

**CRACK PROPAGATION DURING ACTUATION CYCLES
OF THE NITIF HIGH TEMPERATURE SHAPE
MEMORY ALLOYS**

**NİTİHF YÜKSEK SICAKLIK ŞEKİL HAFIZALI
ALAŞIMLARIN AKTÜASYON DÖNGÜLERİ SIRASINDA
ÇATLAK İLERLEMESİ**

MERİÇ EKİCİLER

PROF. DR. BENAT KOÇKAR

Supervisor

Submitted to

Graduate School of Science and Engineering of Hacettepe University

as a Partial Fulfillment to the Requirements

for the Award of the Degree of Doctor of Philosophy

in Mechanical Engineering

2023

To

my father Durali EKİCİLER,

my mother Zehra EKİCİLER,

and

my sister İrem EKİCİLER

ABSTRACT

CRACK PROPAGATION DURING ACTUATION CYCLES OF THE NITIHf HIGH TEMPERATURE SHAPE MEMORY ALLOYS

Meriç EKİCİLER

Doctor of Philosophy, Mechanical Engineering

Supervisor: Prof. Dr. Benat KOÇKAR

January 2023, 121 pages

Shape Memory Alloys (SMAs) are very special materials with their distinctive ability to recover their shape change by phase transformation via mechanical and/or thermal stimulations. When the alloy heated above a certain temperature, shape change recovery under load/stress could be accomplished. By using this shape change mechanism, SMAs could produce work against loads and they could be used as actuators due to this property in several industries.

NiTi alloys are the most widely used SMAs in commercial applications. However, they have limited TTs below 100°C which inhibits their usage as actuators at elevated temperatures. To achieve higher TTs, NiTiHf alloys are the most promising among other SMAs.

There is an increasing demand for using these alloys in actuator type of applications at high operating temperatures. In this demand, NiTiHf High Temperature Shape Memory Alloys (HTSMAs) could be good candidates since they have been known as not only HTSMAs but also SMAs having high strength. Although they have relatively better mechanical and shape memory properties at high temperatures they still suffer from thermal and thermomechanical cyclic instability problem due to the decrease of their strength with the increase of operating temperatures. Thus, knowing their fatigue and crack growth properties could be useful by considering their reliability and robustness in their usage. However, there are limited number of studies in the literature on fatigue, crack initiation and growth behavior that leads to fracture by running actuation thermal cycles on these alloys under constant load. Therefore, it is required to know and understand the actuation fatigue properties together with the crack growth behavior at elevated temperatures. Additionally, creep based viscoplasticity could have an effect on crack formation and propagation, since these materials work at elevated temperatures as mentioned above. Thus, knowing the crack growth behavior under creep formation could be also very beneficial for utilizing these alloys in especially aerospace industry.

Within the scope of the mentioned context, actuation fatigue experiments under load were conducted for different conditions then crack growth behavior and actuation fatigue properties were investigated.

Firstly, dog-bone shaped hot-extruded Ni₅₀Ti₃₀Hf₂₀ (at.%) HTSMA tensile test sample without a pre-notch was thermally cycled under constant load magnitude. Actuation fatigue behavior, surface crack formations and crack growth behavior were investigated at intermittent cycles. The thermal cycles were stopped after running certain amount of cycles, the sample was detached from the test set up and the crack formations and the changes in the crack lengths were determined by using Optical Microscope (OM).

Secondly, hot extruded and pre-notched (HE-PN) Ni₅₀Ti₃₀Hf₂₀ (at.%) test samples were used to investigate the crack growth and actuation fatigue properties during heating-

cooling cycles under load. However, different type of crack growth behavior and shape memory properties were observed from each sample.

Thirdly, to achieve more stable crack growth and actuation fatigue properties, hot-extruded, pre-notched and subsequently annealed (HE-PN-AN) samples were tested via running actuation fatigue tests on $\text{Ni}_{50}\text{Ti}_{30}\text{Hf}_{20}$ (at.%) alloys. Slower crack growth was determined in HE-PN-AN sample than that of in HE-PN sample. In addition, similar crack growth rates and more stable actuation fatigue performance were observed in annealed samples. On the other hand, there were variations in the crack growth rate and the fatigue properties of HE-PN samples. Lastly, minor cracks were formed and propagated together in annealed samples due to relieving the induced stress during hot-extrusion and relatively easier new surface generation with the same amount of energy.

Moreover, actuation fatigue tests were conducted on 3 different samples to see the effect of Upper Cycle Temperature (UCT), applied stress magnitude and Hf content on crack formation, crack growth and actuation fatigue properties. It is important to note that UCT is the limit temperature to which the samples are heated when conducting actuation fatigue tests. HE-PN-AN coded $\text{Ni}_{50}\text{Ti}_{30}\text{Hf}_{20}$ (at.%) samples were tested using different test parameters. While testing one of the HE-PN-AN $\text{Ni}_{50}\text{Ti}_{30}\text{Hf}_{20}$ (at.%) samples UCT value was set to 600°C and the stress was kept constant at 200 MPa stress value. Another HE-PN-AN sample having the same aforementioned composition was tested under 300 MPa stress magnitude by setting the UCT to 440°C . Actuation properties were in similar trends with the previous tests conducted on the other annealed samples with the application of 200 MPa, but increase in the stress magnitude led a shorter actuation fatigue life through which crack propagation could not be followed due to the sudden fracture. To see the effect of Hf content to the actuation fatigue properties of NiTiHf HTSMA, $\text{Ni}_{50}\text{Ti}_{25}\text{Hf}_{25}$ (at.%) was tested under 200 MPa stress and by setting the UCT to 600°C . UCT value was fixed as 600°C to observe the complete austenitic transformation in cycles since this alloy has higher Hf content and hence higher TTs. Actuation strain values of $\text{Ni}_{50}\text{Ti}_{30}\text{Hf}_{20}$ (at.%) were found to be higher than that of $\text{Ni}_{50}\text{Ti}_{25}\text{Hf}_{25}$ (at.%) alloy throughout the actuation cycles which were conducted under 200 MPa and by using 600°C as UCT. Higher UCT resulted higher actuation strains due to the increase in

transforming volume but high amount surface cracks due to severe oxidation were formed around pre-notch area. High amount of oxidation-based crack formation and propagation also increased plastic strain accumulation over the actuation cycles. Although higher actuation strain values could be achieved by higher UCT application, which is one of the important parameters in actuator applications achieving higher actuation strain values did not provide longer fatigue lifetimes, reliable and stable shape memory properties.

Lastly, since these SMAs were heated to higher temperatures during actuation fatigue cycles, creep effect on crack formation at 600°C temperature under different stress levels were investigated. Ni₅₀Ti₃₀Hf₂₀ (at.%) HE-PN-AN samples were loaded to 300 MPa, 400 MPa and 500 MPa at 600°C and the creep experiments were run until failure. It was observed that higher applied stress magnitudes and high UCT led to observe very high creep rates.

Keywords: High Temperature Shape Memory Alloys, Actuation Fatigue, Crack Behavior, Crack Growth, NiTiHf

ÖZET

NiTiHF YÜKSEK SICAKLIK ŞEKİL HAFIZALI ALAŞIMLARIN AKTÜASYON DÖNGÜLERİ SIRASINDA ÇATLAK İLERLEMESİ

Meriç EKİCİLER

Doktora, Makina Mühendisliği Bölümü

Tez Danışmanı: Prof. Dr. Benat KOÇKAR

Ocak 2023, 121 sayfa

Şekil Hafızalı Alaşımlar (ŞHA), mekanik ve/veya termal uyarım yoluyla faz dönüşümünden faydalanarak şekil değişikliklerini geri kazanabilme yeteneklerine sahip özel malzemelerdir. Alaşım belirli bir sıcaklığın üzerine ısıtıldığında yük altında şekil değişikliğinin geri kazanımı sağlanabilmektedir. ŞHA' lar bu şekil değiştirme mekanizmasını kullanarak, yüklere karşı iş üretebilmekte ve bu özelliklerine bağlı olarak çeşitli endüstrilerde aktüatör olarak kullanılabilirler.

NiTi alaşımları, ticari uygulamalarda en yaygın kullanılan ŞHA' lardır. Fakat bununla birlikte, 100°C' nin altında sınırlı dönüşüm sıcaklıklarına sahiptirler ve bu durum yüksek sıcaklıklarda aktüatör olarak kullanımlarını kısıtlamaktadır. Daha yüksek dönüşüm sıcaklıklarında kullanım için NiTiHf alaşımları, diğer ŞHA' lar arasında en umut verici olanlardır.

Bu alaşımların yüksek çalışma sıcaklıklarında aktüatör tipi uygulamalarda kullanılmasına yönelik artan bir talep vardır. NiTiHf alaşımları, sadece yüksek sıcaklık ŞHA' ları olarak değil, aynı zamanda yüksek mukavemete sahip ŞHA' lar olarak da bilindiğinden, bu talepte uygun adaylar olabilirler. Yüksek sıcaklıklarda nispeten daha iyi mekanik ve şekil hafıza özelliklerine sahip olmalarına rağmen, çalışma sıcaklıklarının artmasıyla dayanımlarının azalması nedeniyle hala termal ve termomekanik döngüsel kararsızlık problemleri bulunmaktadır. Bu nedenle, yorulma ve çatlak büyüme özelliklerini bilmek, kullanımlarındaki güvenilirlik ve sağlıklarını göz önünde bulundurarak faydalı olabilir. Bununla birlikte, sabit yük altında aktüasyon çevrimlerindeki yorulma davranışı, çatlakların nasıl davranarak yayıldığı ve ardından kırılmaya neden olduğu konusunda literatürde sınırlı sayıda çalışma bulunmaktadır. Bu nedenle, yüksek sıcaklıklarda çatlak büyüme davranışı ile birlikte aktüasyon yorulma özelliklerinin bilinmesi ve anlaşılması gerekmektedir. Ek olarak, bu malzemeler yüksek sıcaklıklarda çalıştıklarından, sürünme bazlı viskoplastisite, çatlak oluşumu ve ilerlemesi üzerinde bir etkiye sahip olabilir. Bu nedenle, sürünme oluşumu altındaki çatlak büyüme davranışının bilinmesi, bu alaşımların özellikle havacılık endüstrisinde kullanımında yararlı olabilir.

Bahsedilen kapsamda, farklı koşullar için yük altında aktüasyon yorulma deneyleri gerçekleştirilmiş, ardından çatlak büyüme davranışı ve aktüasyon yorulma özellikleri incelenmiştir.

İlk olarak, sıcak ekstrüde edilmiş Ni₅₀Ti₃₀Hf₂₀ (at.%) numunesi, ön çentiksiz, sabit yük büyüklüğü altında termal döngüye tabi tutulmuştur. Aralıklı döngülerde aktüasyon yorulma davranışı, yüzey çatlak formları ve çatlak büyüme davranışı incelenmiştir. Isıl çevrimler belli sayıda çevrim yapıldıktan sonra durdurulmuş, numune test düzeneğinden alınmış ve Optik Mikroskop (OM) kullanılarak çatlak oluşumları ve çatlak uzunluklarındaki değişimler belirlenmiştir.

İkinci olarak, yük altında ısıtma-soğutma çevrimleri sırasında çatlak büyümesini ve aktüasyon yorulma özelliklerini araştırmak için sıcak ekstrüde edilmiş ve önceden çentik açılmış (HE-PN) Ni₅₀Ti₃₀Hf₂₀ (at.%) test numuneleri kullanılmıştır. Bununla birlikte, her

numunede birbirine göre farklı tipte çatlak büyümesi ve şekil hafıza özellikleri gözlenmiştir.

Üçüncü olarak, daha kararlı çatlak büyümesi ve aktüasyon yorulma özellikleri elde etmek için, sıcak ekstrüde edilmiş, önceden çentik açılmış ve ardından tavlanmış (HE-PN-AN) numuneler, $Ni_{50}Ti_{30}Hf_{20}$ (at.%) alaşımları ile aktüasyon yorulma testleri altında test edilmiştir. Aktüasyon yorulma testlerinde HE-PN-AN' de HE-PN' ye göre daha yavaş çatlak büyümesi tespit edilmiştir. Ayrıca, tavlanmış numunelerde benzer çatlak büyüme oranları ve daha kararlı aktüasyon yorulma performansı gözlenmiştir. Buna karşılık, HE-PN numunelerinin çatlak büyüme hızında ve yorulma özelliklerinde farklılıklar görülmüştür. Son olarak, sıcak ekstrüzyon sırasında oluşan gerilmelerin hafifletilmesi ve aynı miktarda enerji ile nispeten daha kolay yeni yüzey oluşumu nedeniyle, tavlanmış numunelerde küçük çatlaklar oluşmuş ve birlikte ilerlemiştir.

Ayrıca, üst çevrim sıcaklığı' nın (ÜÇS), uygulanan gerilim büyüklüğü ve Hf içeriği' nin çatlak oluşumu, çatlak büyümesi ve aktüasyon yorulma özellikleri üzerindeki etkisini görmek için 3 farklı numune üzerinde aktüasyon yorulma testleri yapılmıştır. ÜÇS' nın, aktüasyon yorulma testleri yapılırken numunelerin ısıtıldığı sınır sıcaklık değeri olduğuna dikkat etmek gerekmektedir. HE-PN-AN kodlu $Ni_{50}Ti_{30}Hf_{20}$ (at.%) numuneleri farklı test parametreleri kullanılarak test edilmiştir. HE-PN-AN numunelerinden birisi test edilirken ÜÇS değeri $600^{\circ}C$ olarak ayarlanmış ve gerilim 200 MPa gerilme değerinde sabit tutulmuştur. Yukarıda belirtilen bileşime sahip başka bir HE-PN-AN numunesinin ise, ÜÇS değeri $440^{\circ}C$ ' ye ayarlanmış ve gerilme 300 MPa gerilme değerinde sabit tutulmuştur. Aktüasyon özellikleri, 200 MPa uygulaması ile diğer tavlanmış numuneler üzerinde daha önce yapılan testlerle benzer eğilimlerde görülmüş, ancak gerilme büyüklüğündeki artış, ani kırılma nedeniyle çatlak ilerlemesinin takip edilemediği daha kısa aktüasyon yorulma ömrüne neden olmuştur. Hf içeriğinin NiTiHf alaşımlarının aktüasyon yorulma özelliklerine etkisini görmek için, $Ni_{50}Ti_{25}Hf_{25}$ (at.%) 200 MPa gerilme altında ve ÜÇS $600^{\circ}C$ ' ye ayarlanarak test edilmiştir. Bu alaşım daha yüksek Hf içeriğine ve dolayısıyla daha yüksek dönüşüm sıcaklıklarına sahip olduğundan, döngülerdeki tam östenitik dönüşümü gözlemlemek için ÜÇS değeri $600^{\circ}C$ olarak sabitlenmiştir. 200 MPa altında ve ÜÇS olarak $600^{\circ}C$ 'nin kullanıldığı aktüasyon

döngülerinde, $Ni_{50}Ti_{30}Hf_{20}$ (at.%) aktüasyon gerinim değerlerinin $Ni_{50}Ti_{25}Hf_{25}$ (at.%) alaşımından daha yüksek olduğu görülmüştür. Daha yüksek ÜÇS, dönüşüm hacmindeki artıştan dolayı daha yüksek aktüasyon gerinimlerine neden olmuş, ancak çentik çevresindeki şiddetli oksidasyon nedeniyle yüksek miktarda yüzey çatlakları oluşmuştur. Yüksek miktarda oksidasyona dayalı çatlak oluşumu ve ilerlemesi, aktüasyon döngüleri boyunca plastik gerinim birikimini de artırmıştır. Aktüatör uygulamalarında önemli parametrelerden biri olan yüksek aktüasyon gerinim değerleri, daha yüksek ÜÇS uygulaması ile elde edilebilse de daha uzun yorulma ömürleri, güvenilir ve kararlı şekil hafızası özellikleri sağlanamamıştır.

Son olarak, bu ŞHA' lar aktüasyon yorulma çevrimleri sırasında yüksek sıcaklıklara ısıtıldıklarından, farklı gerilme seviyeleri altında $600^{\circ}C$ sıcaklıkta çatlak oluşumu üzerindeki sürünme etkisi incelenmiştir. $Ni_{50}Ti_{30}Hf_{20}$ (at.%) HE-PN-AN örnekleri $600^{\circ}C$ ' de 300 MPa, 400 MPa ve 500 MPa gerilmelere yüklenmiş ve sürünme deneyleri kırılmaya kadar sürdürülmüştür. Uygulanan yüksek gerilme büyüklüklerinin ve yüksek ÜÇS' nin yüksek sürünme oranlarına yol açtığı gözlemlenmiştir.

Anahtar Kelimeler: Yüksek Sıcaklık Şekil Hafızalı Alaşımlar, Aktüasyon Yorulması, Çatlak Davranışı, Çatlak İlerlemesi, NiTiHf

ACKNOWLEDGEMENTS

Firstly, I would like to express my special thanks and my respect to my supervisor Prof. Dr. Benat KOÇKAR for all the support and guidance with her expertise in addition to strengthening my research endeavors and encouraging my further development during my Ph.D. study.

Also, I would like to thank to Assoc. Prof. Dr. Zarife Gökür BÜKE and Assist. Prof. Dr. Okan GÖRTAN for serving in my thesis review committee, giving me valuable suggestions, comments and contributions throughout my studies. I would like to sincerely thank to jury members Prof. Dr. Rıza GÜRBÜZ and Assoc. Prof. Dr. Bilsay SÜMER for their valuable comments and contributions.

I want to thank to my labmates, my friends Erhan AKIN, Oğulcan AKGÜL and Onat TUĞRUL for their good friendship, valuable technical discussions and great conversations.

I would like to thank to Turkish Aerospace Industries for the materials used in this study procured within the framework of the project numbered DKTM/2015/10.

Lastly, I want to thank to my father Durali EKİCİLER, my mother Zehra EKİCİLER and my sister İrem EKİCİLER for their never-ending support and patience throughout my study.

Meriç EKİCİLER

January 2023, Ankara

TABLE OF CONTENTS

ABSTRACT	i
ACKNOWLEDGEMENTS	ix
TABLE OF CONTENTS	x
LIST OF FIGURES.....	xii
LIST OF TABLES	xviii
SYMBOLS AND ABBREVIATIONS	xix
1. INTRODUCTION.....	1
2. THEORY AND LITERATURE	7
2.1. Martensitic Transformation (MT)	7
2.2. Shape Memory Effect (SME) and Superelasticity (SE).....	10
2.3. Applications of SMAs	15
2.4. NiTi Based Shape Memory Alloys	17
2.5. High Temperature Shape Memory Alloys (HTSMAs).....	19
2.6. Fatigue of HTSMAs	22
2.7. Creep	27
3. EXPERIMENTAL METHODS	30
3.1. As-received material	30
3.2. Sample Preparation	31
3.3. Actuation Fatigue Test set-up and Applied Tests	33
3.4. Optical Microscope Analysis and Fracture Surface SEM Images	39
3.5. Stress Intensity Factor (SIF) calculation	40
4. RESULTS AND DISCUSSIONS	42
4.1. Actuation Fatigue Testing of HE Samples.....	42
4.2. Actuation Fatigue Testing of HE-PN Samples	50
4.3. Actuation Fatigue Testing of HE-PN-AN Samples	60

4.4. Discussions on Actuation Fatigue Testing of HE-PN and HE-PN-AN samples.	71
4.5. Effect of UCT and Stress on Actuation Fatigue Tests of HE-PN-AN Samples..	75
4.6. Actuation Fatigue Testing of Ni ₅₀ Ti ₂₅ Hf ₂₅ (at.%) HE-PN-AN alloy.....	83
4.7. Effect of UCT, Stress and Hf content on Actuation Fatigue and comparison of actuation fatigue results	90
4.8. Creep Experiment Results	96
5. CONCLUSIONS	103
6. REFERENCES	108
APPENDIX.....	115
APPENDIX 1 - Publications.....	115
APPENDIX 2 – Conference Presentations	116
APPENDIX 3 – Originality Report	118
CURRICULUM VITAE.....	120

LIST OF FIGURES

Figure 2.1-1. (a) Schematic representation of shape change through phase transformation, (b) strain accommodation by slip mechanism, (c) strain accommodation by twinning mechanism [39].....	8
Figure 2.1-2. Schematic representation of gibbs free energy curves [39].....	9
Figure 2.2-1. Schematic representation of SME mechanism on Stress - Strain (σ - ϵ) and Temperature – Strain (T – ϵ) diagram with following stages (A - B - C - D – E - F) [2]	12
Figure 2.2-2 Schematic representation of SE mechanism on Stress - Strain (σ - ϵ) diagram with following stages (A - B - C) [14]	13
Figure 2.2-3. Schematic representation of conditions on SME and SE [39]	14
Figure 3.1-1 (a) Hot-extruded Ni ₅₀ Ti ₃₀ Hf ₂₀ (at. %) HTSMA bar, (b) machined bar, (c) Sliced pieces by Wire EDM, (d) Wire EDM machine	30
Figure 3.2-1. Representation of sample and pre-notch dimensions [67]	31
Figure 3.2-2. Vertical cylindrical furnace	32
Figure 3.3-1 (a) Actuation fatigue experiment test set-up, (b) schematic diagram [74]	33
Figure 3.3-2 A schematic curve of an actuation fatigue (heating-cooling) test cycle under constant load and determining the values as TTs, actuation strain, irrecoverable strain and thermal hysteresis [18].....	36
Figure 3.3-3 Additional lifting mechanism integrated to test setup.....	37
Figure 3.3-4. Former type of weight hanger and current type of weight hanger after test set-up improvement.....	38
Figure 3.3-5. Integrated lifting slings in test set-up to catch the dropping lower grip and weight hanger	38
Figure 3.4-1. Nikon Eclipse LV 150 optical microscope.....	40
Figure 4.1-1. Strain-Temperature curves from the actuation fatigue experiment of Ni ₅₀ Ti ₃₀ Hf ₂₀ (at.%) HE sample.....	43
Figure 4.1-2. A schematic curve of a actuation fatigue (heating-cooling) test cycle under constant load and determining the values as TTs, actuation strain, irrecoverable strain and thermal hysteresis [18].....	44

Figure 4.1-3. The evolution of the TTs that was determined from the actuation fatigue experiment of Ni ₅₀ Ti ₃₀ Hf ₂₀ (at.%) HE sample under constant stress.	45
Figure 4.1-4. Actuation strain values that were determined from the actuation fatigue experiment of Ni ₅₀ Ti ₃₀ Hf ₂₀ (at.%) HE Sample 1 under constant stress.....	46
Figure 4.1-5. Accumulated irrecoverable strain values determined from actuation fatigue experiments of Ni ₅₀ Ti ₃₀ Hf ₂₀ (at.%) HE Sample 1 under constant stress.	47
Figure 4.1-6. Thermal Hysteresis values determined from actuation fatigue experiments of Ni ₅₀ Ti ₃₀ Hf ₂₀ (at.%) HE Sample 1.	48
Figure 4.1-7. Optical Images of the crack formations in HE sample that were taken after intermittent cycles.....	49
Figure 4.1-8. Crack length evolution with the number of cycles of HE sample from a leading crack to fracture	50
Figure 4.2-1. Strain-Temperature curves from the actuation fatigue experiments of 3 HE-PN Ni ₅₀ Ti ₃₀ Hf ₂₀ (at.%) samples [67].	51
Figure 4.2-2. TT evolutions determined from actuation fatigue experiment of Ni ₅₀ Ti ₃₀ Hf ₂₀ (at.%) HE-PN sample.	52
Figure 4.2-3. Actuation strain values determined from actuation fatigue experiments of 3 HE-PN Ni ₅₀ Ti ₃₀ Hf ₂₀ (at.%) samples [67].	52
Figure 4.2-4. Accumulated irrecoverable strain values determined from actuation fatigue experiments of 3 HE-PN Ni ₅₀ Ti ₃₀ Hf ₂₀ (at.%) samples under constant stress [67].	54
Figure 4.2-5. Thermal Hysteresis values determined from actuation fatigue experiments of 3 HE-PN Ni ₅₀ Ti ₃₀ Hf ₂₀ (at.%) samples.....	54
Figure 4.2-6. The region showing where the crack images were taken and the crack images of the HE-PN samples before the actuation fatigue test and just before the fracture [67].	56
Figure 4.2-7. Pre-notch, major crack and side crack optical micrographs of HE-PN samples after 1,200 th , 1,400 th , 1,600 th , 1,800 th and 2,000 th cycles of actuation cycling [67].....	57
Figure 4.2-8. Evolution of crack lengths with the number of cycles in actuation fatigue cycling of HE-PN samples [67].....	58
Figure 4.2-9. SIF values calculated for HE-PN samples by the crack lengths at intermittent cycles [67].....	59

Figure 4.2-10. SEM images from fracture surface of Sample 4 after actuation fatigue experiment.....	60
Figure 4.3-1. Strain-Temperature curves from the actuation fatigue experiments of Ni ₅₀ Ti ₃₀ Hf ₂₀ (at.%) HE-PN-AN samples [67].....	62
Figure 4.3-2. Evolution of TTs, which were determined from Actuation Fatigue experiment conducted on HE-PN-AN Ni ₅₀ Ti ₃₀ Hf ₂₀ (at.%) samples.	62
Figure 4.3-3. Actuation strain values determined from Actuation Fatigue experiment conducted on HE-PN-AN Ni ₅₀ Ti ₃₀ Hf ₂₀ (at.%) samples [67].	63
Figure 4.3-4. Accumulated irrecoverable strain values determined from Actuation Fatigue experiment conducted on HE-PN-AN Ni ₅₀ Ti ₃₀ Hf ₂₀ (at.%) samples [67].	64
Figure 4.3-5. Thermal hysteresis values determined from actuation fatigue experiments of Ni ₅₀ Ti ₃₀ Hf ₂₀ (at.%) HE-PN-AN sample.....	65
Figure 4.3-6. The region showing where the crack images were taken and the crack images of the HE-PN-AN samples before the actuation fatigue test and just before the fracture [67].	66
Figure 4.3-7. Pre-notch, major crack and side crack optical micrographs of HE-PN-AN samples after 1,200 th , 1,400 th , 1,600 th , 1,800 th and 2,000 th cycles of actuation cycling [67]	67
Figure 4.3-8. Evolution of crack lengths with the number of cycles in actuation fatigue cycling of HE-PN-AN samples [67]	68
Figure 4.3-9. Pre-notch, major crack and side crack optical micrographs of Sample 5 after 1,800 th , 2,000 th cycles of actuation cycling [67]	69
Figure 4.3-10. SIF values calculated for HE-PN-AN samples by the crack lengths at intermittent cycles [67].....	70
Figure 4.3-11. SEM image from fracture surface of Sample 6 after actuation fatigue experiment.....	70
Figure 4.4-1. Evolution of crack lengths with the number of cycles in actuation fatigue cycling of HE-PN and HE-PN-AN samples [67].....	71
Figure 4.4-2. Pre-notch, major crack and side crack optical micrographs of HE-PN and HE-PN-AN samples after 1,200 th , 1,400 th , 1,600 th , 1,800 th and 2,000 th cycles of actuation cycling [67].....	73
Figure 4.4-3. Actuation strain values determined from Actuation Fatigue experiment conducted on HE-PN and HE-PN-AN Ni ₅₀ Ti ₃₀ Hf ₂₀ (at.%) samples [67].....	74

Figure 4.4-4. SIF values calculated for HE-PN and HE-PN-AN samples by the crack lengths at intermittent cycles [67].....	75
Figure 4.5-1. Strain vs Temperature Curves of HE-PN-AN samples tested under constant load refers to 300 MPa Stress at different UCTs	76
Figure 4.5-2. Strain-Temperature curves from the actuation fatigue experiment of Ni ₅₀ Ti ₃₀ Hf ₂₀ (at. %) HE-PN-AN sample (a) under 200 MPa with 600°C UCT, (b) under 300 MPa with 440°C UCT.	77
Figure 4.5-3. TT evolution determined from Actuation Fatigue experiment conducted on HE-PN-AN Ni ₅₀ Ti ₃₀ Hf ₂₀ (at. %) sample under 200 MPa with 600°C UCT for Sample 7 and actuation fatigue test under 300 MPa with 440°C UCT for Sample 8.....	78
Figure 4.5-4. Actuation strain values determined from Actuation Fatigue experiment on HE-PN-AN Ni ₅₀ Ti ₃₀ Hf ₂₀ (at. %) sample under 200 MPa with 600°C UCT for Sample 7 and actuation fatigue test under 300 MPa with 440°C UCT for Sample 8.....	79
Figure 4.5-5. Accumulated irrecoverable strain values determined from Actuation Fatigue experiment conducted on HE-PN-AN Ni ₅₀ Ti ₃₀ Hf ₂₀ (at.%) samples under 200 MPa with 600°C UCT for Sample 7 and actuation fatigue test under 300 MPa with 440°C UCT for Sample 8.....	80
Figure 4.5-6. Thermal hysteresis values determined from actuation fatigue experiments of Ni ₅₀ Ti ₃₀ Hf ₂₀ (at.%) HE-PN-AN samples under 200 MPa with 600°C UCT for Sample 7 and actuation fatigue test under 300 MPa with 440°C UCT for Sample 8.	80
Figure 4.5-7. Optical micrographs taken after intermittent actuation cycles for Sample 7	81
Figure 4.5-8. Optical micrographs taken after intermittent actuation cycles for Sample 8	82
Figure 4.5-9. SEM Images from fracture surface of Sample 7 and Sample 8 after actuation fatigue experiments.....	82
Figure 4.6-1. Strain-Temperature curves from the actuation fatigue experiment of Ni ₅₀ Ti ₂₅ Hf ₂₅ (at.%) HE-PN-AN sample under 200 MPa with 600°C UCT.....	84
Figure 4.6-2. Evolution of TTs, which were determined from Actuation Fatigue experiment conducted on HE-PN-AN Ni ₅₀ Ti ₂₅ Hf ₂₅ (at.%) sample under 200 MPa with 600°C UCT	84

Figure 4.6-3. Actuation strain values determined from Actuation Fatigue experiment on HE-PN-AN Ni ₅₀ Ti ₂₅ Hf ₂₅ (at.%) sample under 200 MPa with 600°C UCT	85
Figure 4.6-4. Accumulated irrecoverable strain values determined from Actuation Fatigue experiment conducted on HE-PN-AN Ni ₅₀ Ti ₂₅ Hf ₂₅ (at.%) samples under 200 MPa with 600°C UCT for Sample 9	86
Figure 4.6-5. Thermal hysteresis values determined from actuation fatigue experiments of Ni ₅₀ Ti ₂₅ Hf ₂₅ (at.%) HE-PN-AN samples under 200 MPa with 600°C UCT for Sample 9	87
Figure 4.6-6. Optical micrographs taken after intermittent actuation cycles for Sample 9	88
Figure 4.6-7. Evolution of crack lengths with the number of cycles in actuation fatigue cycling of Ni ₅₀ Ti ₂₅ Hf ₂₅ (at.%) HE-PN-AN Sample 9	89
Figure 4.6-8. SEM Images from fracture surface of Sample 9 after actuation fatigue experiment	90
Figure 4.7-1. Evolution of TTs, which were determined from Actuation Fatigue experiment conducted on Sample 4, Sample 6, Sample 7, Sample 8 and Sample 9	91
Figure 4.7-2. Actuation strain values determined from Actuation Fatigue experiment on Sample 4, Sample 6, Sample 7, Sample 8 and Sample 9	92
Figure 4.7-3. Accumulated irrecoverable strain values determined from Actuation Fatigue experiment conducted on Sample 4, Sample 6, Sample 7, Sample 8 and Sample 9	93
Figure 4.7-4. Thermal hysteresis values determined from actuation fatigue experiments of Sample 4, Sample 6, Sample 7, Sample 8, Sample 9	94
Figure 4.7-5. Optical micrographs taken after 200 th intermittent actuation cycles for Sample 7 and Sample 9	95
Figure 4.7-6. SEM Images from fracture surface of Sample 7, Sample 8 and Sample 9 after actuation fatigue experiment	95
Figure 4.8-1. Creep Experiment results showing True Strain vs Time Curves, which were conducted at 600 °C under 300, 400 and 500 MPa initial loading	96
Figure 4.8-2. Optical micrographs taken after different intermittent creep experiment times for Sample 10 tested under 300 MPa	98

Figure 4.8-3. Optical micrographs taken after different intermittent creep experiment times for Sample 11 tested under 400 MPa	99
Figure 4.8-4. Optical micrographs taken after different intermittent creep experiment times for Sample 12 tested under 500 MPa	100
Figure 4.8-5. SEM Images from fracture surface of Sample 10 and Sample 12 which had creep experiment at 600°C under 300 MPa and 500 MPa.....	101
Figure 4.8-6. SEM Image from fracture surface of Sample 11 which had creep experiment at 600°C under 400 MPa.....	101

LIST OF TABLES

Table 3.3-1. Actuation Fatigue Test Sample Types and Testing Parameters	35
Table 4.1-1 Stress-free TTs of Ni ₅₀ Ti ₃₀ Hf ₂₀ (at.%) alloys [22].....	42
Table 4.2-1. Crack growth rate values (“m”) of HE-PN samples and crack length change trend [67].....	59
Table 4.3-1. Stress-free TTs of annealed Ni ₅₀ Ti ₃₀ Hf ₂₀ (at.%) alloys [22]	61
Table 4.3-2. Crack growth rate values (“m”) of HE-PN-AN samples and crack length change trend [67].....	69
Table 4.4-1. Crack growth rate values (“m”) of HE-PN and HE-PN-AN samples and crack length change trend [67].....	72
Table 4.6-1. Stress-free TTs of annealed Ni ₅₀ Ti ₂₅ Hf ₂₅ (at.%) alloys	83
Table 4.8-1. Creep Strain Rates for Ni ₅₀ Ti ₃₀ Hf ₂₀ (at.%) HE-PN-AN samples at 600°C	97

SYMBOLS AND ABBREVIATIONS

Symbols

Au	Gold
Cu	Copper
Fe	Iron
Hf	Hafnium
Ni	Nickel
Pd	Palladium
Pt	Platinum
R^2	Coefficient of Determination (R-Squared)
Ti	Titanium
T_{melting}	Melting Temperature
Zr	Zirconium

Abbreviations

A_f	Austenite Finish Temperature
A_s	Austenite Start Temperature
DSC	Differential Scanning Calorimeter
EDM	Electrical Discharge Machining
HTSMA	High Temperature Shape Memory Alloy
LCT	Lower Cycle Temperature
M_f	Martensite Finish Temperature

M_s	Martensite Start Temperature
MT	Martensitic Transformation
SE	Superelasticity
SEM	Scanning Electron Microscope
SENT	Single Edge Notch Test
SIF	Stress Intensity Factor
SIM	Stress Induced Martensite
SMA	Shape Memory Alloy
SME	Shape Memory Effect
TT	Transformation Temperature
UCT	Upper Cycle Temperature

1. INTRODUCTION

SMA's are very special materials which have the ability to recover their shape change by phase transformation through mechanical and/or thermal stimulations. When the alloy is heated above a certain temperature, shape recovery under load/stress could be accomplished. By using this shape change mechanism, SMA's could produce work against loads. In addition, the work per volume of SMA's against the biasing load with large recovery of strain magnitudes can be noticeably higher than that of conventional actuators [1,2]. Additionally, the task performed by the actuator system can be accomplished using fewer parts made of SMA's with more compact and simplified design instead of using several components. This is important for the usage of these alloys in several industries since using less components could decrease the maintenance costs of machine components and reduce the weight of the actuation components by replacing the heavy pneumatic and hydraulic systems in aerospace industry [3,4].

They are used in several industries as actuators, impact absorption components, and constraining components due to the aforementioned properties. There are several applications in automotive and transportation, civil, biomedical and aerospace industries [5–10]. There has been already an implemented SMA actuator in the transmission system of Mercedes A class car and SMA spring in Shinkansen bullet train's gearbox which actuates a thermostatic mixing valve depending on the measured temperature [2,11]. Usage of these alloys with their superelastic properties in biomedical industry is more popular and conventional. Cardiovascular stents and filters, minimally invasive surgery devices and orthodontic braces are sample applications in this industry [2]. In civil industry, there are applications to control the seismic response of a building, bridge or offshore platform. They could also be used as brace and/or washer spring type SMA components during earthquakes by their energy dissipation capability with superelastic properties of SMA's [7,8,12].

However, in aerospace industry, they are mostly used as actuation components. Due to tough regulations worldwide on engine noise levels of the aircraft during landing and takeoff. Chevron type components are used on engines to mix the exhaust gas flow and

reduce the engine noise. There are SMA beams inside these chevrons which increases the mixing thereby reducing the noise at low-speed or low-altitude flight. NiTi alloys have been used in Boeing 777 as variable chevron geometry to control noise reduction [2,10]. Additionally, to replace heavy weight pneumatics or DC motors, torque tube or beam plate forms of SMAs are usually used as actuation components in aerospace industry [4,10].

In applications of many industries, NiTi SMAs are most prevalently used and studied SMAs due to their superior behaviors such as biological compatibility, workability, and resistance to corrosion [2,13,14]. However, they have TTs lower than 100°C.

Due to the commercial applications of these alloys up to now, SMA developments are generally focused on applications with operating temperatures below 100°C. On the other hand, there is a trend using them in envisioned applications of energy and aerospace industries with SMAs operating at high temperatures with stable material properties. Thus, developing robust SMAs which could operate at higher temperatures without losing the strength and actuation capability has become a necessity. These SMAs are classified as High Temperature Shape Memory Alloys (HTSMAs) and TTs are increased by alloying with ternary elements. Au, Pd, Pt, Zr, Hf are used as suitable ternary additional alloying elements in NiTi binary systems. However, Au, Pd, Pt are relatively more expensive than that of others and therefore commercial applications are often not possible. Cost concerns led the researchers to work on alloys with Hf and Zr [14]. But, Hf addition increases TTs more effectively and Zr makes the alloy very brittle, thus NiTiHf alloys are the most suitable one among them [4,13,15].

There have been numerous studies in the literature investigating Ni-rich NiTiHf alloys since they gained attention due to better mechanical and thermal stability with the formations of nano-sized precipitates. These precipitation formations are called as H-phase precipitates [16,17] and could be obtained by aging heat treatment of Ni-rich HTSMAs (include higher (at.%) Ni content than 50%). Aging process results an increase of TTs due to reduction in the Ni content of the matrix [14]. More Hf addition also

increases TTs. In addition to Ni-rich NiTiHf alloys, equiatomic NiTiHf alloys with 20 (at.%) or higher Hf content exhibit TTs higher than 200°C. Accordingly, they have higher TTs than that of age-treated Ni-rich HTSMAs. Higher TTs could also make them potential candidate for high temperature applications [18–22].

Structural fatigue occurs by cycling loading leading to dislocation accumulation in typical structural materials. Accumulated dislocations cause crack formation. Then, formed crack propagates and fatigue failure occurs with fracture. However, fatigue behavior in SMAs is examined via following a different procedure. Because, they work with repetitive phase transformation due to heating-cooling cycling under constant load instead of a cyclic loading as is applied in investigating the fatigue behavior of typical structural materials [23]. Deterioration of the functional properties of SMAs with heating-cooling cycles under load is defined as functional fatigue. Functional fatigue can be investigated considering the activation mechanism of the phase transformation [23]. Pseudoelastic fatigue occurs due to stress induced martensite transformation by applying cyclic mechanical loading at constant temperature. When the load is applied austenitic SMA transforms to martensite and martensitic SMA transforms back to austenite via unloading. Fatigue occurs as a result of the continuation of the phase transformation with the loading-unloading cycle. The other type of fatigue in SMAs is named as actuation fatigue which takes place by thermally induced phase transformation due to running heating-cooling cycle under constant load [23]. Studies in the literature mainly focused on the pseudoelastic fatigue of NiTi instead of investigating the actuation fatigue [24–28].

Experimental investigations on the actuation fatigue of HTSMAs are few in the literature. There are some studies investigating the effect of testing parameters on actuation fatigue as applied load level [29], UCT effect [18] and cooling rate effect [21]. In addition, some researchers have works on the effect of heat treatment to the actuation fatigue behavior [22], microstructural damage evolution during actuation fatigue [23] and effect of corrosive environment on the actuation fatigue properties of the alloys [30]. In spite, there are limited numbers of studies in the literature investigating the crack growth behavior during the actuation fatigue of NiTiHf alloys. Since SMAs are employed as actuators to operate under cyclic loads, determining fatigue crack growth behavior is crucial. But,

determining fatigue crack growth behavior during actuation application is challenging since the approaches of fatigue crack growth, is based on developed models and theories for structural metals that do not show phase transformation [31].

Total-life (safe-life) design approach (TLA) and damage-tolerant design approach (DTA) are used to investigate the fatigue of the materials. In DTA, there is an already initiated crack in the structure, where its resistance to crack growth with cyclic loading is being considered. However, TLA considers a flawless part without a crack assumption. Since small-sized SMAs are used more in the commercial market such as NiTi implants, there are more works in the literature with TLA. Failure occurs at a short time after the nucleation of the crack in small sized components. Therefore, it is more significant to prevent crack nucleation than to control the crack growth in biomedical applications [32].

Compared to TLA, DTA considers the presence of an initial crack. It is more convenient to use DTA when the part is large enough to keep the functionality and to consider the stable crack growth in the presence of defects during the service period of the part/component. Thus, applying this approach to SMA actuators is more suitable when investigating the crack growth since they usually work against constant loads as functional materials. On the other hand, application of DTA approach to SMAs is different and more difficult than that of conventional metals. Because, reversible phase transformation, thermomechanical coupling and martensite reorientation are primary factors to take into account in crack growth investigations of SMAs [32,33]. Additionally, since HTSMA actuators go under phase transformation by heating-cooling at high temperatures with actuation cycling, creep formation could also have an effect on crack growth behavior. There are only few works such as LExcellent et al. investigating creep of NiTi alloy under tensile load [34] and Tugrul et al. [35] investigating the creep behavior of Ni₅₀Ti₂₅Hf₂₅ (at.%) under constant load. However, there has been no work regarding the creep effect on crack formation in SMAs up to author's best knowledge.

There are limited numbers of experimental studies on the crack growth behavior during actuation fatigue of SMAs. Ramaiah et al. [36] performed actuation fatigue experiments

with NiTi wires under load. They showed that surface cracks initiated during thermal cycling did not merely lead to fracture and crack generation at the core was important in realizing the fracture due to temperature gradient based strain inhomogeneity. Additionally, Iliopoulos et al. conducted experiments by applying actuation cycling under load to double notched Ni₆₀Ti₄₀ (at.%) specimens and showed that unstable crack propagation during cooling caused fracture [37]. Jape et al. [38] had experiments on actuation cycling of pre-notched Ni_{49.5}Ti_{50.5} (at.%) compact-tension specimens (CT) and exhibited that the propagation of crack actually occurred during cooling.

However, there aren't many studies looking into crack growth behavior of equiatomic NiTiHf HTSMAs that contains 50 at.% Ni and 50 at.% (Ti+Hf) during actuation fatigue/thermal cycling under constant load.

The present thesis was conducted with the motivation of looking into the issues regarding determination of crack growth and actuation fatigue behavior during the actuation fatigue cycling under loads in equiatomic NiTiHf HTSMAs. Knowing the crack growth behavior could provide a significant guidance on the use of these alloys as actuators. Since there are not many works regarding the crack growth behavior during actuation fatigue cycling under load in NiTiHf alloys, it is expected from this study to particularly contribute to the literature. Also, experiments revealing the effect of UCT, applied stress magnitude and Hf content on the crack propagation and the actuation fatigue behavior of NiTiHf alloys could also expand the scope of the literature.

Within this context, actuation fatigue experiment was conducted and actuation fatigue behavior of hot-extruded (HE) Ni₅₀Ti₃₀Hf₂₀ (at.%) alloy without a pre-notch was revealed. Also, surface crack initiations and crack propagation of these cracks were investigated.

Furthermore, since these materials work under load as actuators, it is important to understand the actuation fatigue behavior and the crack growth behavior during actuation

cycles. Therefore, hot-extruded equiatomic $\text{Ni}_{50}\text{Ti}_{30}\text{Hf}_{20}$ (at.%) samples with pre-notches (HE-PN) were tested by running actuation fatigue cycles under constant load to investigate the crack growth behavior together with the shape memory properties. Then, to have better crack growth response and stable actuation fatigue behavior, subsequent annealing process was applied to new samples and the effect of annealing heat treatment on the actuation fatigue and the crack growth behavior of equiatomic $\text{Ni}_{50}\text{Ti}_{30}\text{Hf}_{20}$ (at.%) (HE-PN-AN) was investigated during actuation cycling.

Moreover, effect of actuation fatigue test parameters such as UCT and applied stress, and effect of higher Hf content on crack growth and actuation fatigue behavior during actuation fatigue cycling were investigated on (HE-PN-AN) NiTiHf HTSMAs. Additionally, effect of creep on crack formation on $\text{Ni}_{50}\text{Ti}_{30}\text{Hf}_{20}$ was investigated since these alloys also work at very high temperatures. Lastly, fracture surfaces after failure of each type of sample were also inspected with SEM images to observe fracture modes.

The data obtained from all the aforementioned experimental studies were evaluated and presented in the relevant parts of this thesis.

2. THEORY AND LITERATURE

In this chapter, general theoretical background for shape memory alloys were provided including martensitic transformation as well as two different effects observed in SMAs, which are superelasticity and shape memory effect. The most intriguing SMAs were classified and the brief information about them were summarized. Then, HTSMAs were introduced and fatigue properties, actuation fatigue investigations and creep investigations of these SMAs were finally reviewed.

2.1. Martensitic Transformation (MT)

Martensitic transformation (MT) is a diffusionless solid to solid phase transformation that takes place by a coordinated shear motion of atoms via cooling the parent phase (austenite) to martensite phase. This shear motion happens in a short distance like a military type movement in contrast to long distance diffusion of atoms [14].

Due to the crystal structure difference between two phases, a macroscopic shape change can occur with the transformation from the high temperature parent phase to the low temperature martensite phase. Martensite phase has a lower symmetry than that of the parent phase so many lattice variants can be formed from the same parent phase. Thus, large strain being created around the martensite phase within the austenite phase could lead to a shape change through MT. This large strain could be accommodated by two mechanisms that are called as slip and twinning. Twinning is usually the strain relieve mechanism of SMAs by generating twinned martensitic structure. While slip causes an irreversible shape change through dislocation formation, twinning causes reversible shape change by strain accommodation through generated twinned martensitic structures. Strain accommodation or in other terms, the accommodation of shape change through MT by slip and twinning formation is shown in Figure 2.1-1.

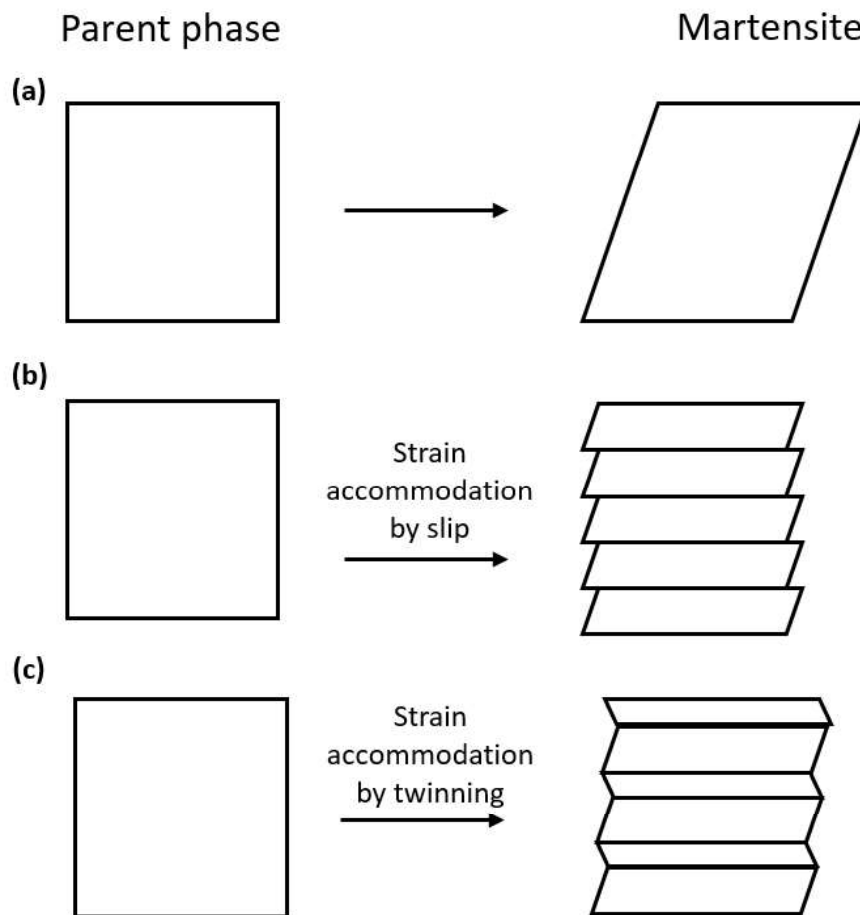


Figure 2.1-1. (a) Schematic representation of shape change through phase transformation, (b) strain accommodation by slip mechanism, (c) strain accommodation by twinning mechanism [39]

The phase transformation from austenite to martensite is called as forward transformation and martensite to austenite transformation is named as reverse transformation. These stated transformations occur within a temperature range not at a single exact temperature. When the material is in austenite phase and started to be cooled, the temperature at which martensitic transformation starts is martensite start (M_s) temperature and at which the forward transformation completes is called as martensite finish temperature (M_f). The temperature at which the reverse transformation starts is called as austenite start (A_s) temperature and the temperature at which the reverse transformation finishes such that martensite completely transforms to austenite phase is called as austenite finish temperature (A_f).

MTs are related with the crystal structure change (from cubic parent phase having higher symmetry to a low temperature martensite phase having lower symmetry) but not the composition change, thus it is important to present the thermodynamics of the transformation with a schematic representation shown in Figure 2.1-2. Free energy evolution of the phases with the temperature change is presented in this figure.

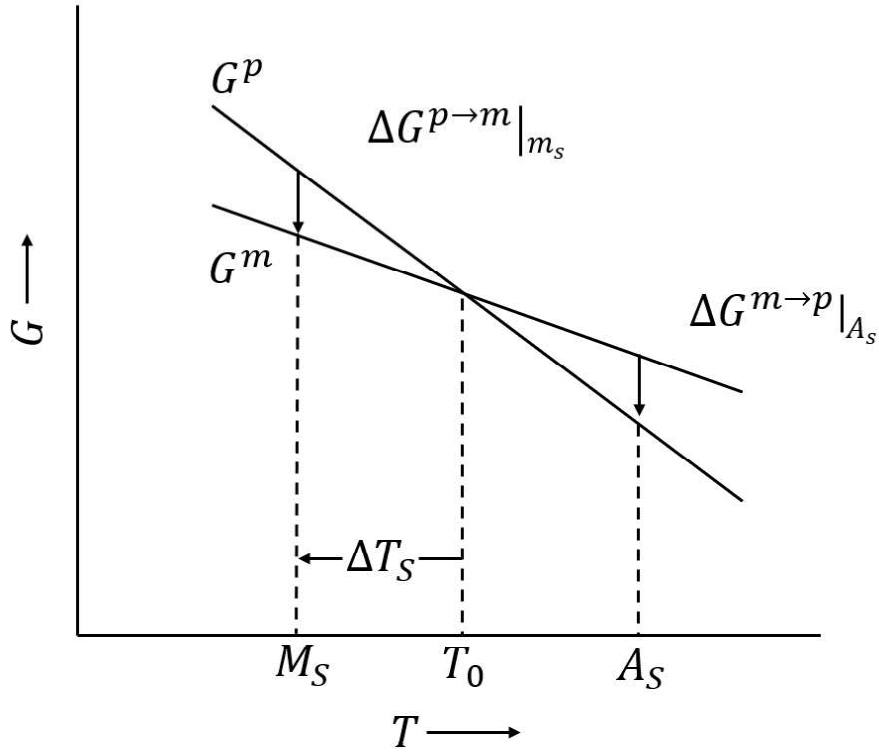


Figure 2.1-2. Schematic representation of gibbs free energy curves [39]

While T_0 is thermodynamic equilibrium temperature at which the phase transformation occurs, G_m and G_p are the gibbs free energy of martensite and gibbs free energy of parent phase austenite. Gibbs free energy difference between austenite and martensite determines the driving force for the martensite nucleation. The total gibbs free energy change during the MT can be defined with the following Equation 1 [39]:

$$\Delta G = \Delta G_c + \Delta G_s + \Delta G_e = \Delta G_c + \Delta G_{nc} \quad (\text{Equation 1})$$

ΔG_c , ΔG_s and ΔG_e are defined as chemical free energy difference between two phases, frictional energy term associated with the transforming interface between parent and

martensite phase, and elastic energy term that is stored around the martensite, respectively. ΔG_{nc} is the non-chemical free energy, which is the summation of friction energy and elastic energy. Thus, supercooling of ΔT_s is needed to overcome the resistance to martensite nucleation since the non-chemical free energy term is not zero and superheating is required for the reverse transformation as well. In addition, due to elastic energy around the martensite causes resistance against martensite growth, further undercooling is needed to overcome this resistance. Thus, M_s and M_f are different temperature values [39].

MTs can be categorized into two main groups as thermoelastic and non-thermoelastic martensitic transformations. Thermoelastic transformation type has smaller temperature hysteresis value since the interface between parent and martensite phase is highly mobile during cooling and heating. Thus, transformation is crystallographically reversible with smaller driving force for transformation where martensite returns to parent phase in the original orientation. However, in non-thermoelastic transformation, the interface between parent and martensite phase is immobile until martensite reaches some critical size, thus driving force for transformation is higher and reverse transformation happens by renucleation of parent phase. Martensitic transformations in SMAs are thermoelastic transformations [39].

2.2. Shape Memory Effect (SME) and Superelasticity (SE)

SMAs show thermoelastic martensitic transformations and the shape changes during transformation are accommodated by twinning mechanism. To accommodate the shape change under no stress, martensite lattice correspondence variants are generated. These twin related martensite correspondence variants accommodate the important part of the strain due to change of lattice structure. Then, these twin related martensite variants come together as several martensite habit planes. They decrease the remaining strain by arranging themselves. Thus, there is nearly no shape change during martensitic transformation and this is called as self-accommodated martensite. Additionally, when there is an external stress applied, most favorable correspondence variant grows depending on the applied stress magnitude and the direction at the expense of other variants to accommodate the strain. This is defined as martensite reorientation and/or

detwinning. Twinned martensite is detwinned with the application of stress and the macroscopic shape change can be observed or measured via the formation of most favorable martensite variant [14].

There are two special mechanisms of SMAs to induce MT via following different paths such as Shape memory effect (SME) and Superelasticity (SE).

The path to follow on the Stress-Strain to obtain SME is shown in Figure 2.2-1. Material in austenite phase under no stress (Point A) is cooled below martensite transformation temperatures (M_s, M_f) and twinned martensite occurs which does not produce a macroscopic shape change (Point B). Then, external stress is applied to twinned martensite and detwinning starts when the applied stress is larger than the stress necessary to reorient the martensite (σ_s). Detwinning via reorientation of martensite continues and the detwinned martensite starts to elastically deform starting with the stress value of σ_f . Detwinning process ends at the transformation finish stress level (σ_f). Self-accommodated martensite variants change into detwinned martensite which yields macroscopic strain. Material keeps staying in detwinned martensite state when it is unloaded elastically to Point D. Finally, material is heated back to A_s temperature to transform to austenite phase (Point E) and shape change by detwinning has been recovered when the temperature is reached to A_f temperature value and the transformation is considered as completed (Point F).

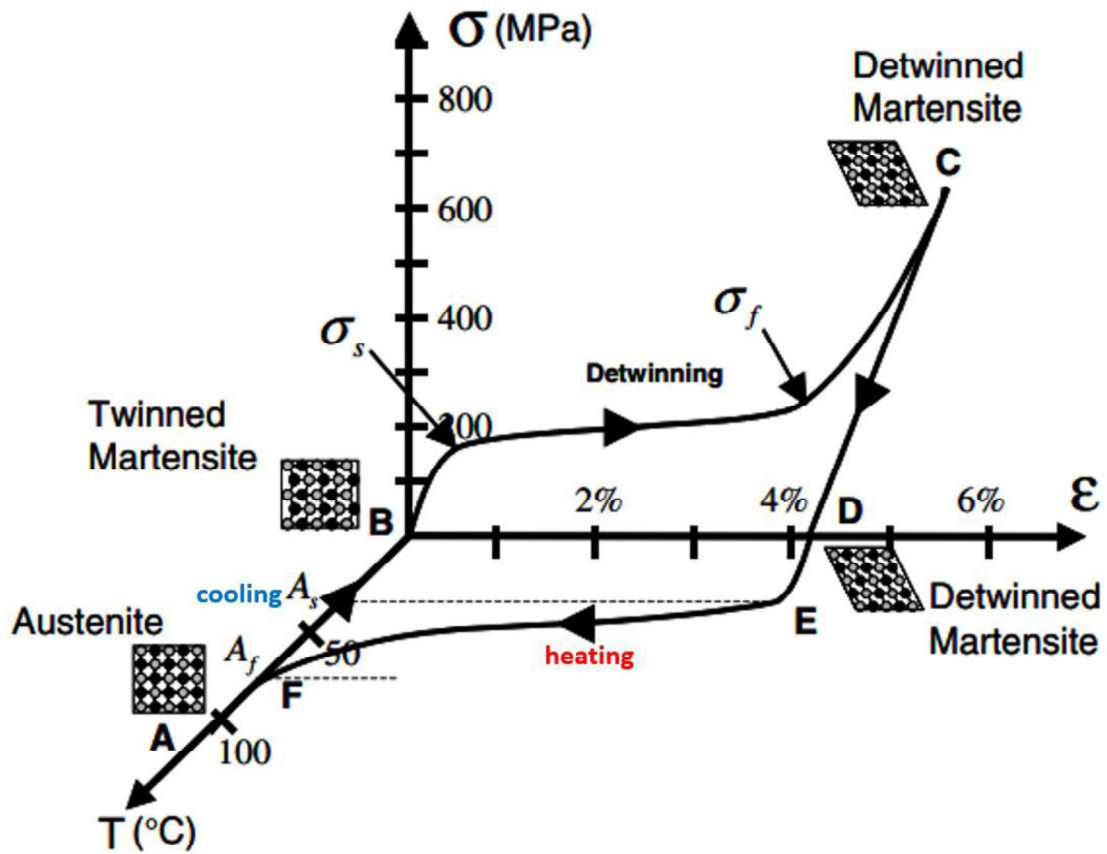


Figure 2.2-1. Schematic representation of SME mechanism on Stress - Strain (σ - ϵ) and Temperature - Strain (T - ϵ) diagram with following stages (A - B - C - D - E - F) [2]

However, in SE, which is also defined as pseudo-elasticity, transformation occurs by external stress application to the material while it is kept in austenite phase at a constant temperature as represented in Figure 2.2-2.

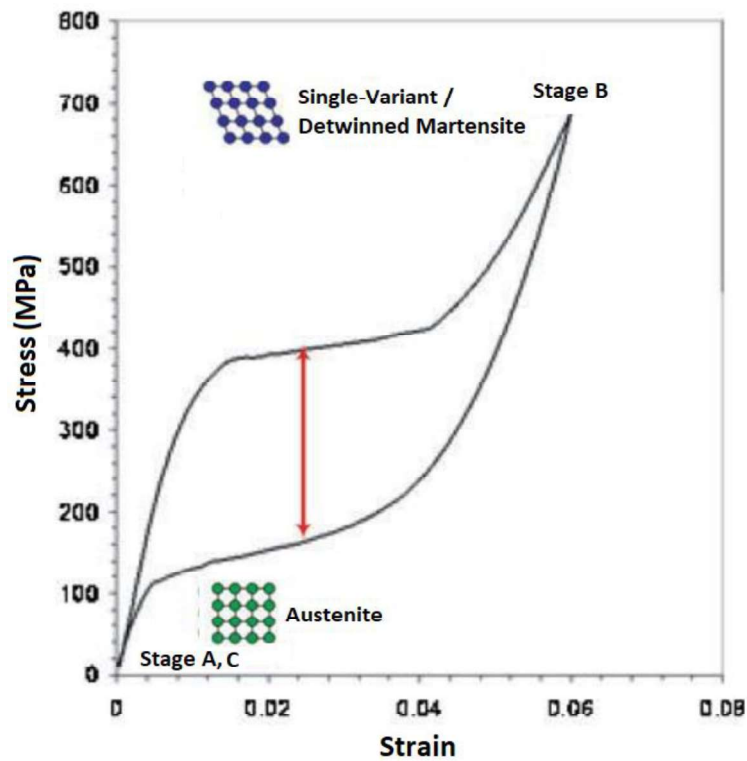


Figure 2.2-2 Schematic representation of SE mechanism on Stress - Strain (σ - ϵ) diagram with following stages (A - B - C) [14]

By the application of external load at Point A, material that is in austenite starts to elastically deform and then the austenite transforms to martensite with the increase in stress. Detwinning takes place throughout the stress plateau and then detwinned martensite may elastically deform up to Point B with the increase in the applied stress. The martensite that is transformed from austenite at a constant temperature with the application of stress is called as Stress Induced Martensite (SIM). After removal of stress, material goes back to austenite phase and recovers the macroscopic strain generated by loading. The alloy should be kept in austenite phase when the loading is started. This can be possible by either heating the alloy directly to A_f temperature or the alloy can be heated to A_f temperature and cooled back to temperature that should be higher than M_s temperature to make sure the alloy does not transform back to martensite. There is also another temperature as M_d , above which it is impossible to obtain stress induced martensitic transformation, since slip formation occurs instead of twinning above that temperature. Both SME and SE could be seen in the same material regarding the stress and temperature range as shown in Figure 2.2-3. While the critical stress for slip line has a negative slope critical stress to induce martensite line has a positive slope. It has been

already known that the critical stress for slip decreases with the temperature increase. It should be drawn from this graphic that, the stress necessary to induce martensite increases as the temperature increases and there is a limitation for this temperature. When the temperature is high enough it is not possible to induce stress instead the alloy starts to plastically deform since the critical stress for slip becomes very low. The striped region in the graphic defines the Superelasticity. If the stress is applied while the alloys is kept above A_f , SIM takes place at a stress above the critical stress for inducing martensite. SIM transforms back to austenite since martensite is unstable above A_f without the application of stress. There is a common area between A_s and A_f where shape memory and superelastic behavior can appear together. When the stress is applied at a temperature that is lower than A_s , martensite is kept as in deformed condition after unloading and the shape change can be recovered via heating the alloy above A_f . In the region between A_s and A_f , the alloy may contain austenite and martensite at the same time, so both superelasticity and shape memory effect can be observed depending on state of stress and temperature.

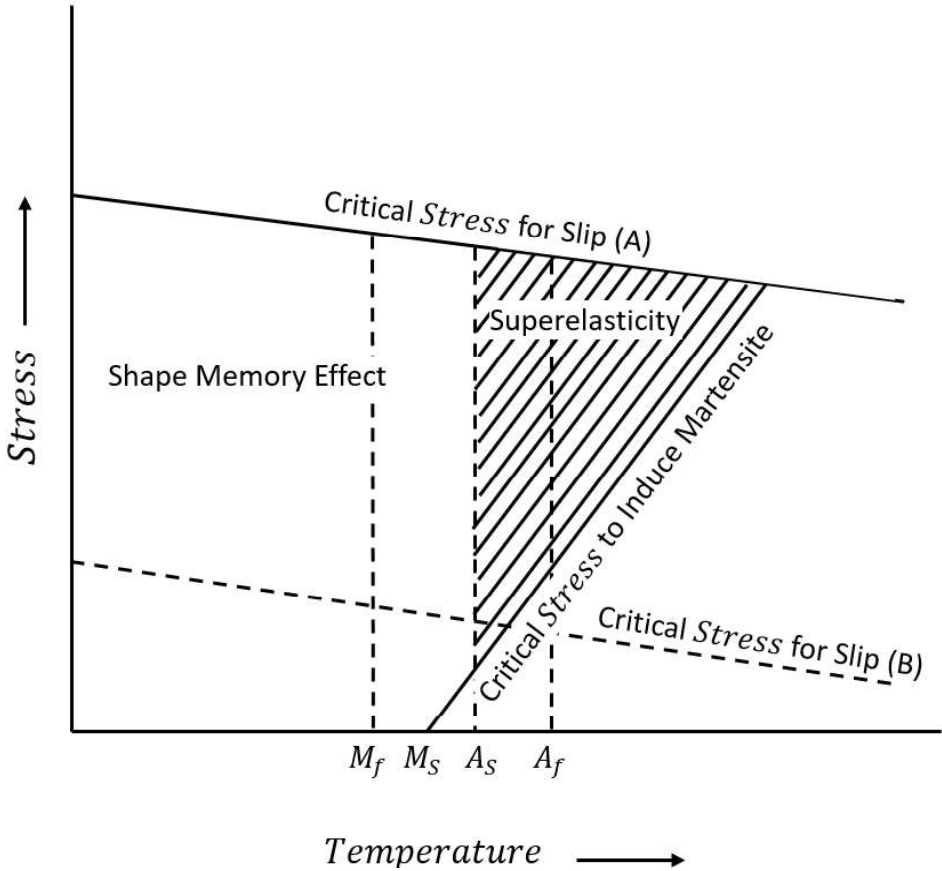


Figure 2.2-3. Schematic representation of conditions on SME and SE [39]

In One-Way Shape Memory Effect (OWSME), SMA is deformed in martensite and then heated to austenite to recover the shape change due to the deformation and cooled back to martensite. The shape is retained after cooling to martensite. To observe OWSME, the deforming, heating (to recover the shape change) and cooling to martensite is repeated. There is also another type effect of SME in which the material remembers the shape of both the parent and the martensite phases under some conditions. This effect is called as Two-Way Shape Memory Effect (TWSME) and microstructural conditioning by creating internal stress field is necessary to see this effect. Internal stress fields could be created by applying plastic deformation [40,41], constrained aging [42], thermal cycling [42,43], and martensite aging [44]. The stress fields, which are induced due to dislocations and precipitates, lead to the formation of certain martensite variants, therefore the alloy starts to form these variants to remember the shape after cooling that is obtained with the deformation of martensite. As a summary, the alloy remembers not only the shape at high temperature but also the shape at low temperature.

2.3. Applications of SMAs

SMAs are used in many industries due to its special properties. They can recover their shape change by phase transformation between martensite phase and austenite phase which can be triggered by mechanical loading and/or heating/cooling. Shape change under applied load can be recovered by heating over a certain temperature. They can achieve high amount of work per volume against the biased load due to large recovery strain magnitudes occurred under higher loads [1,2]. Additionally, they could perform the same function in the actuation system with more compact simplified design and fewer parts instead of using several components. Using fewer components leads to reduce maintenance costs of the system in addition to the reduction of the system weight [3,4].

They are used in several industries as impact absorption components, constraining components and actuators. There are many applications in automotive and transportation, biomedical, civil and aerospace industries [5–10].

There is an example for the application of SMAs in Mercedes A class car as a sensor with their actuation function in transmission system. SMA spring detects the temperature and actuates a valve to change the oil flow direction when temperature comes to a specific value. Additionally, there is a similar type of application Shinkansen bullet train's gearbox, where SMA spring actuates a thermostatic mixing valve to adjust the oil level in the gearbox via detecting the temperature [2,11].

Cardiovascular stents and filters, minimally invasive surgery devices, orthodontic braces and wires are several usages of SMAs in biomedical applications due to their superelastic properties [2]. There are also several civil industry applications to control the seismic response of a building, bridge or offshore platform. They are used as brace and/or washer spring type SMA components during earthquakes by their energy dissipation capability through large hysteresis with loading and unloading [7,8,12].

In aerospace industry, there are tough regulations worldwide on engine noise levels of the aircraft during landing and takeoff. Thus, chevron type components are integrated to engines to mix the exhaust gas flow and reduce the engine noise. There are SMA beams inside these chevrons which increases the mixing thereby reducing noise at low-speed or low-altitude flights. Additionally, they straighten the chevron and increase the performance of the engine since SMA beam components go into martensite due to cooling at high-speed or high-altitude flights. NiTi SMA beams have been utilized in Boeing 777 Variable chevron geometry to active control of the noise reduction [2,10]. There is another application where SMAs are used for satellites as low-shock release mechanism since gradual heating based slow actuation makes them more convenient [45]. Torque tube or beam plate forms of SMAs are usually used as actuation components to replace heavy weight pneumatics or DC motors in aerospace industry [4,10].

In applications of many industries, NiTi SMAs are most widely used and studied alloys among SMAs due to their outstanding mechanical and shape memory properties.

2.4. NiTi Based Shape Memory Alloys

SMA was first reported by Arne Ölander for Au-Cd alloy [46]. However, Equiatomic binary NiTi alloy showing SME was discovered at the U.S. Naval Ordnance Laboratory [47] and this discovery has a great impact on the use of these SMAs in real conditions as an active material. After that discovery, there have been several studies and commercial use of these alloys in different type of applications [5,6,8,10].

NiTi is the most widely commercially used and studied SMA due to its superior behaviors such as high ductility, strength, workability, biological compatibility, and resistance to corrosion [2,13,14]. Also, NiTi is appropriate for a variety of applications since it shows relatively higher SE, SME and TWSME under proper conditions [2].

A phase diagram of NiTi alloys created by Massalski was shown in Figure 2.4-1 [48]. NiTi could be decomposed into Ti_2Ni on the titanium-rich side and $TiNi_3$ on nickel-rich side.

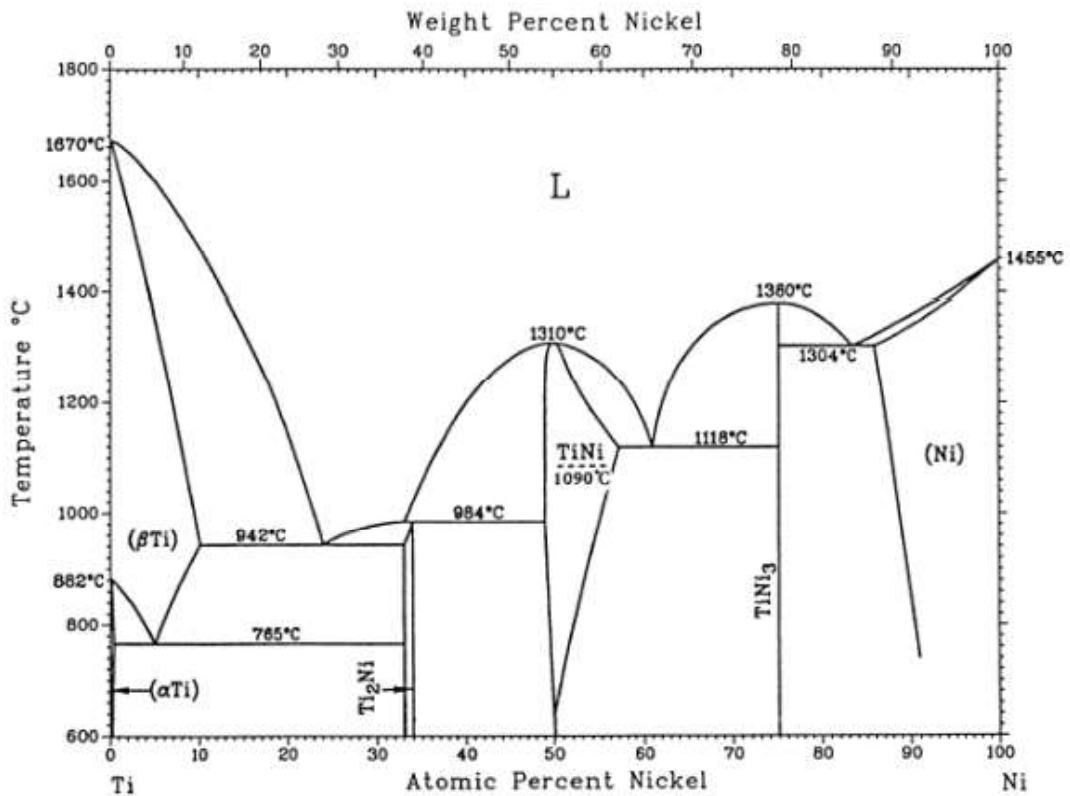


Figure 2.4-1. Phase diagram on NiTi by Massalski [48]

The alloy composition and thermomechanical treatments have significant impact on the transformation temperature (TT) values of the NiTi. If Nickel content in the matrix increases, it causes a decrease in TT values. Ni₄Ti₃ precipitate could be formed by aging treatment in Ni-rich NiTi alloys. However, precipitates can not be formed by aging treatments in near equiatomic NiTi alloys [49]. Ni₄Ti₃ precipitates formed in Ni-rich alloys leads to the loss of Ni from the matrix which results to observe higher TT value. However, in Ti-rich alloys, Ti₂Ni precipitates can be formed by aging treatment and these precipitates do not affect TTs, since Ti₂Ni precipitates keeps the Ni content of the matrix at equilibrium state. Additionally, Ti₂Ni precipitates are generally observed in oxide forms (Ti₂NiO types) which are detrimental to the ductility of the alloys.

NiTi alloys exhibit SE and SME behaviors between austenite phase with B2 (cubic) crystal structure and martensite phase with B19' (monoclinic) crystal structure. MT could also occur in multiple steps after running thermal cycles, thermomechanical treatments that are applied to near equiatomic NiTi alloys and aging treatment to Ni-rich NiTi alloys. This multistage transformation could happen from B2 to R-phase followed by R-phase to B19' [50]. NiTi alloys prefer this multistep transformation to decrease the energy that is necessary for the direct transformation of B2 parent phase to B19' martensite phase.

To strengthen the alloys, some methods to increase the critical stress for slip formation (CSS) could be used such as work/strain hardening by increasing dislocation density and/or refining grains, and precipitation hardening.

Strengthening of SMAs could be achieved via work hardening by applying cold rolling, extrusion, and thermomechanical treatments through increasing the dislocation density or refining the grains. Some of these work hardening processes are also helpful to induce texture to the alloys which leads to improve the mechanical and/or shape memory properties of the alloys as well [51,52]. There have been many studies regarding the strengthening of these alloys and improving their properties. Some of the studies are mentioned in the following paragraph.

Miller et al. investigated the effect of cold rolling (CR) and annealing temperature on the transformation behavior of equiatomic NiTi alloys [53]. They showed that, when the CR level increases, stress level to induce plastic deformation increases as well as decrease the plastic strain created during thermal and/or thermomechanical cycling. Also, Adharapurapu et al. [54] investigated the strengthening behavior of Ni-rich (Ni₅₅Ti) alloy upon aging. They found that the precipitation formation led to a significant improvement of the strength but to an embrittlement and low ductility. In addition to these studies, Saburi et al. [55] showed that the reducing the grain size is effective on improving the pseudoelastic performance. Increase in dislocation density or a decrease in grain size with the deformation processes cause an increase in the strength of the alloy. Therefore, the plastic deformation during phase transformation would be inhibited. However, it is worth to note that, deformation induced dislocations also decreases the mobility of the martensite-austenite phase since they act as pinning structures [56,57]. As the volume of the transformed phase decreases the actuation capability of the alloy decreases as well.

2.5. High Temperature Shape Memory Alloys (HTSMAs)

NiTi SMAs have several types of applications and one of the most extensively studied type of SMAs due to their special properties as mentioned in the previous section. However, they have limited transformation temperature below 100°C (<100°C).

SMA developments are mainly concentrated on applications with operating temperatures below 100°C due to the commercial applications of these alloys in the industries over the last decades. However, there is a trend using these alloys in envisioned applications of energy and aerospace industries which need SMAs operating at higher temperature values with stable material properties. Thus, there is a requirement for developing robust SMAs which could work at higher temperatures without losing their actuation capability and strength. This group of materials are called as High Temperature Shape Memory Alloys (HTSMAs).

The first study on the literature was reported by Donkersloot et al. on MTs of Au-Ti, Pd-Ti and Pt-Ti alloys which have very high TTs [58]. It is shown in this study that MT of

Ti-Pt occurred around 1,070°C. There are also binary alloys showing higher TTs as Ru-based binary Ta-Ru and Nb-Ru alloys which exhibit TTs up to around 1,400°C and 1,000°C respectively [59,60]. Although these binary alloys have very high TTs their actuation and work output capacities are considerably low.

In addition to mentioned binary HTSMAs, there are ternary HTSMAs. TTs of these SMAs are increased by alloying with ternary element addition to NiTi binary alloy. Au, Pd, Pt, Zr, Hf are used as ternary additional alloying elements in NiTi binary systems.

There is a study on TiNiAu alloys regarding the effect of Au addition to binary TiNi alloys. It is found that 40-50 at.% Au addition to NiTi showed transformation from B2 to orthorhombic B19 martensite as in binary NiTi. However, with 5-10 at.% of Au addition, transformation formed between B2 to B19' monoclinic structure. TTs for $Ti_{50}Ni_{10}Au_{40}$ and binary $Ti_{50}Au_{50}$ were shown around 470°C and 640°C respectively [61].

Furthermore, in the Pt addition as a ternary element, addition of more than 10 at.% Pt linearly elevates TTs. In contrast, TTs decrease while addition of Pt is below 10 at.% Pt [62]. It is shown that, MT happens from B2 to orthorhombic B19 martensite when Pt addition is around 30 at.% Pt. It is also important to note that R-phase was found in $Ti_{50}Ni_{30}Pt_{20}$ as an intermediate phase between B2 to B19' [63].

Adding Pd to NiTi binary alloy is more effective than Pt addition in increasing TTs [63]. Less than 10 at.% of Pd addition to NiTi decreases TTs as in the case of Pt addition. MT happens between B2 to B19' monoclinic structure in this condition. It is shown that R-phase was also found in $Ti_{50}Ni_{45}Pt_5$ during MT [63]. Pd addition has similarities with Pt addition. Adding more than 10 at.% of Pd increase the TTs and MT happens through B2 to orthorhombic B19 martensite transformation.

NiTiPd alloys have poor shape memory behavior at relatively higher temperatures since the CSS decreases noticeably with increasing temperature. Thus, plastic deformation could occur under lower loads during phase transformation before martensite

reorientation. Basically, NiTiPd alloys starts yielding before the reorientation of martensite [1].

Among the above-mentioned elements as ternary additions to NiTi alloys, addition of Zr and Hf seems to be the most promising with respect to their cost advantages compared to Au, Pd and Pt alloys. Additionally, because of their success in altering TTs, they might be utilized in lower quantities with relatively higher effect on TTs [14].

NiTiHf and NiTiZr have similarities in their properties. MT occurs through the transformation of ordered cubic austenite (B2) phase and monoclinic martensite (B19') phase in NiTiZr and NiTiHf alloys [4]. Also, TTs of the alloys increase when higher than 10 at.% Hf or 10 at.% Zr elements are added to binary NiTi [4]. However, Hf is the most preferred ternary element since it is more effective in increasing TTs [4,13,15].

There are many studies in the literature investigating Ni-rich NiTiHf HTSMAs since they possibly contain precipitates leading to better mechanical and thermal stability. The precipitation formation could be achievable by aging heat treatment in Ni-rich HTSMAs which has Ni at.% of more than 50 in the matrix. These precipitates are named as H-phase precipitates [16,17]. Aging process results an increase of TTs due to reduction in the Ni content of the matrix [14].

Saghaian et al. [64] investigated different types of aging effect on the microstructure of Ni-rich $\text{Ni}_{51.2}\text{Ti}_{28.8}\text{Hf}_{20}$ by testing the aged samples under compression. They found that the H-phase precipitate size is significant in strength and MT of the material. Aging treatment at relatively low temperatures ($<500^\circ\text{C}$) led to the formation of smaller precipitates ($<15\text{nm}$) and lower interparticle distances, which improved the strength of the material since they could act as obstacles against dislocation motion. Also, Karaca et al. [16] worked with Ni-rich polycrystalline $\text{Ni}_{50.3}\text{Ti}_{29.7}\text{Hf}_{20}$ alloys and investigated the effects of various heat treatments to shape memory properties. They showed that aging treatment could be used to change precipitate size which directly affect the mechanical and shape memory properties. In their study, they applied various aging

temperatures with various aging time durations. They found that aging at 550°C for 3 hours provided better shape memory and mechanical properties compared to aging at 650°C for 3 hours. In addition to aging effect studies, Umale et al. [65] worked on the effect of composition variation on MT of NiTiHf alloys through investigation of NiTiHf alloys produced with different chemical compositions. They showed that wide range of TT (M_s) (ranging from -170°C to 500°C) could be obtained by varying composition of Ni and Hf content. Additionally, they also stated that Hf addition lower than 10 at.% did not result a significant increase in the TT of the alloy.

Compared to Ni-rich NiTiHf, equiatomic NiTiHf alloys with 20 at.% or higher Hf content exhibit higher TTs than that of Ni-rich NiTiHf alloys. Therefore, equiatomic NiTiHf alloys are also good alternatives especially for high temperature applications [18–22]. However, there are limited number of studies with equiatomic NiTiHf alloys. It is worth to note that Hf takes the positions of Ti atoms since they have similar sizes. Therefore, the at.% of Ni is approximately 50 and the at.% of Ti+Hf is also 50. This is the reason why the alloys having 50 at.% Ni and 50 at.% (Ti+Hf) are named as equiatomic in this study.

Babacan et al. [20] have investigations on the effects of cold and warm rolling process to shape memory properties of Ni₅₀Ti₃₀Hf₂₀ alloys. It is shown in their work that the optimum thermomechanical treatment condition for achieving the highest shape recoverability was %15 cold rolling process followed by annealing process. Additionally, Akgul et al. [21] conducted a study in which they worked with Ni₅₀Ti₃₀Hf₂₀ alloy to investigate cooling rate effect on shape memory characteristics. They found that the TTs of the samples are independent on differences of cooling rate. Other studies using equiatomic NiTiHf is briefly mentioned in the next chapter since they are related to fatigue behavior of these materials.

2.6. Fatigue of HTSMAs

Fatigue is a failure mechanism causes serious catastrophic problems to components under repetitive load application. There had been severe failures due to fatigue that were

reported in the 19th century, and the mechanism of these failures was not known-well in the early history of the materials science since the failure could not be observed when happening and it had occurred suddenly without warning. Thus, it was an important technical problem people need to have awareness of.

First valuable research regarding fatigue was made by Wöhler in which he saw that a single load below the yield strength of material could damage the structure when it was repeated many times. In 20th century, it was recognized that a fatigue mechanism starts with a nucleation of crack in the material, then a crack growth stage occurs and is followed by sudden failure by fracture at the end [66].

In typical engineering materials, structural fatigue is due to dislocation accumulation leading to start crack formation. Formed cracks propagate in the fatigue crack growth period, then the fatigue failure occurs by fracture at the end. This happens when the material is subjected to cyclic load. However, there is another type of fatigue behavior that should be considered in SMAs. Rather than cyclic load change as in typical structural fatigue, repetitive phase transformation under constant load which takes place by heating-cooling cycles and/or repetitive phase transformation which takes place by loading and unloading are two main mechanisms in investigating the fatigue of SMAs [23].

If the fatigue that occurs in SMAs causes deterioration of the functional properties it is defined as functional fatigue. There are two types of functional fatigue when the activating mechanism for phase transformation is considered such as pseudoelastic fatigue and actuation fatigue [23].

Pseudoelastic fatigue is also called as isothermal fatigue that is caused by stress induced phase transformation by cyclic mechanical loading at constant temperature. However, actuation fatigue occurs by performing heating-cooling cycles under constant mechanical load [23]. The fatigue studies are mostly focused on pseudoelastic fatigue of NiTi binary SMA on the contrary to actuation fatigue [24–28]. It is important to state that, conducting

thermal cycles on HTSMAs is pretty difficult since the heating-cooling cycles should be conducted at very high temperatures.

Experimental investigations regarding actuation fatigue are only in few numbers in the literature. There are studies in the literature investigating the testing parameters on actuation fatigue such as Upper Cycle Temperature (UCT) effect [18] and applied load level [29]. UCT is the upper limit temperature to which the samples are heated to observe the full austenite transformation in actuation fatigue experiments. UCT can be set to a temperature a little higher than A_f temperature of the alloy or can be set relatively higher than A_f of the alloy. There are some studies as well regarding the effect of heat treatment on the shape memory properties of the alloy [22], the evolution of microstructural damage during actuation fatigue [23] and, corrosive environment effect on actuation fatigue properties [30].

In the work of Karakoc et al. [18], they investigated the UCT effect on the fatigue life and actuation strain in nano-precipitation hardened $Ni_{50.3}Ti_{29.7}Hf_{20}$ (at.%) alloy. 300°C and 350°C UCTs were used and the samples were kept under 300 MPa constant load in the work and they found that the difference between the strain values at martensite and austenite which has been called as actuation value was increased with increasing UCT level. Additionally, they showed the fatigue life was decreased with increased UCT value in stated conditions.

Also, Karakoc et al. [29] had a work on the effect of stress magnitude on functional fatigue (actuation fatigue) behavior of the same alloy. Different stress levels (200 MPa, 300 MPa, 400 MPa and 500 MPa) were applied to $Ni_{50.3}Ti_{29.7}Hf_{20}$ (at.%) alloys which were aged at 550°C for 3h. They showed that the actuation value was increased with increasing stress level. However, actuation strain value was decreased by the increased number of cycles due to generated dislocations for all levels of stress application.

In a different study by Akin et al. [22], the effect of additional heat treatment on cyclic stability and fatigue properties of $Ni_{50}Ti_{30}Hf_{20}$ alloy was investigated via running

functional fatigue cycles. Samples were initially in hot extruded form and the hot extruded sample was later annealed at 550°C for 3 hours. They found that the post annealing process eliminated the deformation variations and internal stresses induced by hot extrusion process and led to obtain very consistent and similar shape memory properties. Additionally, the all actuation properties such as actuation strain magnitudes, and TTs became more stable and the fatigue life increased after annealing heat treatment and surface polishing.

Determining fatigue behavior is important since SMAs are used as actuators which are produced to work under cyclic loads. Fatigue crack growth investigations with phase transformation induced by heating-cooling under constant load are limited in literature especially for NiTiHf HTSMAs. It is hard to determine fatigue crack growth behaviour during actuation application since the approaches of fatigue crack growth based on developed models and theories for structural metals with showing no phase transformation [31].

There are total-life (safe-life) design approach (TLA) and damage-tolerant design approach (DTA) to investigate the fatigue. There is an already initiated crack in a structure of DTA design and its resistance to crack growth with cyclic loading is being considered. However, total-life approach is based on an initial flawless part assumption. There have been relatively more studies in the literature on TLA design due to the fact that small-sized SMAs are used in the commercial market such as NiTi implants. In small sized components, failure occurs at a short time after crack nucleates. Thus, preventing crack nucleation is more significant than controlling the crack growth in biomedical applications considering the TLA approach [32].

DTA is more proper to use when the part is large enough to keep the functionality and crack growth stable, in the presence of defects during the service period of the parts/components. Therefore, it is more proper to apply this approach to SMA actuators while investigating the crack growth since they usually work under constant loads as functional materials. However, application of DTA on SMAs is different and more difficult than that of conventional metals due to the fact that reversible phase

transformation, martensite reorientation and thermomechanical coupling are main points of consideration in crack growth investigations in SMAs [32,33].

There are limited number of studies working experimentally on crack growth during actuation fatigue.

By using NiTi alloys in wire form, Ramaiah et al. [36] conducted actuation fatigue experiments under load. They showed that many surface cracks initiated by thermal cycling followed by simultaneous crack propagation of these cracks inward the material did not lead to fracture alone. They found that crack generation at the core of the material is highly important in fracture and crack generation at the core was occurred by strain inhomogeneity in the core of the wire due to temperature gradient appeared across the wire section during thermal cycles.

Iliopoulos conducted experiments on actuation cycling under load with double notched Ni₆₀Ti₄₀ (at.%) specimens. They found that fracture occurs due to unstable crack propagation during cooling mostly occurred in the first cooling cycle [37]. Jape et al. [38] had experiments on actuation cycling of pre-notched Ni_{49.5}Ti_{50.5} (at. %) compact tension specimens (CT) and showed that crack grows during cooling.

Kockar's group [67] worked on crack growth behavior during actuation cycling under constant load in pre-notched Ni₅₀Ti₃₀Hf₂₀ (at. %) samples. They investigated the crack growth and shape memory properties of two groups of samples. First group was as hot-extruded samples and the second group was hot extruded and then post annealed samples at 550°C temperature for 3 hours. They investigated the effect of annealing heat treatment on the crack growth behavior of pre-notched Ni₅₀Ti₃₀Hf₂₀ (at.%) HTSMA during actuation fatigue and showed that the growth rates of the major crack in annealed samples were lower and it was relatively easier to create new minor side crack formations in annealed samples with spending less energy.

2.7. Creep

Creep behavior of materials classically related to time-dependent plasticity due to a fixed stress at elevated temperature values.

Creep occurs in three stages under constant stress as primary creep - stage 1, secondary creep - stage 2 and tertiary creep - stage 3. As in primary creep stage, creep rate ($\dot{\epsilon} = \frac{d\epsilon}{dt}$) is changing and decreasing by time. In secondary creep stage, creep rate becomes steady. Then, creep rate accelerates eventually due to cracking and lead to fracture in tertiary stage [68]. In stage 1, the dislocation formation rate is higher than that of the dislocation annihilation rate, therefore, the material is strain hardening. In stage 2, the rate of dislocation formation and annihilation becomes same, thus the creep rate becomes steady.

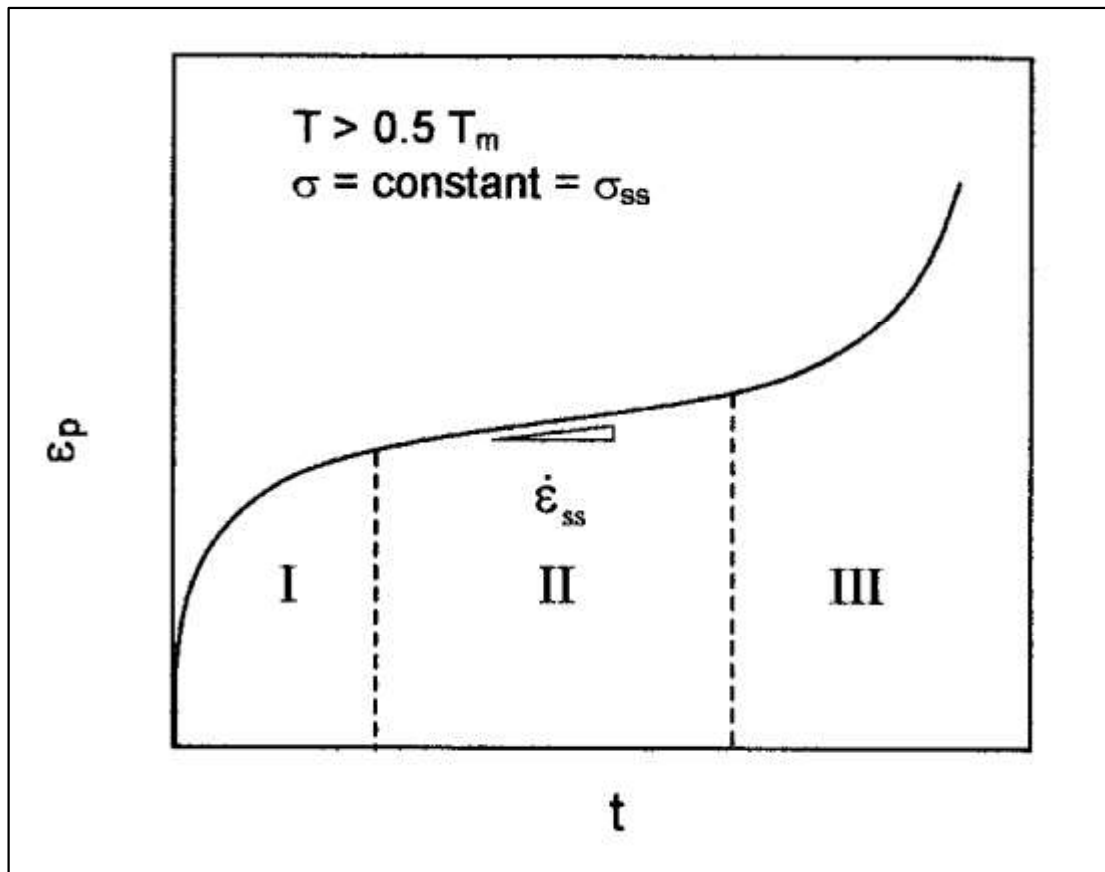


Figure 2.7-1. Schematic of a true strain vs time curve in metals under constant stress [68]

In SMAs as actuators, actuation fatigue experiments conducted between UCT and LCT under constant load. During the tests, actuation strain values decrease and accumulated

irrecoverable strain values increase over the cycles. However, higher UCT leads to an increase in actuation strain as well as accumulated irrecoverable strain values. The increase in actuation strain is due to the increase in the transforming volume with the increase in UCT and the increase in accumulated irrecoverable strain might be due to the dislocation formation by plastic deformation via phase transformation and/or creep-based plasticity over the cycles due to higher temperature values.

There are very limited number of studies in the literature about the creep behavior of NiTi SMAs and NiTi based ternary HTSMAs. In those few studies, creep experiments under different constant load magnitudes and different temperature levels with NiTi alloys were done. Firstly, Mukherjee studied creep behavior of NiTi alloys with constant strain-rate tests at 6 different temperatures which were between 700-1,000°C [69]. They calculated the stress exponent as 3 and activation energy value as 251.4 kJ/mol. They found that the stress exponent showed viscous creep deformation which was temperature independent in addition to calculated activation energy was not stress dependent.

Then, Lexcellent et al. [34] had creep experiments with NiTi and measured the strain rates at 600-900°C temperature levels under constant tensile load between 10-35 MPa. They found stress exponent as 3 and activation energy as 226 kJ/mol that agreed with the values obtained by Mukherjee et al. However, they compared the calculated activation energy value with Ni tracer-diffusion value which was found as 155 kJ/mol before in the literature [70]. By comparing the value, they concluded that Ti was the slower diffusing component with higher activation energy.

Oppenheimer et al. [71] worked at higher temperature levels (950-1,100°C) with near-equiatomic NiTi under low stress magnitudes (3-11 MPa) with compression load to measure the creep rates. They found the stress exponent and activation energy as 2.7 and 150 kJ/mol, respectively. They concluded the difference on these values with previous studies might be due to some variables affecting creep such as compression/tension asymmetry, precipitate and texture presence. Additionally, Kumar et al. [72] worked with Ti_{50.5}Pd₃₀Ni_{19.5} (at.%) alloy under 100-300 MPa constant stress at (300-400°C) temperature to calculate creep parameters. They investigated the effect of heating rate to

the creep rate of the alloy and found that as the heating rate increased the creep rate increased noticeably. However, they just worked on the heating rate effect. Also, Chaugule et al. [73] used $\text{Ni}_{49.8}\text{Ti}_{30.6}\text{Hf}_{19.2}$ (at.%) alloy to investigate creep plasticity and transformation induced plasticity (TRIP). They worked on both constant load creep experiments and thermal cycling experiments under constant load with different heating-cooling rates. They found that the creep viscoplasticity was considerably lower than that of TRIP at actuation fatigue experiments.

Tugrul et al. [35] worked with $\text{Ni}_{50}\text{Ti}_{25}\text{Hf}_{25}$ (at.%) alloys to investigate creep deformation under tensile loads at different temperature levels (450°C - 550°C - 600°C) under different tensile stress magnitudes (200 MPa to 500 MPa). They showed that there was almost no creep strain occurred at 550°C and 600°C temperature under 200 MPa and 300 MPa strain level. Also, they showed that no primary creep formation occurred on annealed $\text{Ni}_{50}\text{Ti}_{25}\text{Hf}_{25}$ (at.%) samples creep tested with 600°C . In addition to those stated works regarding the creep deformation under NiTi based and NiTi ternary HTSMAs, there is no work regarding the crack formation and crack propagation during creep in NiTiHf HTSMAs.

3. EXPERIMENTAL METHODS

3.1. As-received material

The production details of the alloys that were used in this study were explained below in this chapter. It is important to mention that the percentages of the elements have been given in atomic weight percentages (at.%) throughout the text of this thesis. $\text{Ni}_{50}\text{Ti}_{30}\text{Hf}_{20}$ (at.%) and $\text{Ni}_{50}\text{Ti}_{25}\text{Hf}_{25}$ (at.%) HTSMAs were used to investigate the crack growth behavior of NiTiHf alloys.

These two alloys were produced by melting high purity elemental materials of Nickel, Titanium and Hafnium via purging high purity argon atmosphere and casting with utilizing vacuum induction melting (VIM) method. After VIM process, the cast ingot was sealed in a mild steel can, to reduce the friction between the extrusion die and the material surface and to inhibit the severe oxidation during the hot extrusion process. Then, the cast ingot was hot extruded at 900°C into a rod as shown in Figure 3.1-1 (a) with an area reduction of 4:1. Hot extruded rod was machined via utilizing a lathe to remove the cast layer (Figure 3.1-1 (b)). The rod was sliced into dog-bone shaped samples as presented in Figure 3.1-1 (c) via using Agie Charmilles CUT 300 Wire EDM that was presented in Figure 3.1-1 (d).

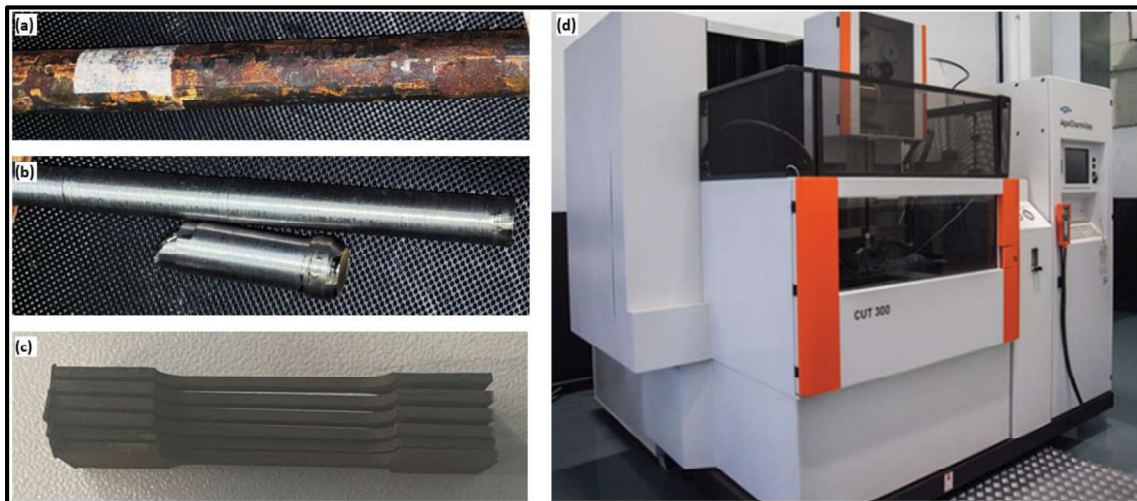


Figure 3.1-1 (a) Hot-extruded $\text{Ni}_{50}\text{Ti}_{30}\text{Hf}_{20}$ (at. %) HTSMA bar, (b) machined bar, (c) Sliced pieces by Wire EDM, (d) Wire EDM machine

3.2. Sample Preparation

Dog-bone shaped Single Edge Notch Test (SENT) samples were tested in actuation fatigue experiments. Dimension of the sample was determined according to ASTM E8 and scaled down into a smaller size proportionally since it is difficult to find and produce these shape memory alloys in large volumes due to the very high prices of the each material. SENT samples were cut from hot extruded material into samples of 1 mm thickness with a gage length of 16.6 mm and width of 2.25 mm. Then, a notch was formed with a 0.40 mm width and 0.30 mm depth which was perpendicular to the test loading direction (stated as lateral axis (X) in Figure 3.2-1). The sample dimensions were drawn as shown in Figure 3.2-1.

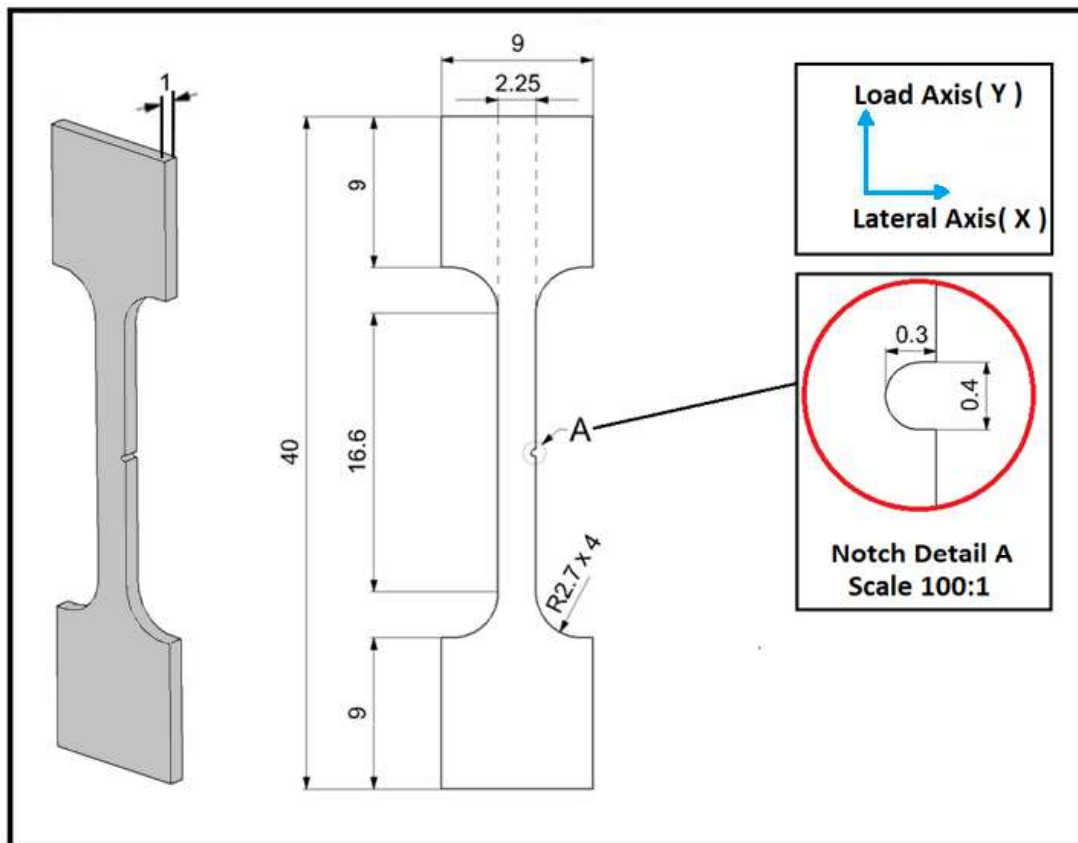


Figure 3.2-1. Representation of sample and pre-notch dimensions [67]

Wire electrical discharge machine (Wire EDM) was operated on sample cutting and notch forming to minimize the residual stresses on the cutting surface occurred during the process.

Actuation Fatigue experiment test samples of $\text{Ni}_{50}\text{Ti}_{30}\text{Hf}_{20}$ (at.%) alloys were separated into three groups such as as-extruded, as extruded and pre-notched, and as extruded, pre-notched and annealed samples. Hot extruded sample, hot extruded pre-notched samples and hot extruded, annealed and pre-notched samples were coded as “HE”, “HE-PN” and “HE-PN-AN”, respectively throughout the text. Additionally, since $\text{Ni}_{50}\text{Ti}_{25}\text{Hf}_{25}$ (at.%) alloy was annealed before the experiments HE-PN-AN code was also used for $\text{Ni}_{50}\text{Ti}_{25}\text{Hf}_{25}$ (at.%) as well.

Annealing process was applied on HE-PN-AN samples by using a vertical cylindrical furnace as shown in Figure 3.2-2. The sample was wrapped with tantalum foil to prevent potential severe oxidation during the process, and then it was annealed at 550°C for 3 hours under high purity argon atmosphere in the furnace.



Figure 3.2-2. Vertical cylindrical furnace

The annealing process and temperature were chosen by considering the studies by our research group since 550°C corresponds to approximately $0.5T_{\text{melting}}$ of the alloy which is reasonable to overcome the deformation variation and to relieve the irregular internal stress which might possibly induced during extrusion. Akin et al. worked on $\text{Ni}_{50}\text{Ti}_{30}\text{Hf}_{20}$ (at.%) alloy and stabilized actuation properties, similar TTs and increased fatigue life were observed after the application of annealing process at 550°C for 3 hours [22].

Grinding process was done to sample surfaces with 600-800-1,000 and 1,200 grit sized grinding papers before conducting experiments to eliminate Wire EDM based residual layers and micro cracks as much as possible.

Before actuation fatigue experiments, there is a need to determine the transformation temperatures of the sample since the actuation cycling will be done regarding the TTs. “Perkin Elmer 8000” differential Scanning Calorimeter (DSC) has been used under no load condition to determine the transformation temperature and enthalpy values for the same batch of $\text{Ni}_{50}\text{Ti}_{30}\text{Hf}_{20}$ (at.%) and $\text{Ni}_{50}\text{Ti}_{25}\text{Hf}_{25}$ (at.%) alloys.

3.3. Actuation Fatigue Test set-up and Applied Tests

Actuation fatigue experiments were performed by using actuation fatigue test set-up. Heating-cooling cycles have been run under constant load condition by hanging dead weights to the bottom grip of the set-up. In the beginning of the experiments, it has been aimed to apply 200 MPa stress magnitude. Therefore, constant load magnitudes were kept between 440 N – 468 N regarding the cross section of the sample. It is worth mentioning that, there were very small variations in load magnitudes regarding the gage section dimension of the samples. In addition to 200 MPa initial constant load condition, 300 MPa stress magnitude which refers to 654 N was applied to HE-PN-AN coded $\text{Ni}_{50}\text{Ti}_{30}\text{Hf}_{20}$ (at.%) sample.

Actuation fatigue experiment test set-up and representation of schematic diagram are shown in Figure 3.3-1 (a) and Figure 3.3-1 (b), respectively.

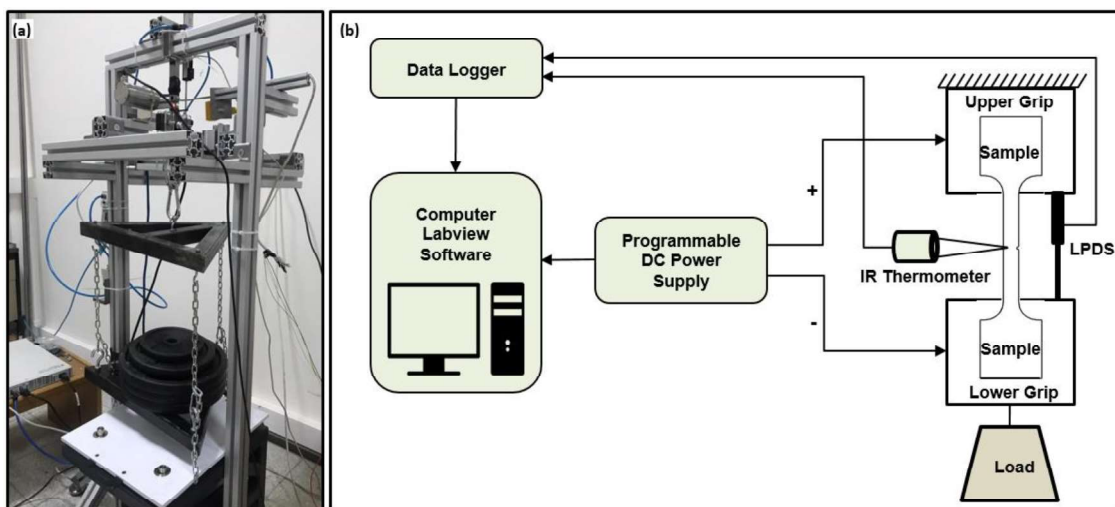


Figure 3.3-1 (a) Actuation fatigue experiment test set-up, (b) schematic diagram [74]

While heating of the sample was done by Joule Heating in which current passes through the sample, cooling was occurred by conventional open-air cooling. Cooling-heating rate of the samples was kept constant as 15°C/s during heating-cooling cycles.

Displacement measurements during heating-cooling cycles were made with a linear potentiometric displacement sensor (LPDS) which is mounted to the bottom grip of the test set-up. An infrared pyrometer (Optris Ct Laser LTF-CF1) was fixed at a position where it had focused on to the middle of the sample closer to the notch. Temperature value of the test sample was determined by converting the measured value by using thermal emissivity value which must be known while using infrared pyrometer. However, NiTiHf thermal emissivity value is not known. Therefore, high temperature resistant black paint (MOTIP Heat resistant paint) was sprayed onto the sample measurement area to measure the temperature accurately during actuation fatigue tests since its thermal emissivity value was known as 0.95.

National Instruments USB-6003 data logger was used to record the displacement and temperature data during test cycles.

Highest temperature value set to heat the samples during heating-cooling cycle and the lowest temperature value set to cool the samples are called as upper cycle temperature (UCT) and lower cycle temperature (LCT), respectively. The UCT, LCT and cooling-heating rate parameters were set in the Labview Software which controls all these test parameters during the actuation fatigue experiments.

UCT and LCT set temperature values for samples were determined as 440°C, 150°C respectively via considering the TTs that were measured by using DSC. In addition to these tests, to see the effect of higher UCT on actuation fatigue, another Ni₅₀Ti₃₀Hf₂₀ (at.%) sample in HE-PN-AN condition was tested for UCT and LCT values of 600°C and 150°C, respectively. Additionally, HE-PN-AN coded Ni₅₀Ti₂₅Hf₂₅ (at.%) sample was tested at higher UCT and LCT values which were pre-set as 600°C and 200°C, respectively. Table 3.3-1 represents the sample types and the corresponding sample numbers together with the testing parameters.

Table 3.3-1. Actuation Fatigue Test Sample Types and Testing Parameters

Sample Groups	Sample Type	Sample Numbers	Testing Parameters
1	HE (Without pre-notch)	Sample 1	Ni ₅₀ Ti ₃₀ Hf ₂₀ (at.%)
			initial constant load refers to 200 MPa
			UCT – LCT: 440°C – 150°C
			15°C/s heating-cooling rate
2	HE-PN	Sample 2	Ni ₅₀ Ti ₃₀ Hf ₂₀ (at.%),
		Sample 3	initial constant load refers to 200 MPa
		Sample 4	UCT – LCT: 440°C – 150°C
			15°C/s heating-cooling rate
3	HE-PN-AN	Sample 5	Ni ₅₀ Ti ₃₀ Hf ₂₀ (at.%)
		Sample 6	initial constant load refers to 200 MPa
			UCT – LCT: 440°C – 150°C
4	HE-PN-AN	Sample 7	Ni ₅₀ Ti ₃₀ Hf ₂₀ (at.%)
			initial constant load refers to 200 MPa
			UCT – LCT: 600°C – 150°C
			15°C/s heating-cooling rate
5	HE-PN-AN	Sample 8	Ni ₅₀ Ti ₃₀ Hf ₂₀ (at.%)
			initial constant load refers to 300 MPa
			UCT – LCT: 440°C – 150°C
			15°C/s heating-cooling rate
6	HE-PN-AN	Sample 9	Ni ₅₀ Ti ₂₅ Hf ₂₅ (at.%)
			initial constant load refers to 200 MPa
			UCT – LCT: 600°C – 200°C
			15°C/s heating-cooling rate

In actuation fatigue experiments, multiple sequential cycles were included. Strain vs Temperature curve that is drawn for one heating-cooling cycle fatigue experiment was schematically shown in Figure 3.3-2. Actuation fatigue-shape memory properties were determined from these curves as explained in the following paragraph.

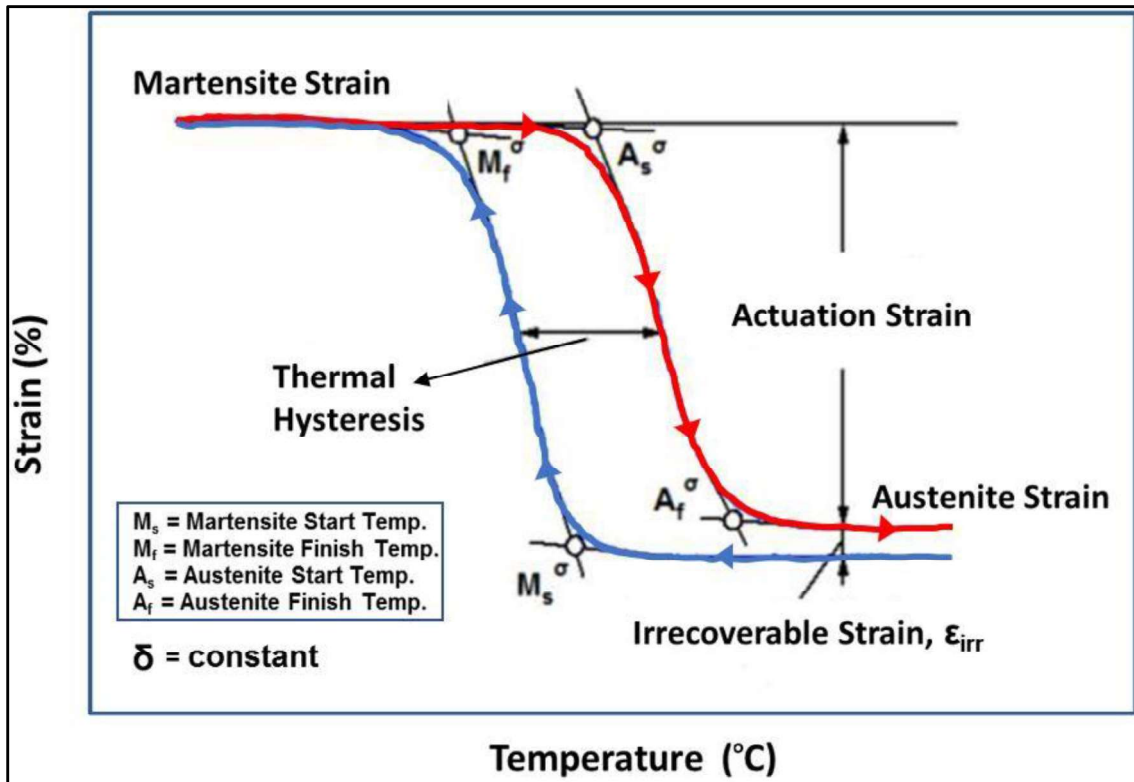


Figure 3.3-2 A schematic curve of an actuation fatigue (heating-cooling) test cycle under constant load and determining the values as TTs, actuation strain, irrecoverable strain and thermal hysteresis [18]

In the beginning of the tests, sample was heated to UCT to keep it in the austenitic phase, then dead weight was loaded. Thus, the starting temperature point of the experiment was UCT at lower strain value. After that, cooling-heating cycles were done between UCT to LCT values with a certain heating-cooling rate which was 15°C/s during the tests. Austenite strain and martensite strain were defined as strain value at austenite phase and strain value at martensite phase respectively. Actuation strain value was defined as strain difference between austenite strain and martensite strain. Functioning property of the SMAs and work being produced against the loaded dead weights were presented by the actuation strain value.

The difference between the starting strain and finishing strain at UCT in a cycle, is called as Irrecoverable Strain which corresponds to remained shape change. The accumulation of irrecoverable strain from each heating-cooling cycle was stated as austenite strain up to given cycle. Additionally, TT values and thermal hysteresis values were extracted from the representing points as shown in Figure 3.3-2 at each representing cycle.

During the actuation fatigue experiments, the experiment was stopped to detach the sample from the set-up at each determined intermittent cycle and optical micrographs were taken to show the rate of crack propagation. However, since there was no lifting and loading/unloading mechanism in test set-up, sample would have been exposed to elevated temperatures for long time until loading/unloading was finished. Besides, manual loading of weights is pretty hard to do alone and takes longer times. Therefore, a lifting mechanism was designed, produced and integrated to test set-up. Mechanism consisted of main components such as welded main lifting body with guide shafts and wheels, lift plate with bushings and hydraulic jack as shown in Figure 3.3-3.

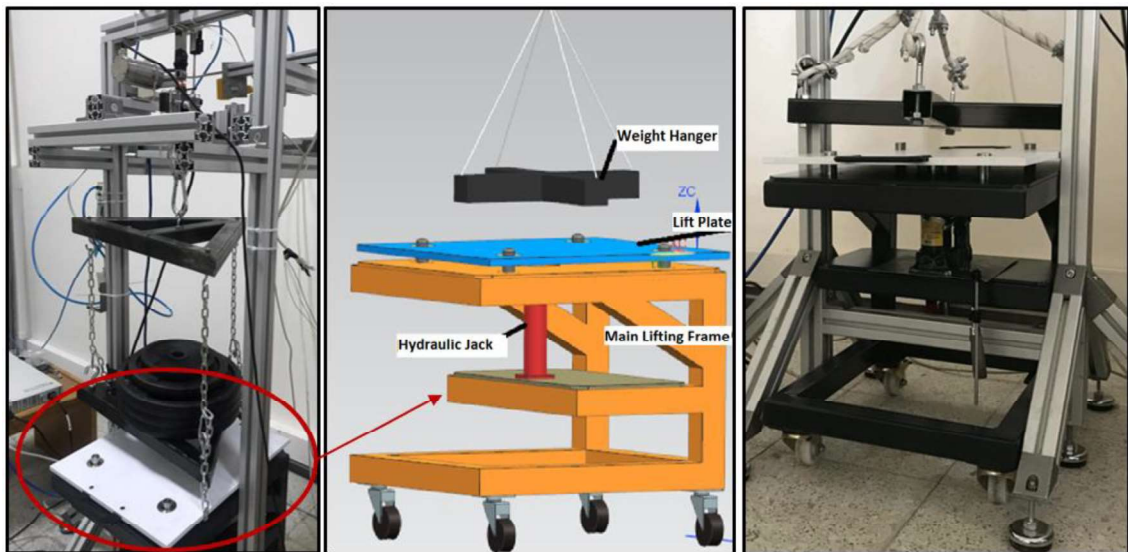


Figure 3.3-3 Additional lifting mechanism integrated to test setup

Additionally, new type of weight hanger was designed and produced to have more space for placing the weights easily and to be able to load the samples with higher magnitude loads as shown in the same figure. Hanger that has the triangle form was produced to put more weights in between two similar hangers. Length adjustable chains with hooks were

adapted instead of ropes which led to have more rigid and distance adjustable weight hangers.

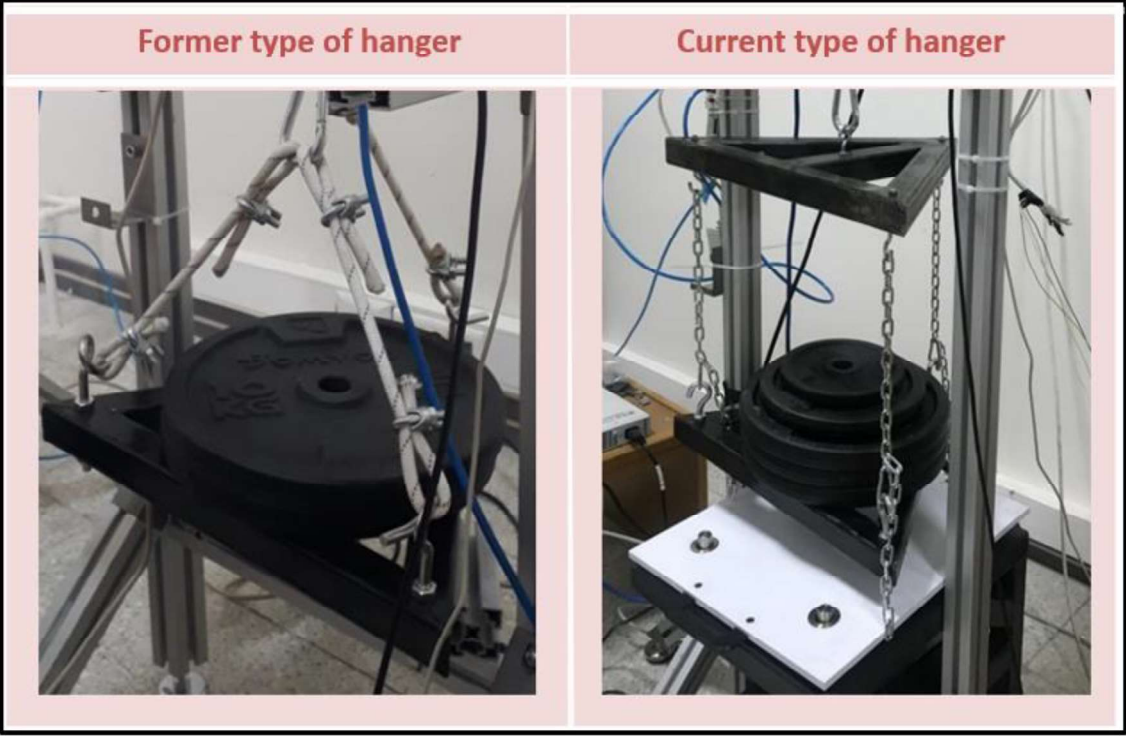


Figure 3.3-4. Former type of weight hanger and current type of weight hanger after test set-up improvement

The weights drop down after the failure of the samples and this causes bending of the lower grip, which could directly affect the testing stability, as represented in Figure 3.3-5. Crane lifting slings were integrated to experimental setup to cope with this problem. In this way, lower grip could be caught by those slings without being deformed when dropped after fracture.

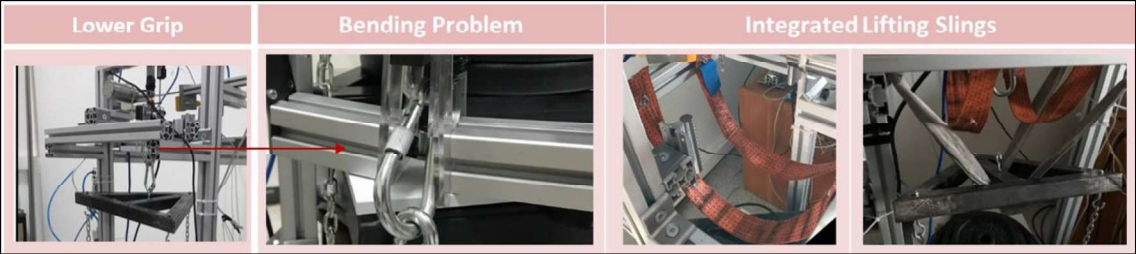


Figure 3.3-5. Integrated lifting slings in test set-up to catch the dropping lower grip and weight hanger

In addition to actuation fatigue experiments, creep experiments were conducted on HE-PN-AN Ni₅₀Ti₃₀Hf₂₀ (at.%) samples with the same actuation fatigue test set-up. Experiments were done under 3 different initial constant loading conditions such as 654 N, 890 N and 1087 N that correspond to 300 MPa, 400 MPa and 500 MPa stress magnitudes, respectively.

Creep experiments were set to be performed at 600°C that was used as UCT in actuation fatigue experiment which is approximately equal to half of melting temperature value in Ni₅₀Ti₃₀Hf₂₀ (at.%). Also, in a work investigated by our lab group, creep behavior of an equiatomic Ni₅₀Ti₂₅Hf₂₅ (at.%) were investigated at different temperatures and it was seen that these alloys didn't show noticeable creep strain at temperatures below 600°C [35]. Surface cracks during the creep tests were also investigated at intermittent cycles by using optical microscope.

3.4. Optical Microscope Analysis and Fracture Surface SEM Images

Nikon Eclipse LV 150 optical microscope that is shown in Figure 3.4-1 was used to observe and investigate the cracks, pre-notch and surface of the sample. Optical images were taken using microscope and then dimension measurements of crack and pre-notch were done using Clemex Vision Lite software that is cooperated with the microscope before tests, after each intermittent cycles and after failure. Additionally, during the intermittent cycles of creep experiments surface images were taken by optical microscope.

In addition to optical microscope analysis, fracture surfaces of some failed samples from each testing condition were investigated by using SEM Phenom – XL SEM to reveal the fracture modes of the samples.

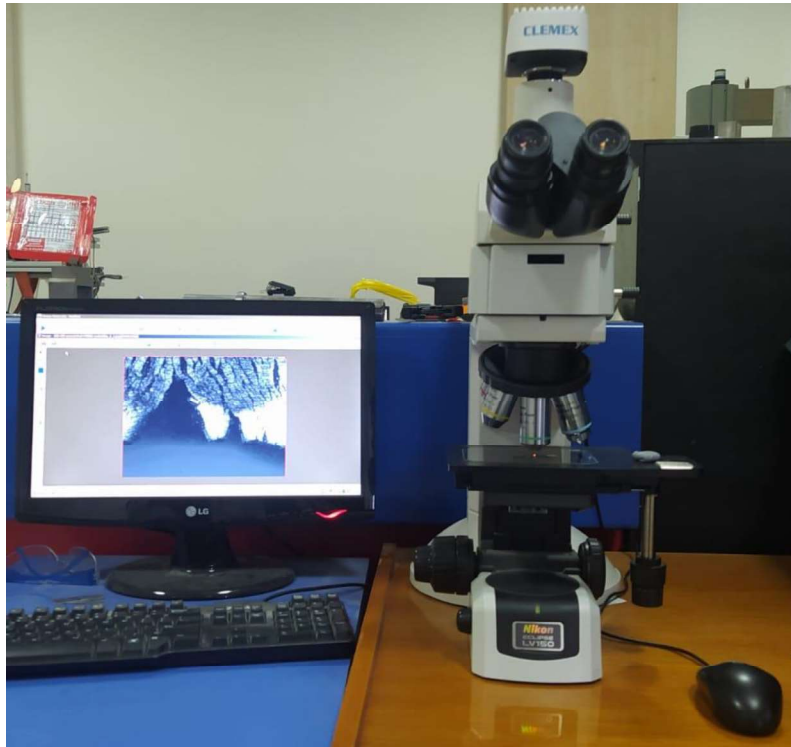


Figure 3.4-1. Nikon Eclipse LV 150 optical microscope

3.5. Stress Intensity Factor (SIF) calculation

After intermittent heating-cooling actuation cycles, crack lengths were measured using Clemex Vision Lite software from the optical images that were taken with the optical microscope at various magnification levels. The notch dimensions from the crack length measurements were used to determine the stress intensity factor for all samples, which is related to the rate of crack growth and displays the intensity of the stress distribution at the fracture tip. Equation 2 demonstrates that stress intensity factor K , which is directly related with the applied stress (σ), geometric factor ($F(a/b)$), and square root of defect size [32,75]. The remote loading stress (σ), was chosen as the applied constant nominal stress value during actuation fatigue tests. There are numerous equations for SIF calculations regarding different crack and sample geometries and loading conditions. The stress intensity and geometric factor values in this study were determined based on the empirical relationships indicated in Tada-Paris-Irwin's Stress Analysis of Cracks, which Tada defined in 1973 [66,75].

$$K_I = \sigma \sqrt{\pi a} F\left(\frac{a}{b}\right) \quad (\text{Equation 2})$$

In Equation 3, the geometric factor function, denoted as $F\left(\frac{a}{b}\right)$, was chosen for single edge notched samples where a is the length of the crack and b is the sample width.

$$F\left(\frac{a}{b}\right) = 0.265 \left(1 - \frac{a}{b}\right)^4 + \frac{0.857 + 0.265\frac{a}{b}}{\left(1 - \frac{a}{b}\right)^{3/2}} \quad (\text{Equation 3})$$

In calculating the SIF, when a/b is equal to or more than 0.2, this equation is stated to offer accuracy better than 0.5%, and better than 1% when a/b is less than 0.2 [75].

During actuation cycles, a/b ratio determined by crack length measurements after every intermittent cycles, were usually less than or near to 0.2. Therefore, Equation 3 was chosen among other empirical formulas to calculate geometric factor values for which provides more accurate values.

4. RESULTS AND DISCUSSIONS

4.1. Actuation Fatigue Testing of HE Samples

Ni₅₀Ti₃₀Hf₂₀ (at.%) alloys were used to investigate the actuation fatigue performance and crack propagation behavior during actuation fatigue cycles.

Before starting the experiments, TTs of the alloys should be known to determine UCT and LCT values to see full transformation during the actuation cycles. TTs of Ni₅₀Ti₃₀Hf₂₀ (at.%) that were previously measured and reported by our lab group for the same batch of alloy from DSC experiments are shown in Table 4.1-1.

Table 4.1-1 Stress-free TTs of Ni₅₀Ti₃₀Hf₂₀ (at.%) alloys [22]

Stress-free TTs of hot extruded Ni ₅₀ Ti ₃₀ Hf ₂₀ (at.%)				
	A _f	A _s	M _s	M _f
Temperatures (°C)	330	286	282	236

Firstly, actuation fatigue test was conducted on as extruded Ni₅₀Ti₃₀Hf₂₀ (at. %) sample without a pre-notch. Sample was tested by applying thermo-mechanical cycling with 15°C/s heating-cooling rate under 200 MPa constant stress by hanging dead weights to sample.

Actuation fatigue experiment results of the sample were gathered from the displacement and temperature data during test cycles. Then, the displacement data were converted to strain and the strain-temperature curves were drawn by these data of the samples.

Strain - Temperature diagrams for the HE sample that was thermally cycled under 200 MPa were shown in Figure 4.1-1, which included the selected cycles until failure. The 7,699th cycle, which was the last cycle was also shown in the Figure. It is important

to note that the applied constant load corresponds to 200 MPa stress magnitude at the beginning of the experiments but the stress increases as the cross section of the samples decreases with the plastic deformation. However, constant stress terminology was used throughout the text of this thesis to be consistent with the terminology that is being used in the literature.

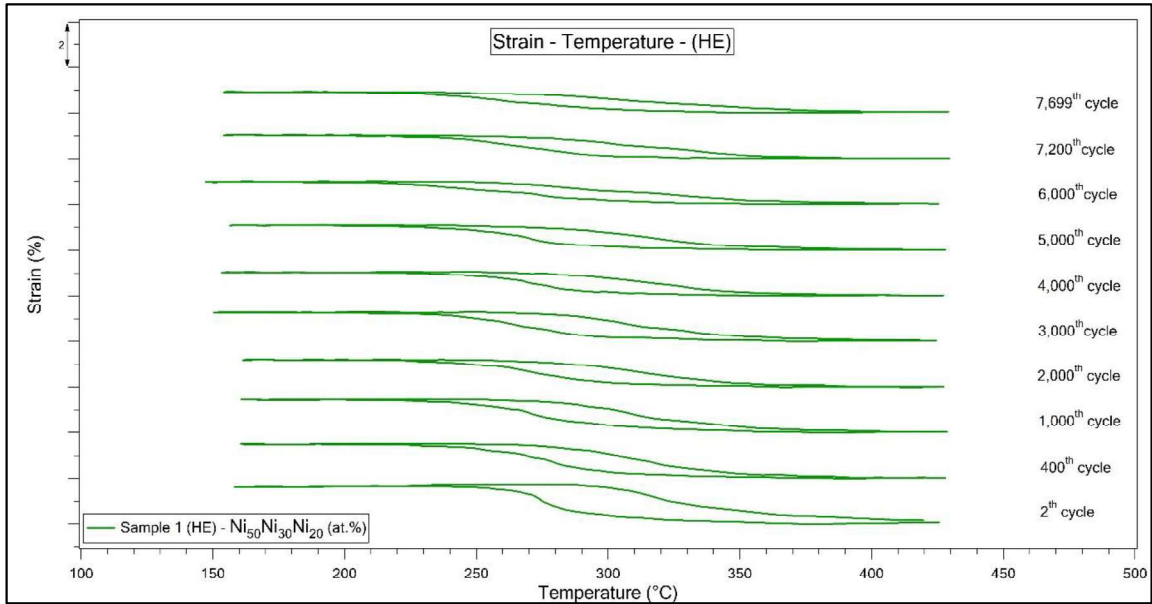


Figure 4.1-1. Strain-Temperature curves from the actuation fatigue experiment of Ni₅₀Ti₃₀Hf₂₀ (at.%) HE sample.

By using these curves, actuation fatigue properties of the materials such as actuation strain, accumulated irrecoverable strain, TTs and thermal hysteresis values were determined for all samples that were in different conditions. Extracting these properties was done by applying the procedure that was shown in Figure 4.1-2 and that was explained in the experimental procedure section for each correspondent cycle.

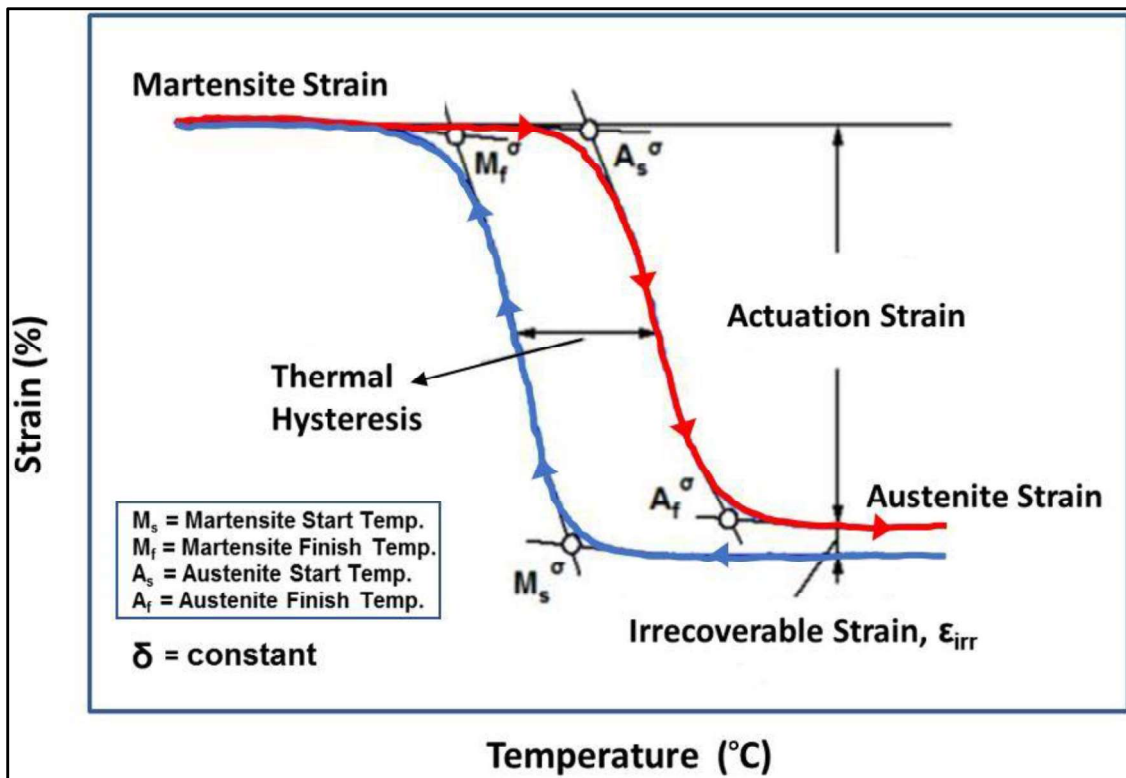


Figure 4.1-2. A schematic curve of a actuation fatigue (heating-cooling) test cycle under constant load and determining the values as TTs, actuation strain, irrecoverable strain and thermal hysteresis [18]

TTs that were determined from Strain vs Temperature curves of the HE sample, were shown in Figure 4.1-3. TTs were almost stable during the actuation fatigue test, however A_f showed a slight increase due to dislocation accumulation through the cycles. A_s , A_f , M_s and M_f temperature values were found as around 280°C, 350°C, 295°C, 250°C respectively.

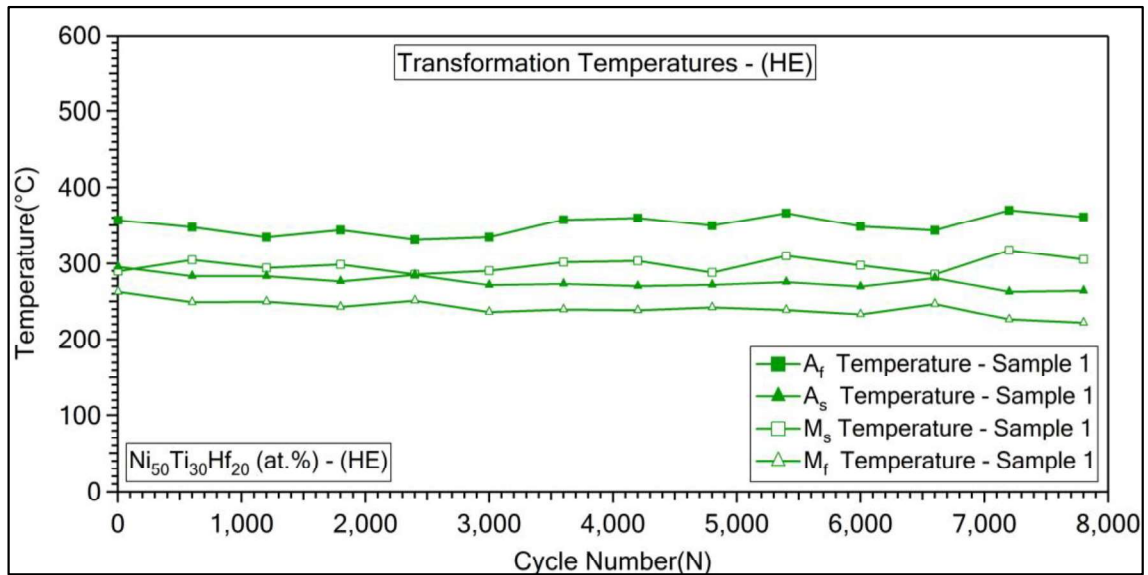


Figure 4.1-3. The evolution of the TTs that was determined from the actuation fatigue experiment of Ni₅₀Ti₃₀Hf₂₀ (at.%) HE sample under constant stress.

Difference between strain at austenite and strain at martensite denotes the actuation strain. Actuation strain decreased for HE Sample 1 with increased number of actuation cycles as shown in Figure 4.1-4. Actuation strain started with 1.6% value and then decreased to 0.89% in HE sample. Actuation strain values slightly decreased with increasing number of cycles due to dislocation formation leading to martensite pinning over the cycles. It has been already known that the dislocations, which are formed by phase transformation, pin the martensite-austenite boundary and hinder the boundary movement [30,56,57].

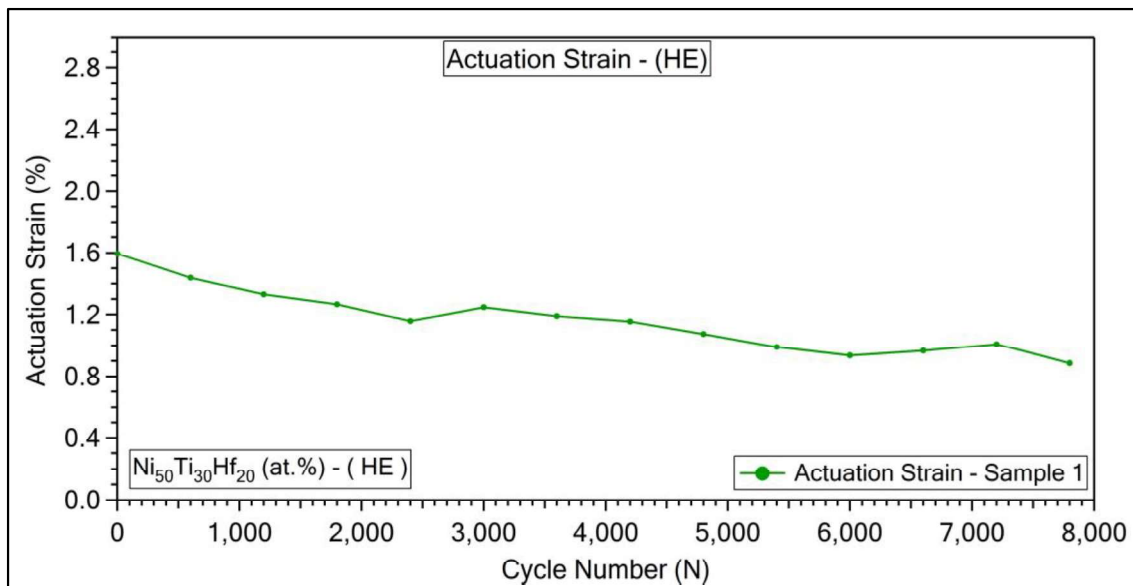


Figure 4.1-4. Actuation strain values that were determined from the actuation fatigue experiment of Ni₅₀Ti₃₀Hf₂₀ (at.%) HE Sample 1 under constant stress.

Accumulated irrecoverable strain values represent the strain values in which the change of shape could not be fully recovered upon cycles. Accumulated irrecoverable strain values of the HE Sample 1 with the number of cycles were given in Figure 4.1-5. There was an increasing trend in the values, but increasing rate decreased with the number of cycles due to strain hardening with the actuation cycles. As mentioned before, the number of dislocations increase at every heating-cooling cycles with the phase transformation under stress, thus the irrecoverable strain values increase as well. On the other hand, with the increase in the number of dislocations, the alloy undergoes strain hardening and therefore a decrease in the increasing rate of irrecoverable strain is observed. This is

actually similar to the strain hardening mechanism observed during plastic deformation of any metal alloy.

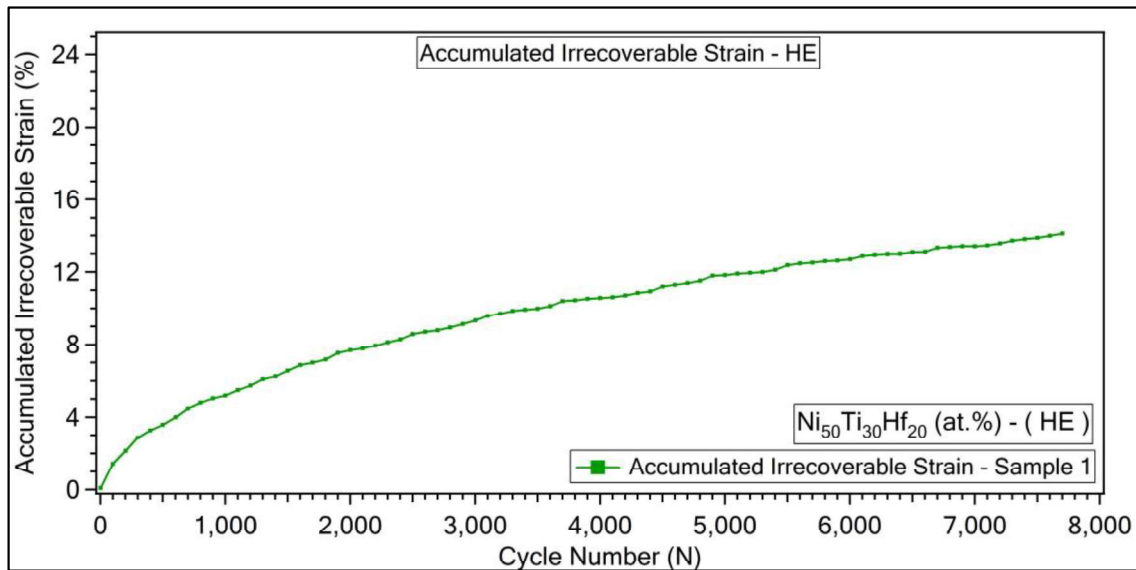


Figure 4.1-5. Accumulated irrecoverable strain values determined from actuation fatigue experiments of $\text{Ni}_{50}\text{Ti}_{30}\text{Hf}_{20}$ (at.%) HE Sample 1 under constant stress.

Thermal hysteresis values over the number of cycles were shown in Figure 4.1-6. There was a sharp decrease during the first 500 cycles and a slight increase in hysteresis values with the number of cycles. At the beginning, the randomly induced dislocations and the internal stress due to extrusion may help the phase transformation to take place without spending more energy, so the thermal hysteresis was determined to be decreasing. However, since dislocations and pinned martensite volumes increased later with the number of cycles more energy should be supplied for the progress of phase transformation by overcoming the pinning effect of dislocations.

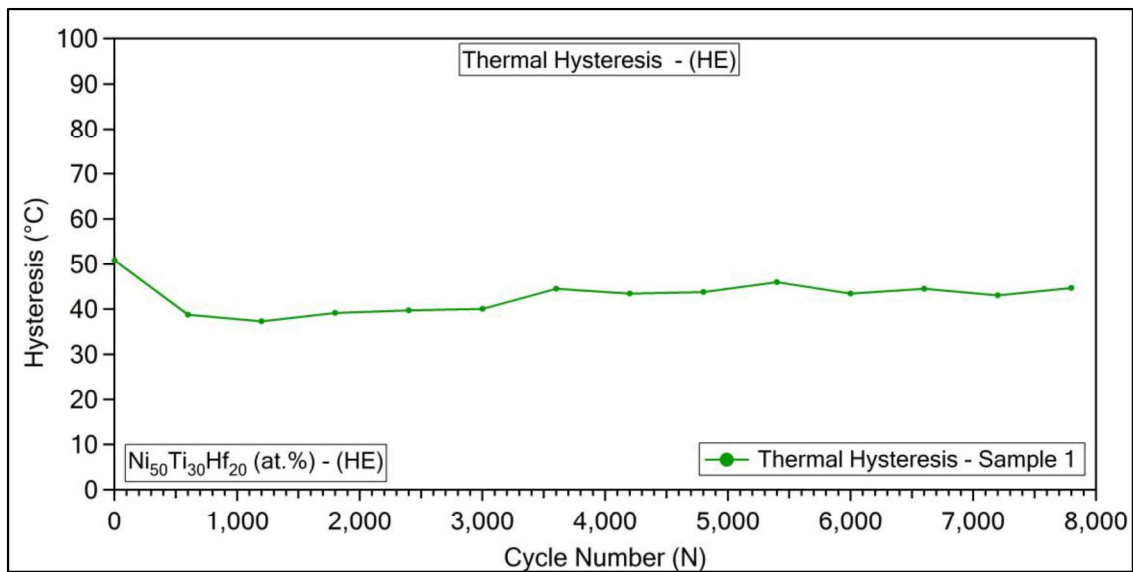


Figure 4.1-6. Thermal Hysteresis values determined from actuation fatigue experiments of Ni₅₀Ti₃₀Hf₂₀ (at.%) HE Sample 1.

During the actuation fatigue testing, Sample 1 (HE) was detached from the test set-up at each 600 intermittent cycles to investigate the crack initiations and crack growth. At each interval, optical micrographs were taken on different sections of the sample's surface, and crack length measurements were done. To investigate a wider surface area, the images from different sections were merged into one image at each intermittent cycle.

Optical images of the sample after different cycles were shown in Figure 4.1-7. From all collected optical images, major crack leading up to fracture were determined from the optical image that was taken after the last cycle, and the growth of that specific crack was followed. The crack lengths were measured at each intermittent cycle. The length of the major crack leading to fracture was shown with yellow color measurement boxes in Figure 4.1-7.

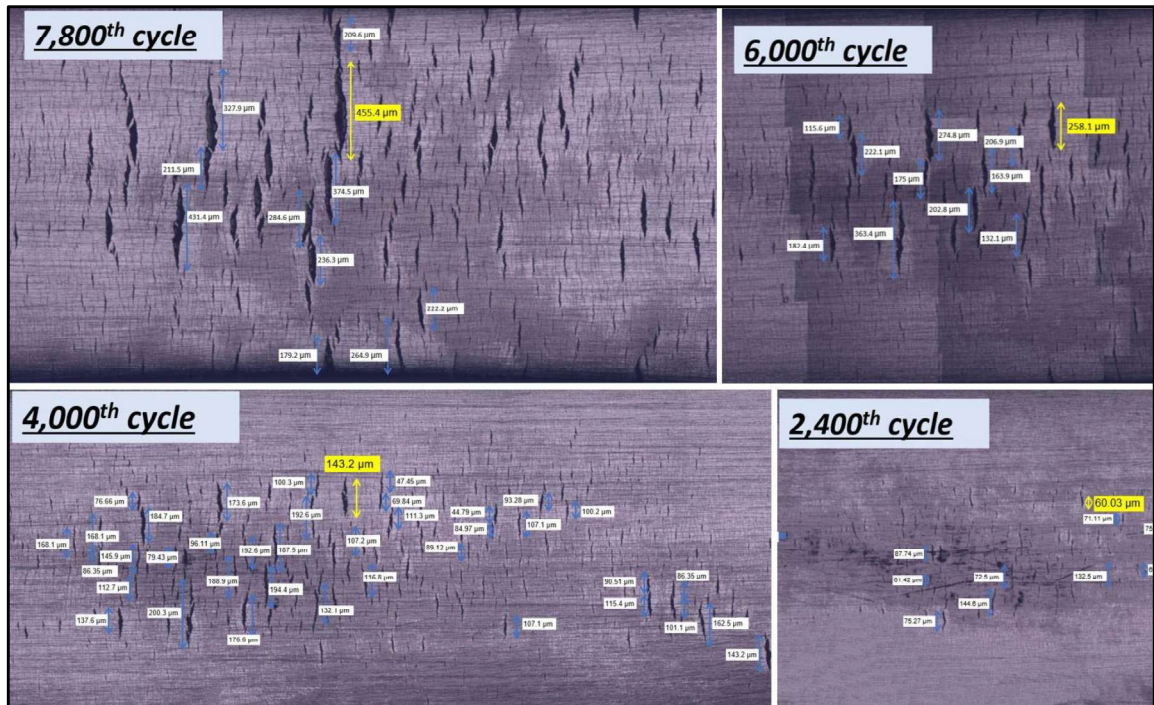


Figure 4.1-7. Optical Images of the crack formations in HE sample that were taken after intermittent cycles

The results of the crack length measurements at different cycles, best fit line and R-Squared (R^2) value which shows how well the best fit line fitted the data were shown in Figure 4.1-8. Crack growth rate of Sample 1 was found to be 0.054 $\mu\text{m}/\text{cycle}$. It is important to remind that, these measurements were taken by following the major crack that led to the failure of the sample. However, since a pre-notch was not initiated before the actuation cycles, crack distribution was different and crack growth rate was found to be relatively lower than that of the rates that were found from the test results of pre-notched samples in the following sections.

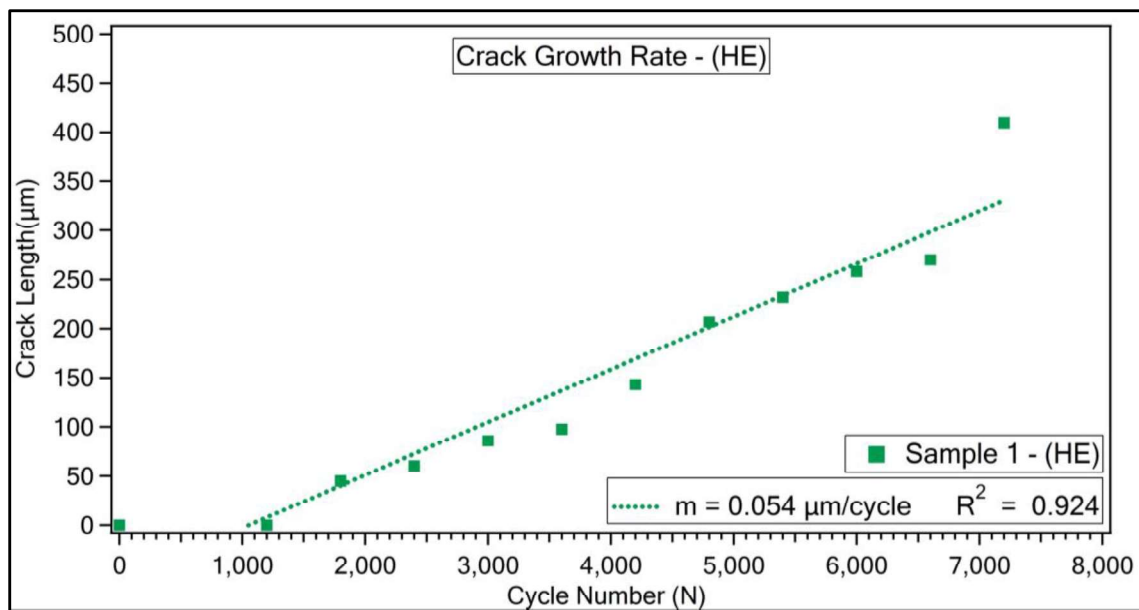


Figure 4.1-8. Crack length evolution with the number of cycles of HE sample from a leading crack to fracture

It was hard to find a crack initiation and very difficult to follow the growth of the major crack in a sample without a pre-notch form. Therefore, crack growth behavior was determined by running actuation fatigue tests on pre-notched samples in the following sections.

4.2. Actuation Fatigue Testing of HE-PN Samples

Actuation fatigue cycles were conducted on pre-notched hot extruded (HE-PN) Ni₅₀Ti₃₀Hf₂₀ (at.%) samples. 3 different samples (Sample 2, Sample 3, Sample 4) were tested by applying thermo-mechanical cycling with 15°C/s heating-cooling rate under constant load which corresponded to 200 MPa by hanging dead weights to sample.

Sample 2, Sample 3 and Sample 4 performed 2,702 , 4,200 and 2,200 cycles, respectively. Strain-Temperature curves from the actuation fatigue experiments of 3 HE-PN samples were shown in Figure 4.2-1 for the corresponding same number of cycles. Relatively similar trends were observed in Sample 2 and Sample 4, however the curves that were drawn for Sample 3 slightly shifted upwards with respect to the curves that were drawn

for other samples. The curves were shown with different colors, so the differences could be distinguished more easily.

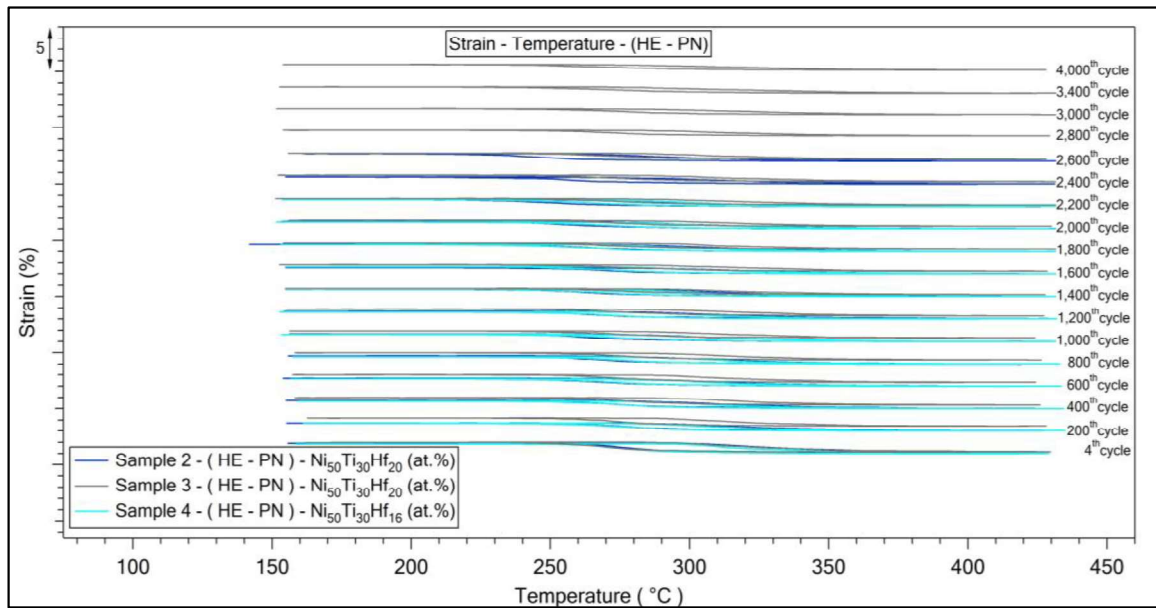


Figure 4.2-1. Strain-Temperature curves from the actuation fatigue experiments of 3 HE-PN $\text{Ni}_{50}\text{Ti}_{30}\text{Hf}_{20}$ (at.%) samples [67].

M_s and A_f temperature values were indicated for the sake of simplicity in the graphs for all experiments. M_s and A_f temperatures that were determined from the Strain-Temperature curves for all samples showed nearly similar trends with the number of cycles as can be seen in Figure 4.2-2. While M_s temperature values were around 300°C , A_f values were found to be around 350°C .

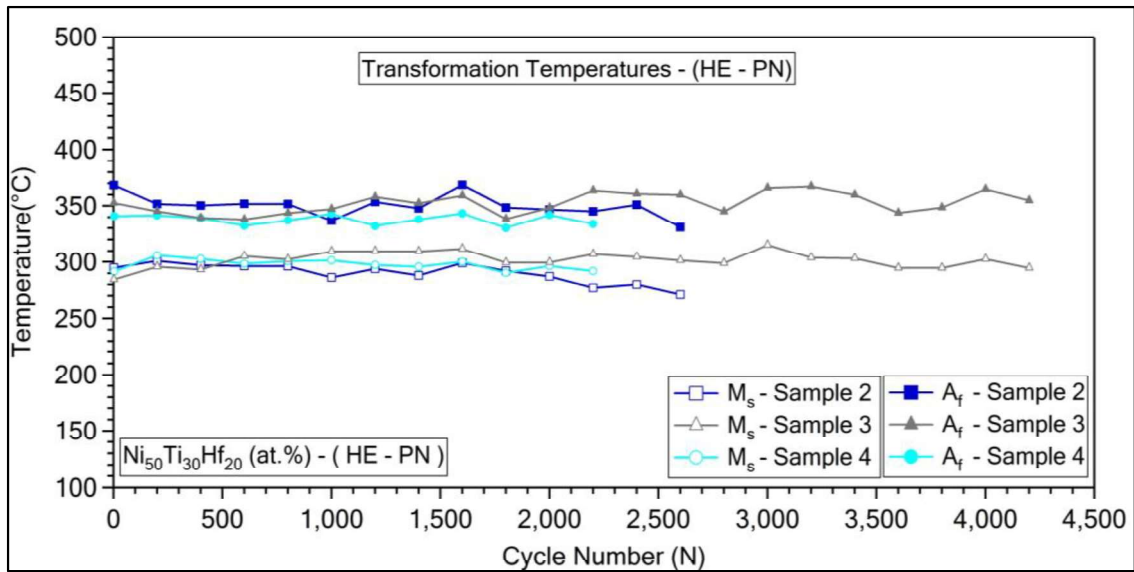


Figure 4.2-2. TT evolutions determined from actuation fatigue experiment of Ni₅₀Ti₃₀Hf₂₀ (at.%) HE-PN sample.

Actuation strain values of HE-PN samples demonstrated almost similar decreasing trend, however, the values of Sample 3 diverged from the values of the other two samples starting from 1,200th cycle (Figure 4.2-3).

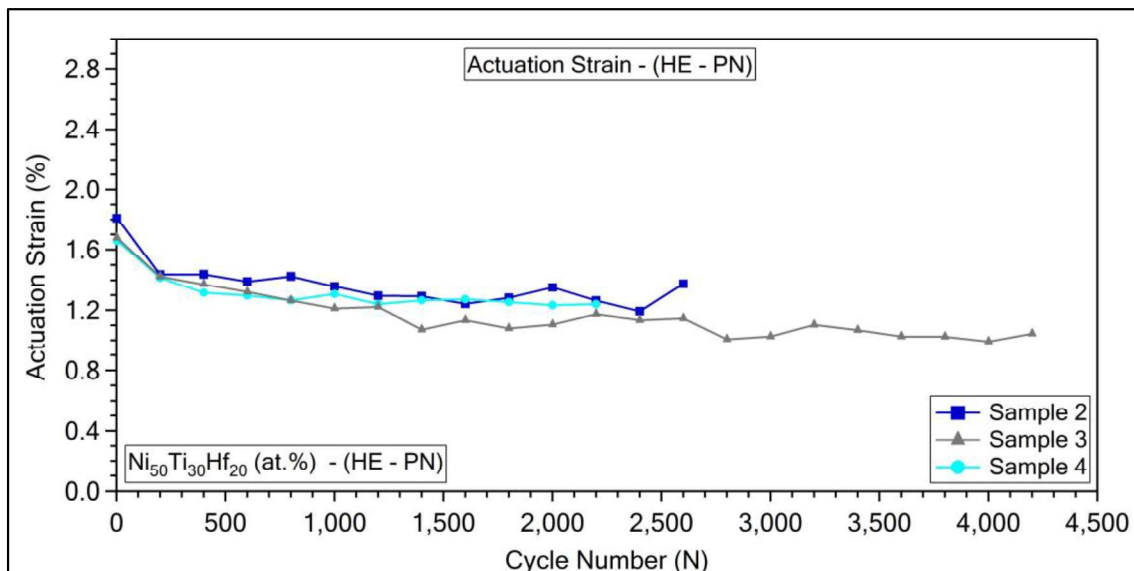


Figure 4.2-3. Actuation strain values determined from actuation fatigue experiments of 3 HE-PN Ni₅₀Ti₃₀Hf₂₀ (at.%) samples [67].

Accumulated irrecoverable strain values of HE-PN samples increased with the number of cycles, however increasing rate of the accumulated irrecoverable strain of these three samples varied during the tests as shown in Figure 4.2-4. All samples exhibited similar increasing trend at the beginning of the actuation cycles, however the values diverged from each other later.

Accumulated irrecoverable strain values did not saturate and kept increasing with the cycles. This behavior might be due to the pre-notch, crack initiations and growths of the cracks from pre-notch or the other cracks, which were formed during cycling. Additionally, the increasing rate of the accumulated irrecoverable strain values of these three samples was found to be higher than that of Sample 1, which is the sample without pre-notch. For instance, Sample 2 and Sample 3 showed 12% of accumulated irrecoverable strain value at around 2,300th and 4,200th cycles, while the sample with no pre-notch showed the same irrecoverable strain value at around 5,700th cycle.

A jump was observed on the accumulated irrecoverable vs cycle number curve of Sample 2 at the end of actuation cycles and this is due to the peeling of the black paint from the surface of the sample that was used to accurately measure the temperature data. The increase of surface crack formations towards the last cycles of the actuation fatigue experiments could also lead the black paint to be peeled off from the surface. Thus, measuring the temperature accurately became difficult and the samples could be heated to higher temperatures than that of the set UCT value (440°C). If the sample was mistakenly heated well above the UCT due to the black paint peeled off the surface, the strength of the alloy would decrease and the crack propagation and dislocation formation rate would increase. This might be the reason of the jump in the accumulated irrecoverable strain value.

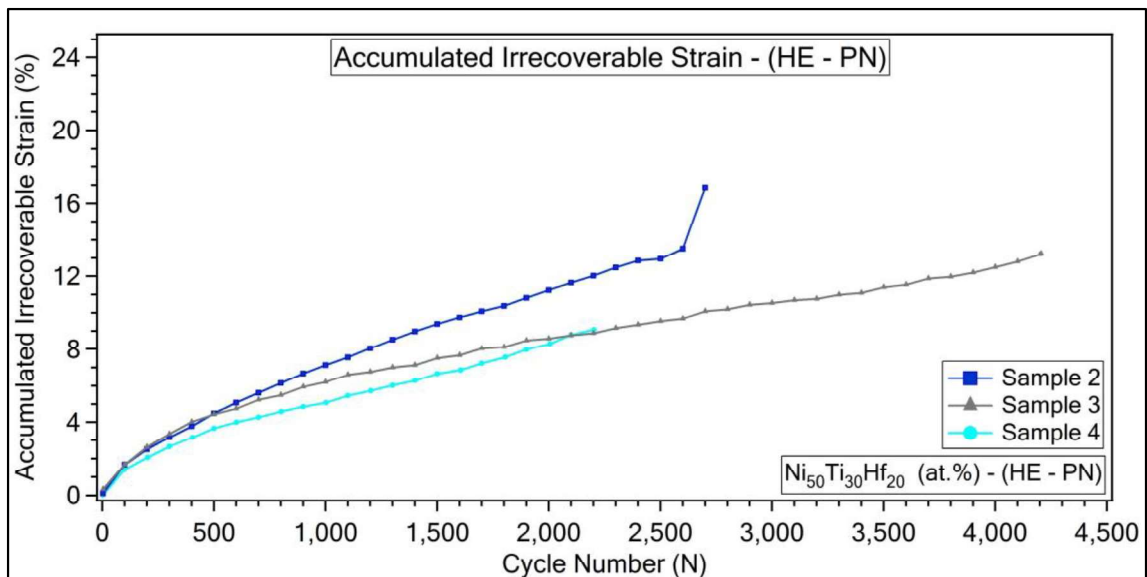


Figure 4.2-4. Accumulated irrecoverable strain values determined from actuation fatigue experiments of 3 HE-PN $\text{Ni}_{50}\text{Ti}_{30}\text{Hf}_{20}$ (at.%) samples under constant stress [67].

Thermal hysteresis values of all HE-PN samples were determined from the actuation fatigue cycle curves and shown in Figure 4.2-5. Similar decreasing and increasing trends were observed for all HE-PN samples. However, thermal hysteresis values were not so close to each other at these samples (Figure 4.2-5).

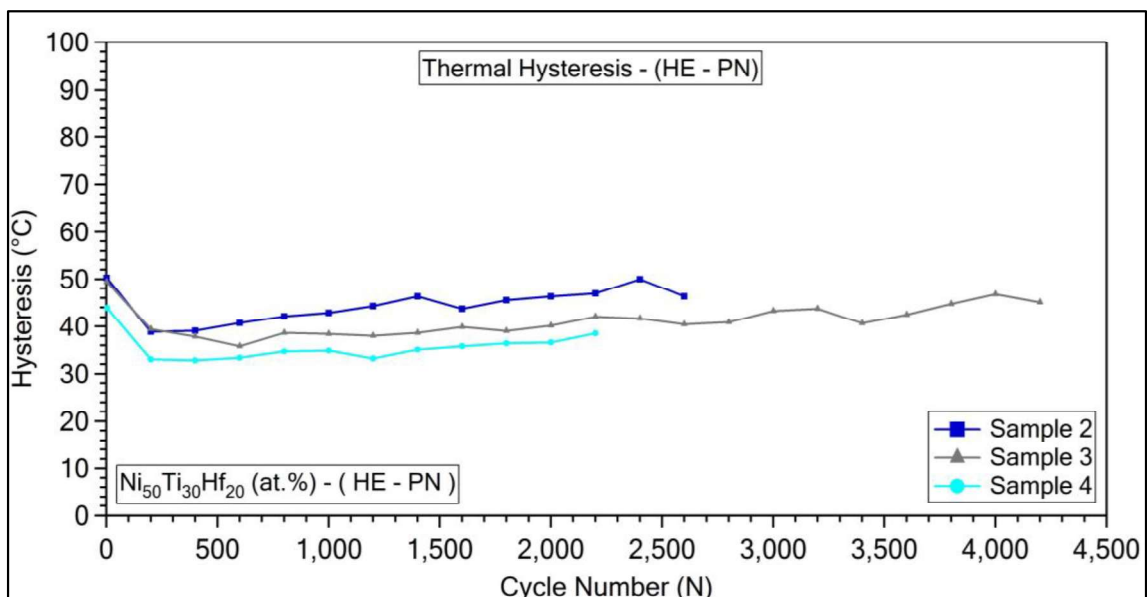


Figure 4.2-5. Thermal Hysteresis values determined from actuation fatigue experiments of 3 HE-PN $\text{Ni}_{50}\text{Ti}_{30}\text{Hf}_{20}$ (at.%) samples.

During the heating-cooling cycling of HE-PN samples, to take a better look on the formation and propagation behavior of cracks with the number of actuation fatigue cycles, optical micrographs were taken after every 200 actuation cycles. Optical micrographs were recorded at different magnification levels to investigate the formations and measurements.

Location of optical micrographs from where images were taken for HE-PN samples were represented in Figure 4.2-6. Wire EDM created pre-notch geometry and area around the pre-notch were demonstrated in the figure. Optical micrographs of the area around the crack before the test start and after the previous intermittent cycle before the fracture were also given in the figure.

Initial crack length of the samples in figures was defined as the depth of the pre-notches that was mentioned previously in experimental procedure section and presented with the letter 'a', which was around 0.3 mm (300 μm). However, measured pre-notch length in lateral axis and load axis before starting the test could be different in samples due to the precision of EDM cutting method. For instance, the dimensions of the pre-notch of Sample 2 were 280 μm and 422 μm before the test was started.

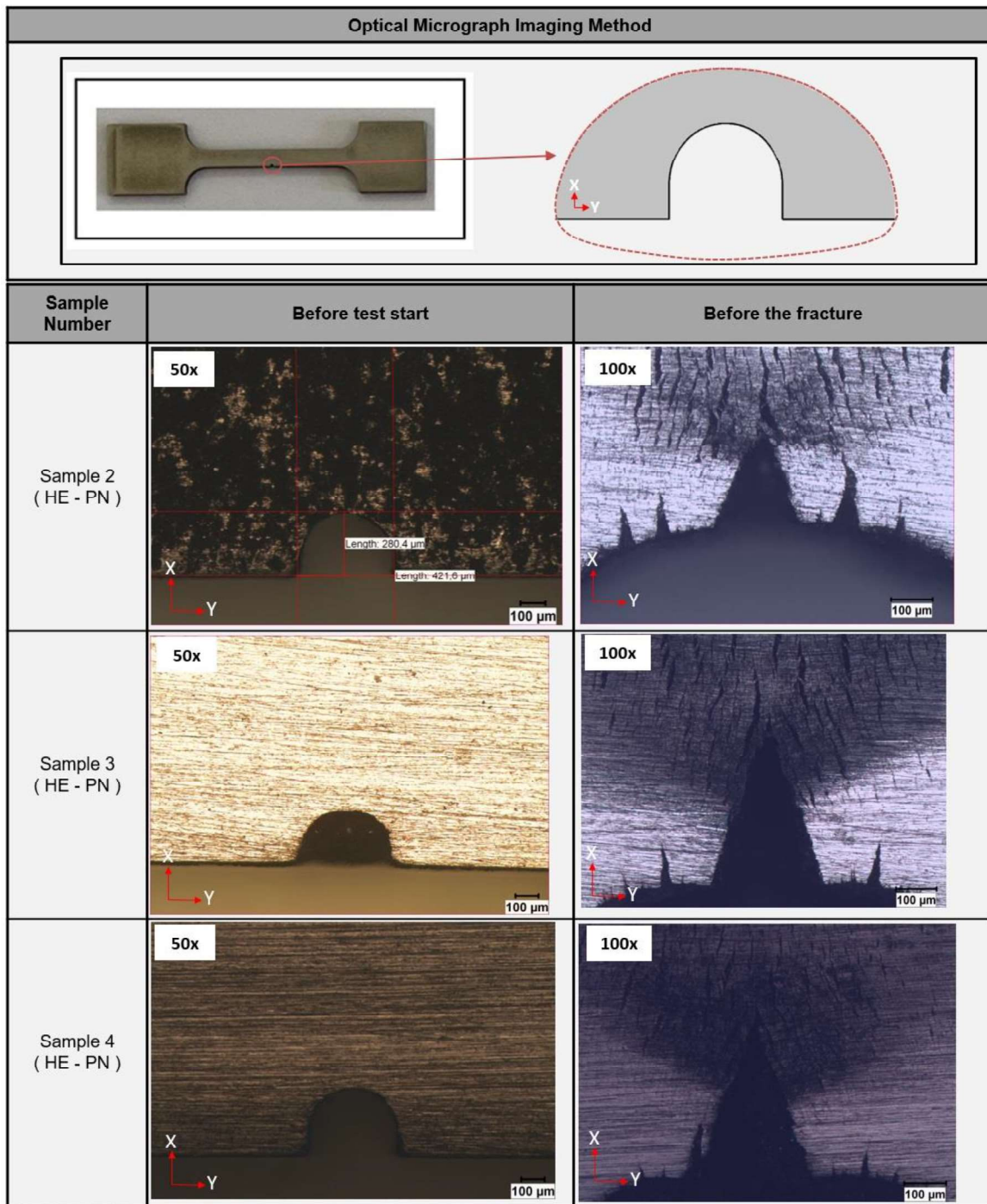


Figure 4.2-6. The region showing where the crack images were taken and the crack images of the HE-PN samples before the actuation fatigue test and just before the fracture [67].

Optical micrographs that were taken after each 200 intermittent cycles were shown and presented for 1,200th, 1,400th, 1,600th, 1,800th and 2,000th cycles in Figure 4.2-7.

A distinctive major crack leading to fracture in all HE-PN samples can be seen in the figure.

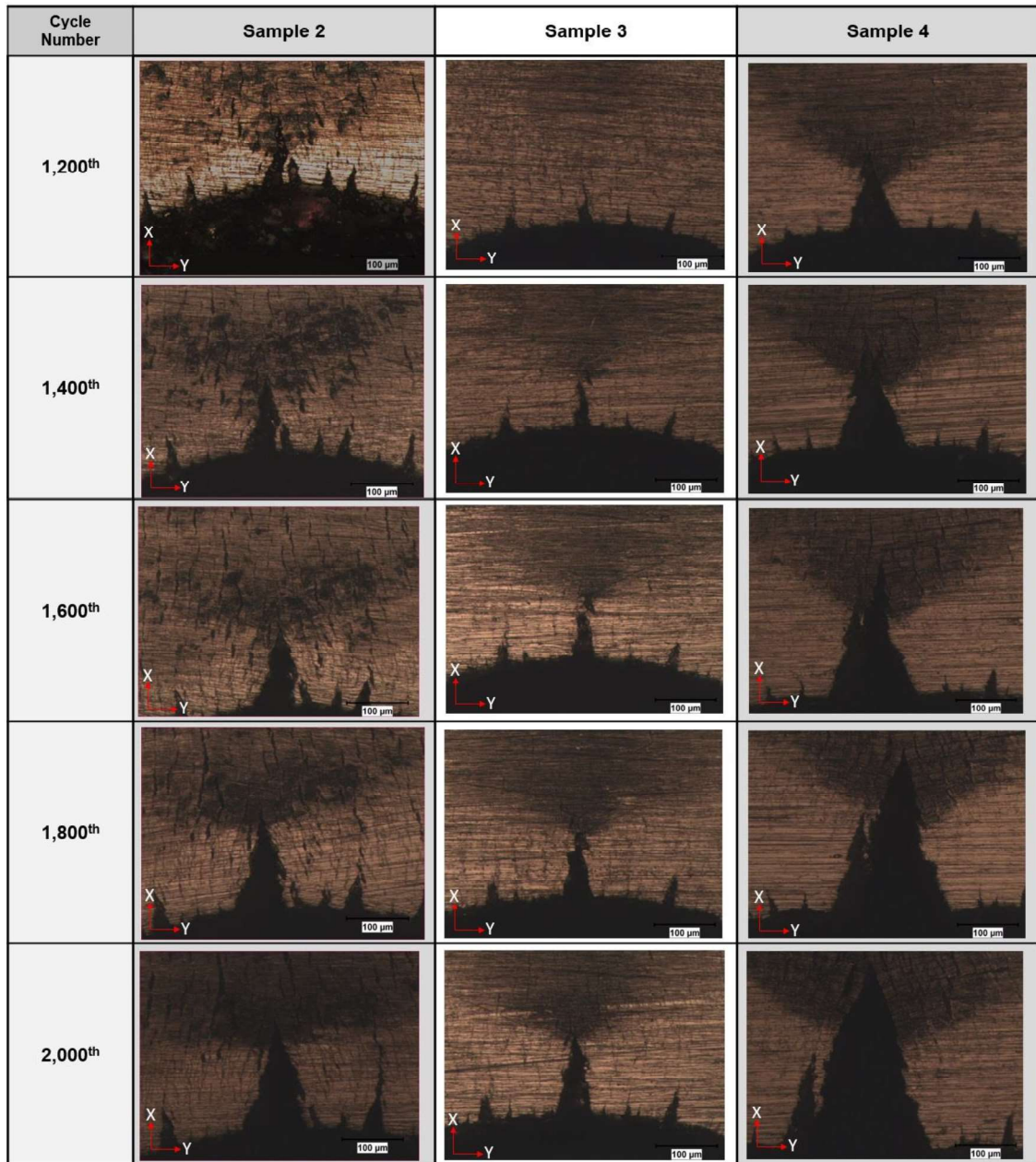


Figure 4.2-7. Pre-notch, major crack and side crack optical micrographs of HE-PN samples after 1,200th, 1,400th , 1,600th , 1,800th and 2,000th cycles of actuation cycling [67]

The crack size evolution was analyzed by measuring the length of major crack, which propagated with the number of actuation cycles. The total length data points of the major crack at different intermittent cycles were shown on the graph, the data points were

connected and best fit lines were drawn passing from these data points (Figure 4.2-8). Then, slope of these lines defining the crack growth rate ($\mu\text{m}/\text{cycle}$) of the samples for actuation cycles were calculated and presented with the letter "m". R-Squared values of these 3 best fit lines were also calculated and given in the figure. It is important to mention that the graph of crack growth rate with respect to stress intensity range (ΔK) could not be drawn in the study since there is a different mechanism in actuation cycling of SMAs. Crack growth occurs in these materials due to thermally triggered phase transformation under constant load in actuation fatigue testing instead of alternating stress magnitude application in conventional fatigue experimentation of metal alloys.

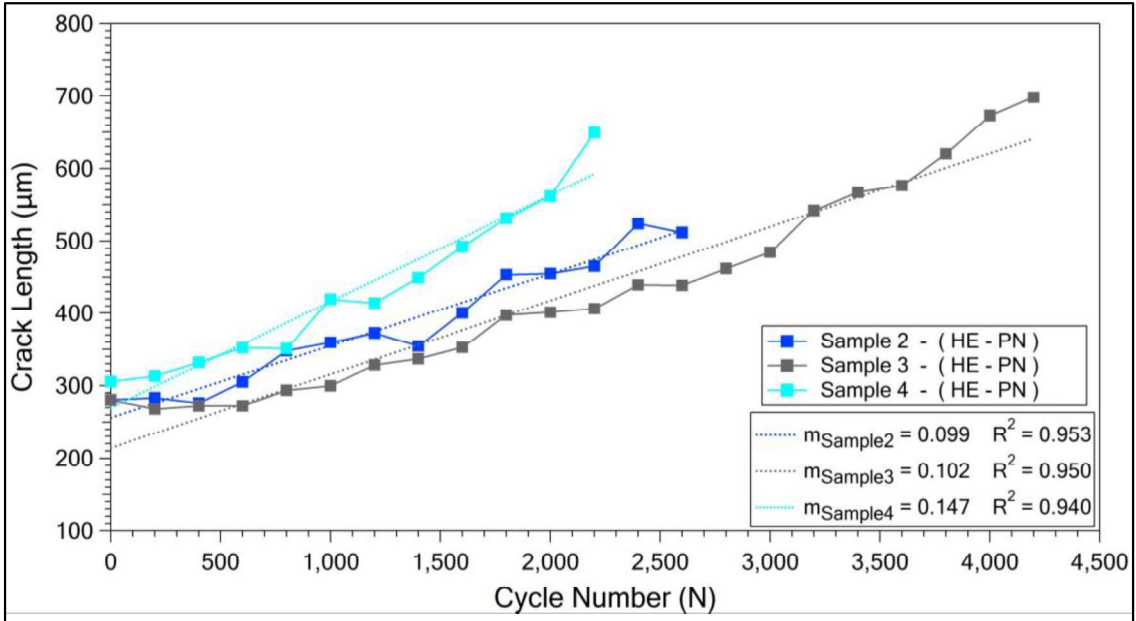


Figure 4.2-8. Evolution of crack lengths with the number of cycles in actuation fatigue cycling of HE-PN samples [67]

Crack growth rates of Sample 2, Sample 3 and Sample 4 were tabulated in Table 4.2-1. Although Sample 2 and Sample 3 showed relatively closer crack growth rates, the significant increase in the crack length (the growth of crack) started at a different cycle of the actuation fatigue experiment that was conducted on Sample 3. While crack growth at Sample 2 and Sample 4 was seen starting after 200th cycle, crack length increase was seen after 800th cycle in Sample 3. Also, actuation fatigue lifetime of Sample 3 was completely different as well as the propagation of an initiated crack growth started later compared to other samples.

Table 4.2-1. Crack growth rate values (“m”) of HE-PN samples and crack length change trend [67]

“m” Values	Sample 2	Sample 3	Sample 4
Crack Growth Rate ($\mu\text{m}/\text{cycle}$)	0.099	0.102	0.147

SIF values were determined by using the equation of Tada et al. [75], which was defined and explained in the experimental procedure section. Geometric factor and crack length dimensions were used in the formula to define SIF values and represented plot was given in Figure 4.2-9. SIF values were increased by the increase in crack length with the number of cycles.

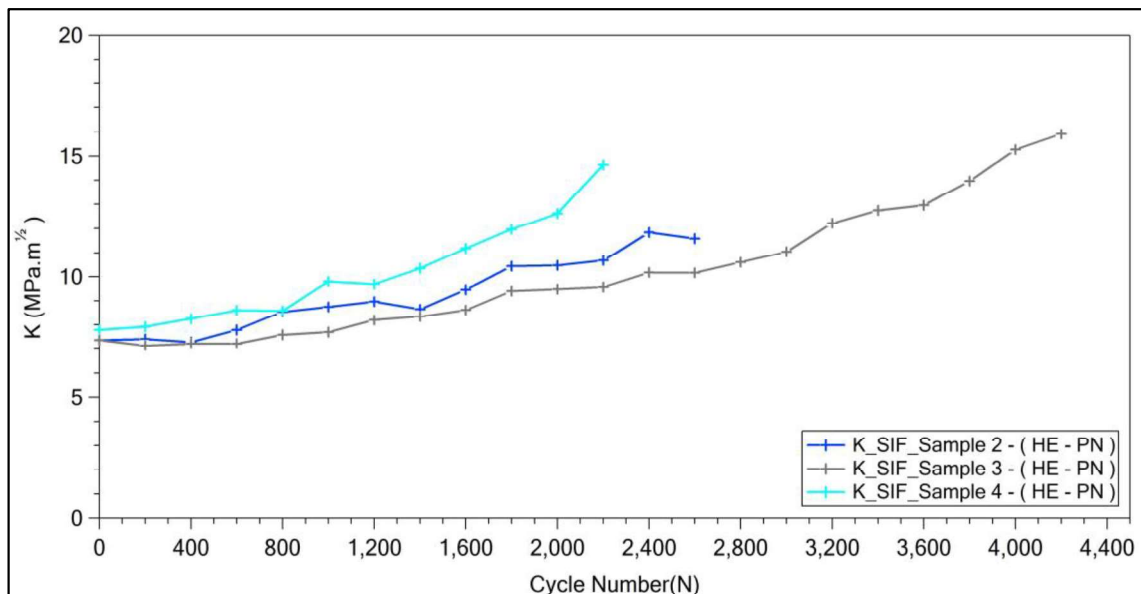


Figure 4.2-9. SIF values calculated for HE-PN samples by the crack lengths at intermittent cycles [67]

Fracture surface of the Sample 4 was investigated using SEM to reveal the fracture modes of the sample. Fracture morphology of the Sample 4 after actuation fatigue cycling exhibited a combination of both intergranular and transgranular fracture morphology. However, more intergranular formations had been seen on the fracture surfaces in addition to a couple of dimples on the surface.

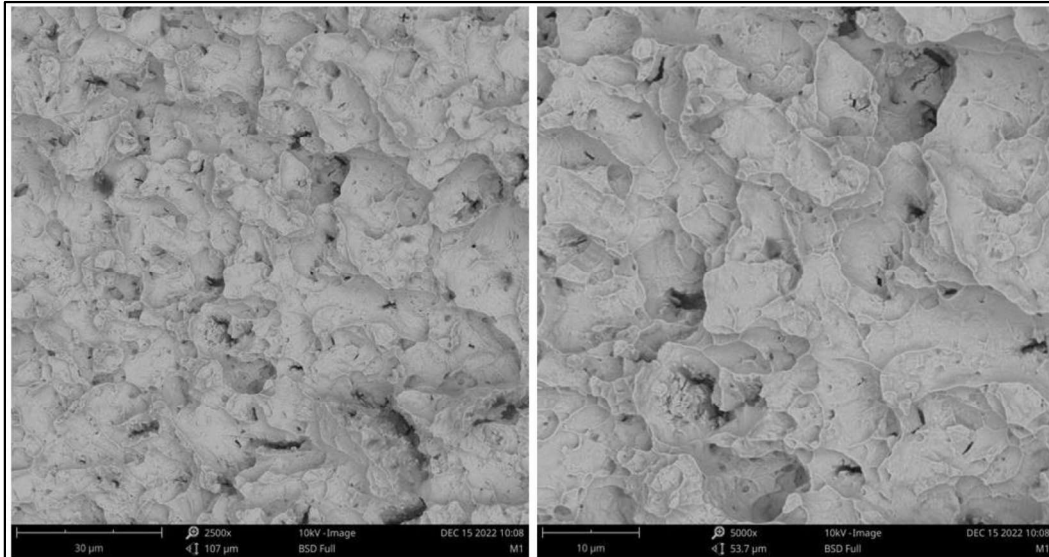


Figure 4.2-10. SEM images from fracture surface of Sample 4 after actuation fatigue experiment

Briefly, HE-PN samples showed diverse shape memory properties and crack growth behavior compared to each other. Since there can be deformation variation and induced stresses due to the hot extrusion process that was previously shown by our research group annealing heat treatment was applied to virgin samples from the same batch as suggested by Akin et al. and these samples were coded as HE-PN-AN [22].

4.3. Actuation Fatigue Testing of HE-PN-AN Samples

TTs of annealed Ni₅₀Ti₃₀Hf₂₀ (at.%) alloys were obtained and previously reported by our lab group for the same batch of alloy from DSC experiments. The results are shown in Table 4.3-1.

Table 4.3-1. Stress-free TTs of annealed Ni₅₀Ti₃₀Hf₂₀ (at.%) alloys [22]

Stress-free TTs of annealed Ni₅₀Ti₃₀Hf₂₀ (at.%)				
	A _f	A _s	M _s	M _f
Temperatures (°C)	328	281	282	229

Actuation fatigue experiments were performed on pre-notched and annealed samples by running cooling-heating cycles under constant load which corresponded to 200 MPa stress condition via considering the initial cross-section area of the sample. Samples enumerated with 5 and 6 were tested by applying thermal cycles with 15°C/s heating-cooling rate. UCT and LCT temperatures were set to 440°C and 150°C, respectively as in the case of previous actuation fatigue tests.

Actuation Fatigue lifetimes of Sample 5 and Sample 6 were found to be 2,683 and 2,351 cycles, respectively. Strain-Temperature curves, which were previously presented for the same cycles of annealed samples, obtained from the activation fatigue test of the HE-PN-AN sample, are shown in Figure 4.3-1. Strain-Temperature curves that were obtained at each 200th cycles were shown together for both of the annealed samples. Both samples showed almost the same strain-temperature curves at the same actuation cycles.

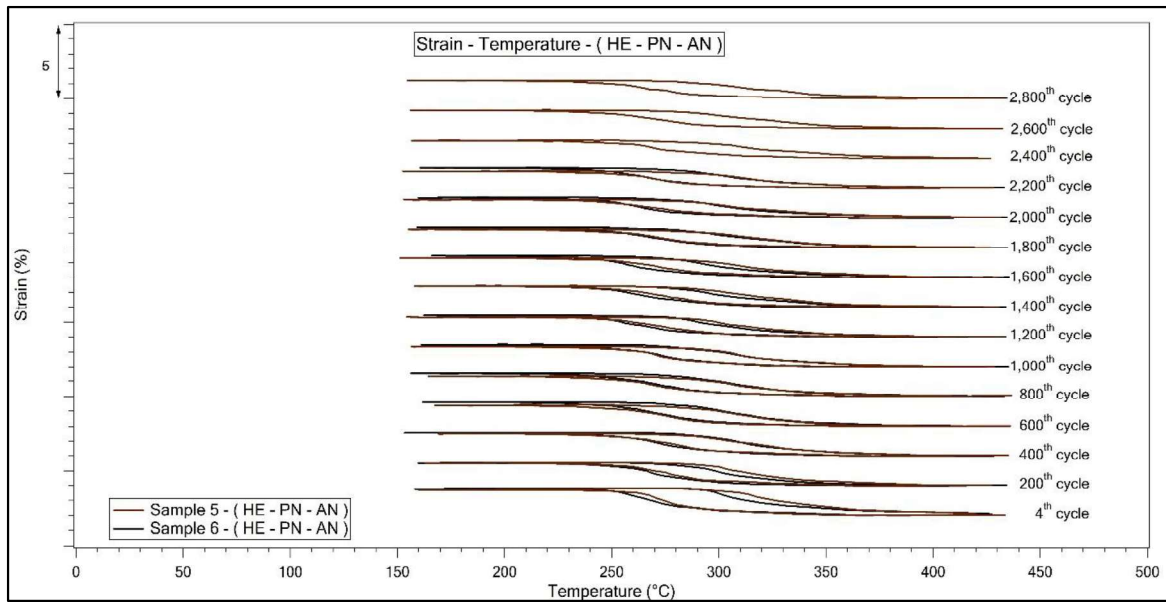


Figure 4.3-1. Strain-Temperature curves from the actuation fatigue experiments of $\text{Ni}_{50}\text{Ti}_{30}\text{Hf}_{20}$ (at.%) HE-PN-AN samples [67].

Annealed samples (HE-PN-AN) with pre-notches showed pretty similar TTs throughout the cycles as shown in Figure 4.3-2. M_s temperatures were around 290°C and A_f temperatures of Sample 5 were in the range of 337°C to 358°C and of Sample 6 were in the range of 326°C to 343°C .

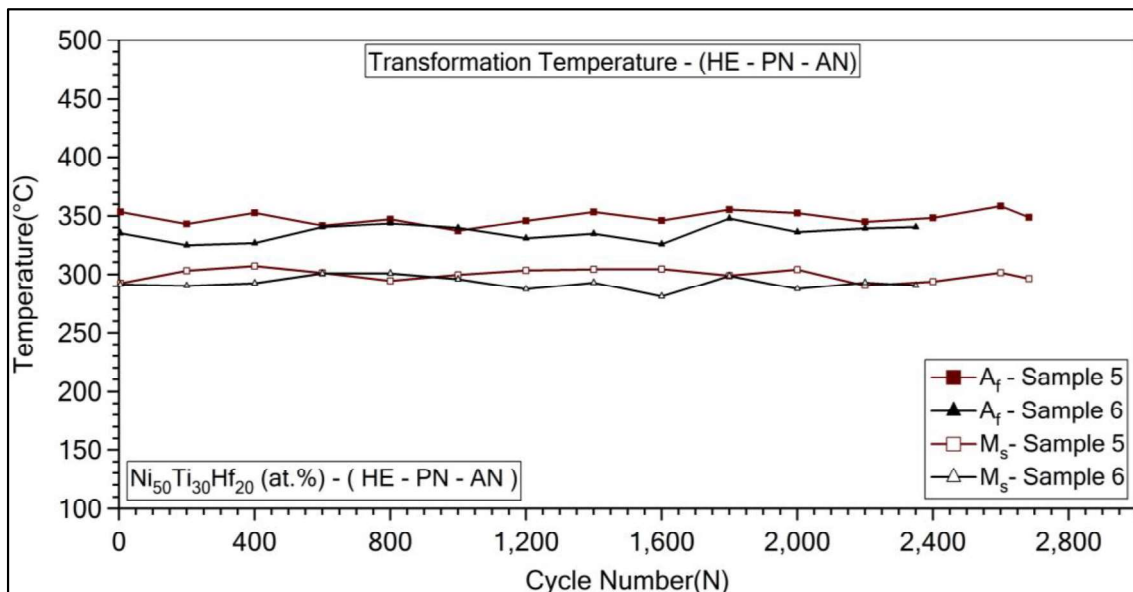


Figure 4.3-2. Evolution of TTs, which were determined from Actuation Fatigue experiment conducted on HE-PN-AN $\text{Ni}_{50}\text{Ti}_{30}\text{Hf}_{20}$ (at.%) samples.

Actuation strain values were slightly decreased as it was shown in other studies the literature with the number of cycles due to the plastic strain accumulation and residual martensite plates that are pinned by the dislocations with the actuation cycles [29,76]. The actuation strain evolution with the number of cycles was demonstrated in Figure 4.3-3. The work output could be calculated by multiplying the applied stress with actuation strain. Work output value also decreased with the actuation strain decrease. However, since the actuation strain values were almost the same at all cycles for annealed samples, the work output values were approximately the same at all cycles.

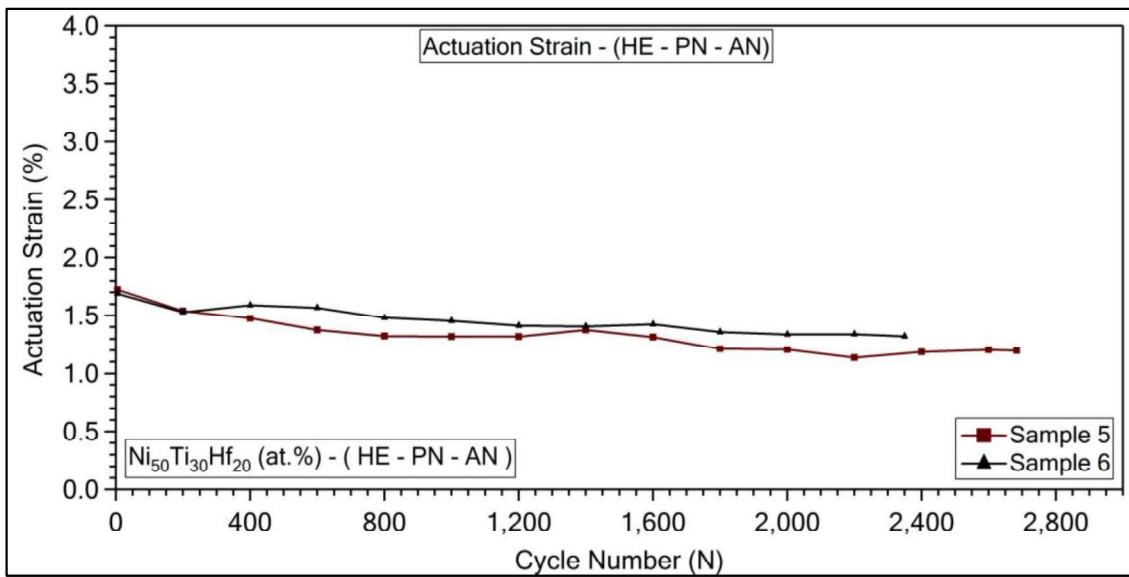


Figure 4.3-3. Actuation strain values determined from Actuation Fatigue experiment conducted on HE-PN-AN Ni₅₀Ti₃₀Hf₂₀ (at.%) samples [67].

Accumulated irrecoverable strain values increased with the number of cycles in HE-PN-AN samples, and both samples resulted almost similar accumulated irrecoverable strain values as can be seen in Figure 4.3-4. The similarity in the irrecoverable strain values of HE-PN-AN samples can be attributed to the stress relief and homogenized extruded microstructure via annealing as explained in the previous paragraphs.

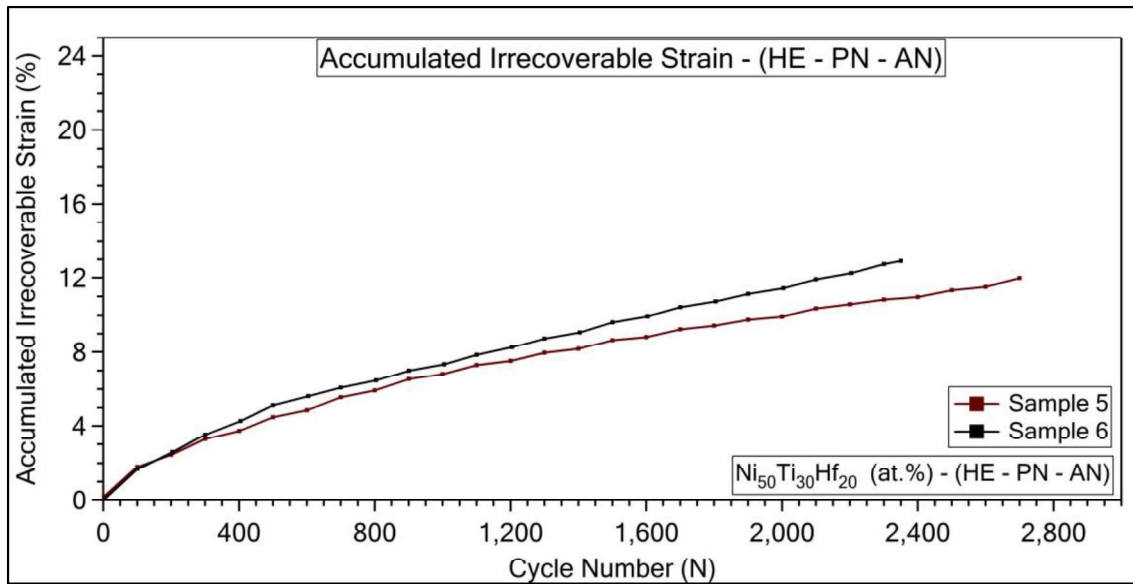


Figure 4.3-4. Accumulated irrecoverable strain values determined from Actuation Fatigue experiment conducted on HE-PN-AN $\text{Ni}_{50}\text{Ti}_{30}\text{Hf}_{20}$ (at.%) samples [67].

Thermal hysteresis values of HE-PN-AN were almost in similar trends and very close to each other as shown in Figure 4.3-5. A sharp decrease through the first 200 cycles was observed and then an increase with a very low rate in the thermal hysteresis values was determined through the rest of the experiments. The initial decrease can be attributed to the annealing and the increase can be attributed to the increase in dislocation density with the number of cycles. Since the dislocations are able to pin the martensite-austenite and increase the resistance to phase transformation higher energy should be supplied to the alloys to overcome this energy.

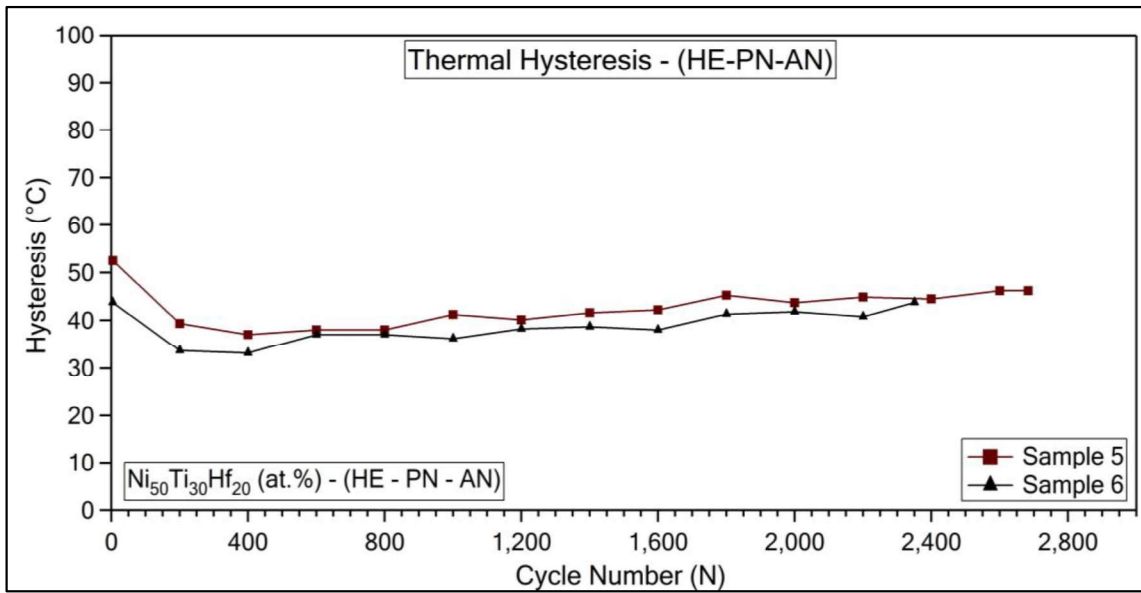


Figure 4.3-5. Thermal hysteresis values determined from actuation fatigue experiments of $\text{Ni}_{50}\text{Ti}_{30}\text{Hf}_{20}$ (at.%) HE-PN-AN sample.

Crack formations and length of cracks were investigated by using optical micrographs taken after every 200 actuation cycles that were run on annealed samples (HE-PN-AN). Crack images of HE-PN-AN samples before the actuation fatigue experiments and just before the fracture could be seen in Figure 4.3-6.

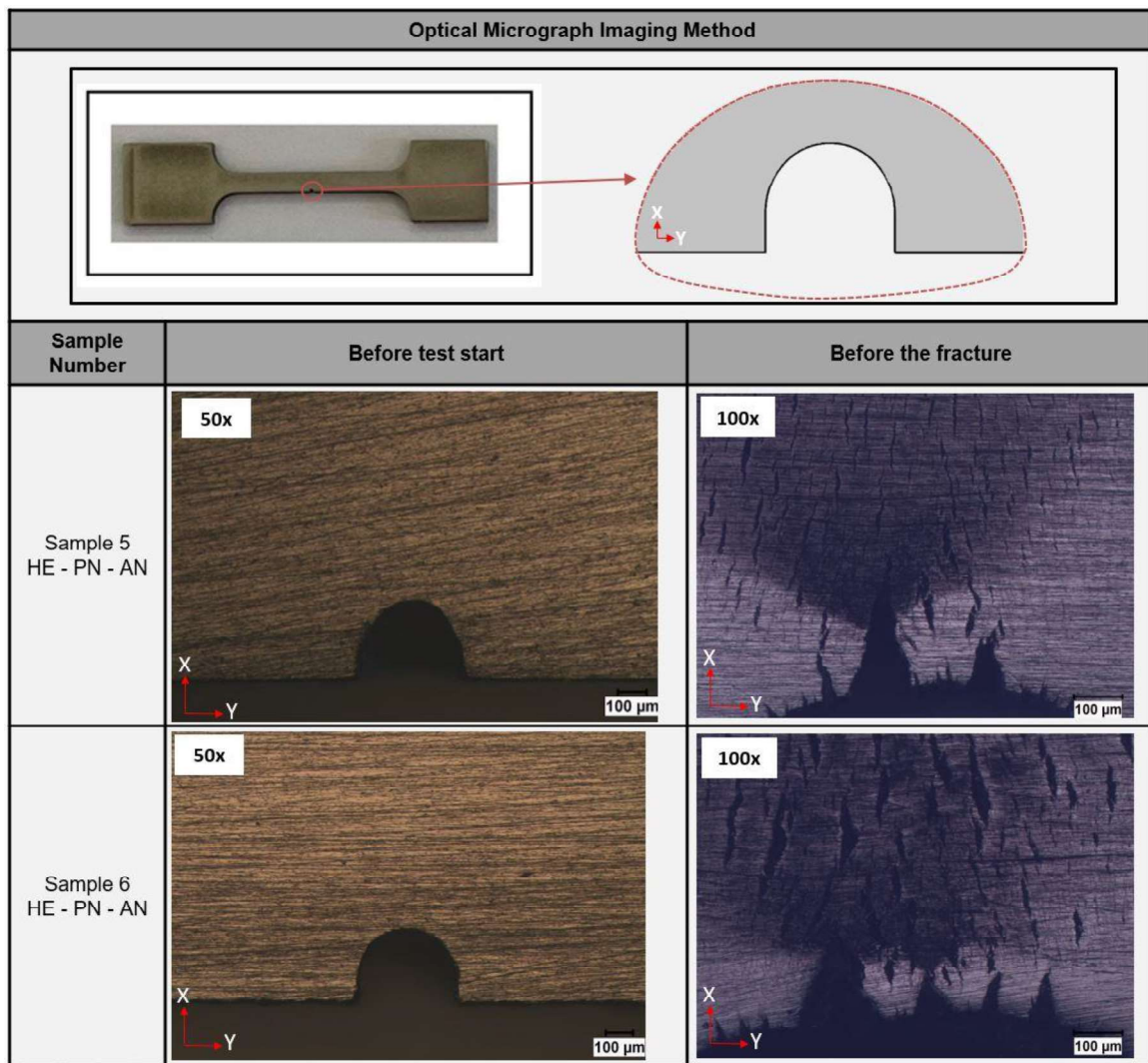


Figure 4.3-6. The region showing where the crack images were taken and the crack images of the HE-PN-AN samples before the actuation fatigue test and just before the fracture [67].

Optical micrographs showing the pre-notch area were presented for 1,200th, 1,400th, 1,600th, 1,800th and 2,000th cycles in Figure 4.3-7.

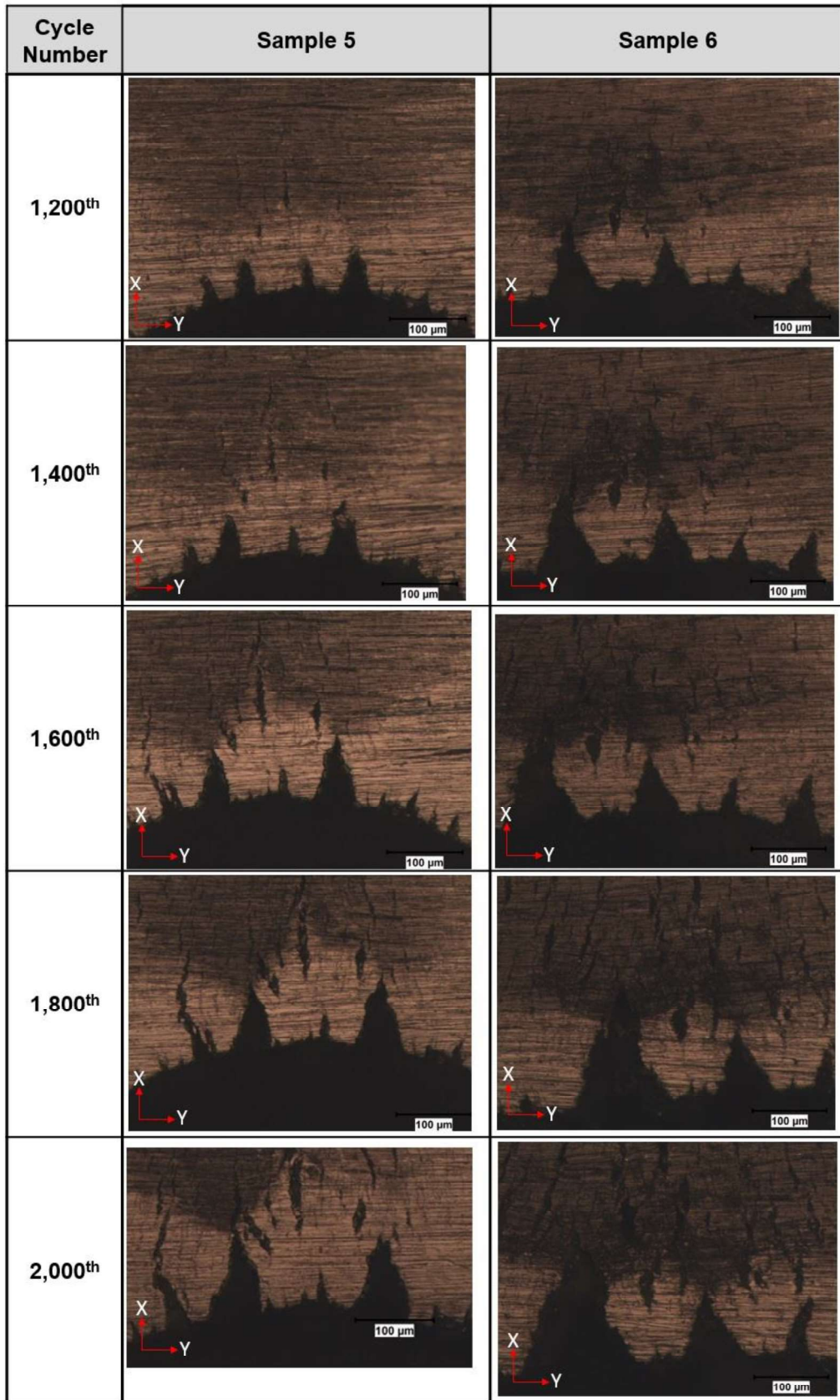


Figure 4.3-7. Pre-notch, major crack and side crack optical micrographs of HE-PN-AN samples after 1,200th, 1,400th, 1,600th, 1,800th and 2,000th cycles of actuation cycling [67]

The crack length size evolutions over the actuation cycles of HE-PN-AN samples were given in Figure 4.3-8. Best fit lines passing from the data points and their R-Squared values were also presented in the figure. Major crack data leading to fracture at after every 200 intermittent cycles and best fit lines of these data showed almost similar crack growth rate trend with increasing number of actuation fatigue cycles as can be seen in Figure 4.3-8.

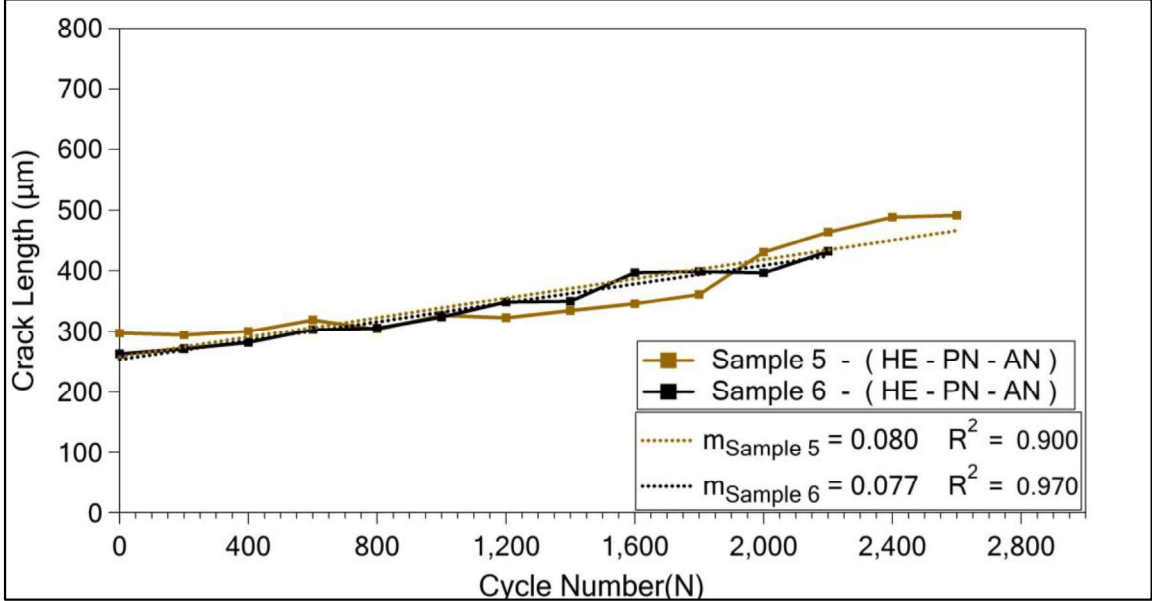


Figure 4.3-8. Evolution of crack lengths with the number of cycles in actuation fatigue cycling of HE-PN-AN samples [67]

Due to the simultaneously joining minor cracks after 200 cycles, the total crack length of HE-PN-AN Sample 5 suddenly increased between the 1,800th and 2,000th actuation cycles as shown in Figure 4.3-9. This increase also led to sudden increase of SIF value of Sample 5 after 1,800th cycle, which could be seen in Figure 4.3-10.

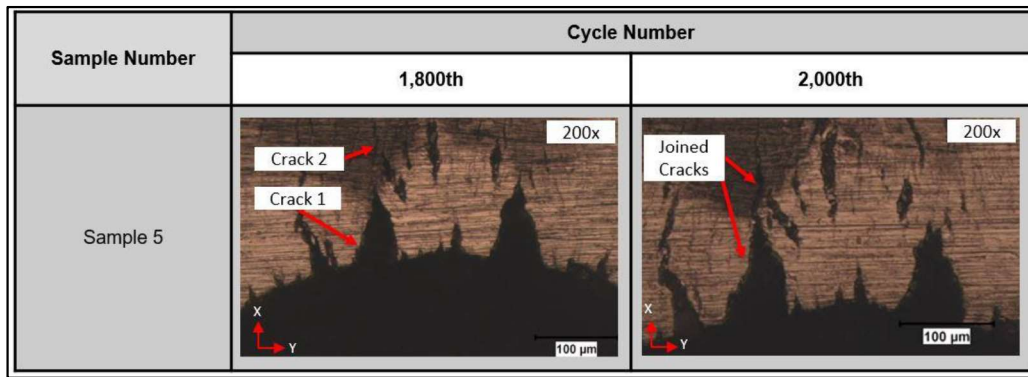


Figure 4.3-9. Pre-notch, major crack and side crack optical micrographs of Sample 5 after 1,800th, 2,000th cycles of actuation cycling [67]

Crack growth values of Sample 5 and Sample 6 were tabulated in Table 4.3-2. Almost similar crack growth rates were determined.

Table 4.3-2. Crack growth rate values (“m”) of HE-PN-AN samples and crack length change trend [67]

“m” Values	Sample 5	Sample 6
Crack Growth Rate (μm/cycle)	0.080	0.077

Plots showing SIF values determined by using the equation of Tada et al. [75] was shown in Figure 4.3-10 for annealed samples. A lower and similar increasing trend in SIF values after actuation cycles were seen until 1,800th cycle for annealed samples. Until distinctive increase, SIF values were mitigated due to the annealing process via rearranged dislocations and relieved stresses that were induced from hot extrusion process.

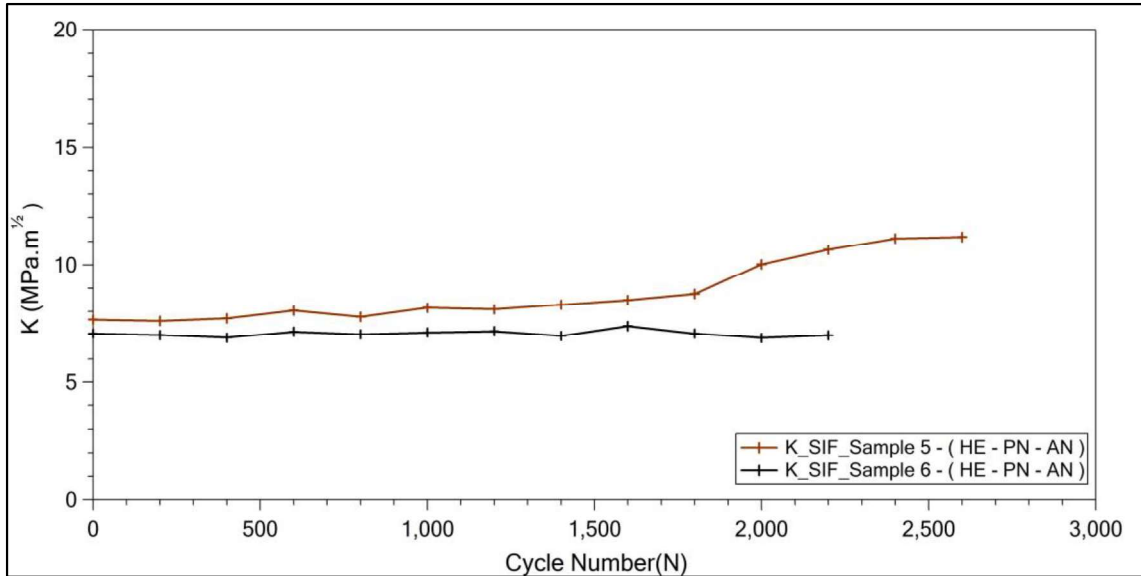


Figure 4.3-10. SIF values calculated for HE-PN-AN samples by the crack lengths at intermittent cycles [67]

Fracture surface of failed HE-PN-AN Sample 6 was shown in Figure 4.3-11. Fracture morphology of the Sample 6 after actuation fatigue cycling showed both transgranular and intergranular fracture surfaces as demonstrated in Figure 4.3-11. Intergranular fracture mode found to be dominant on the fracture surfaces. Additionally, few smaller dimples were also found on the surface.

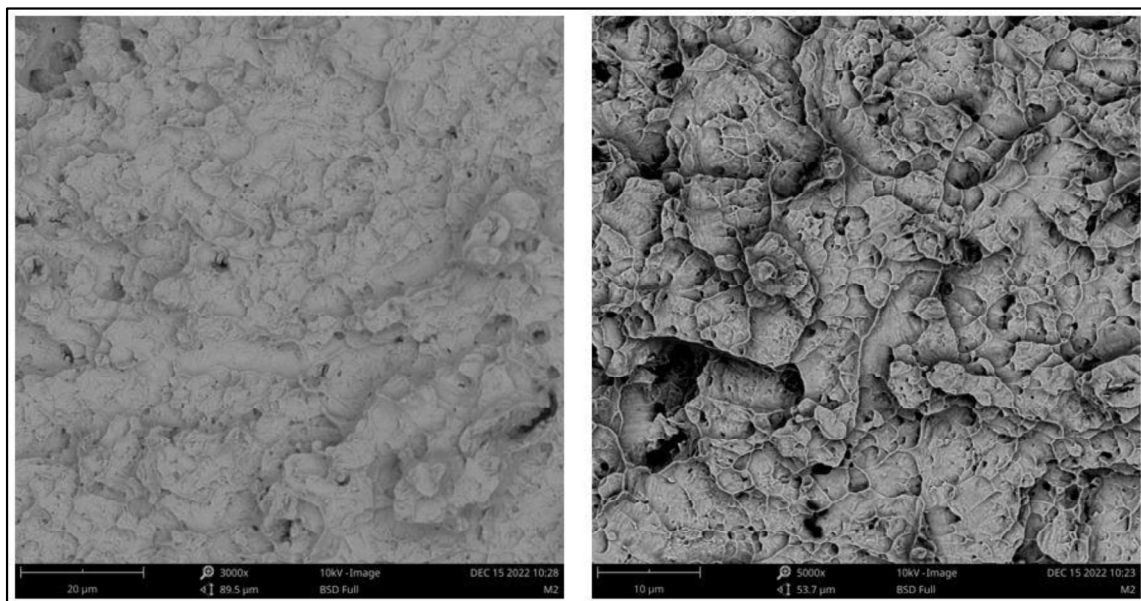


Figure 4.3-11. SEM image from fracture surface of Sample 6 after actuation fatigue experiment

Briefly, HE-PN-AN samples showed almost similar shape memory properties and crack growth behavior with similar and lower crack growth rate.

4.4. Discussions on Actuation Fatigue Testing of HE-PN and HE-PN-AN samples

Crack growth curves of both types of samples, best fit lines and their R-Squared values were shown in Figure 4.4-1. It was seen that the annealed samples showed almost similar increasing crack length trends and crack growth rates, however crack length values of HE-PN samples that were measured at certain number of cycles deviated from each other.

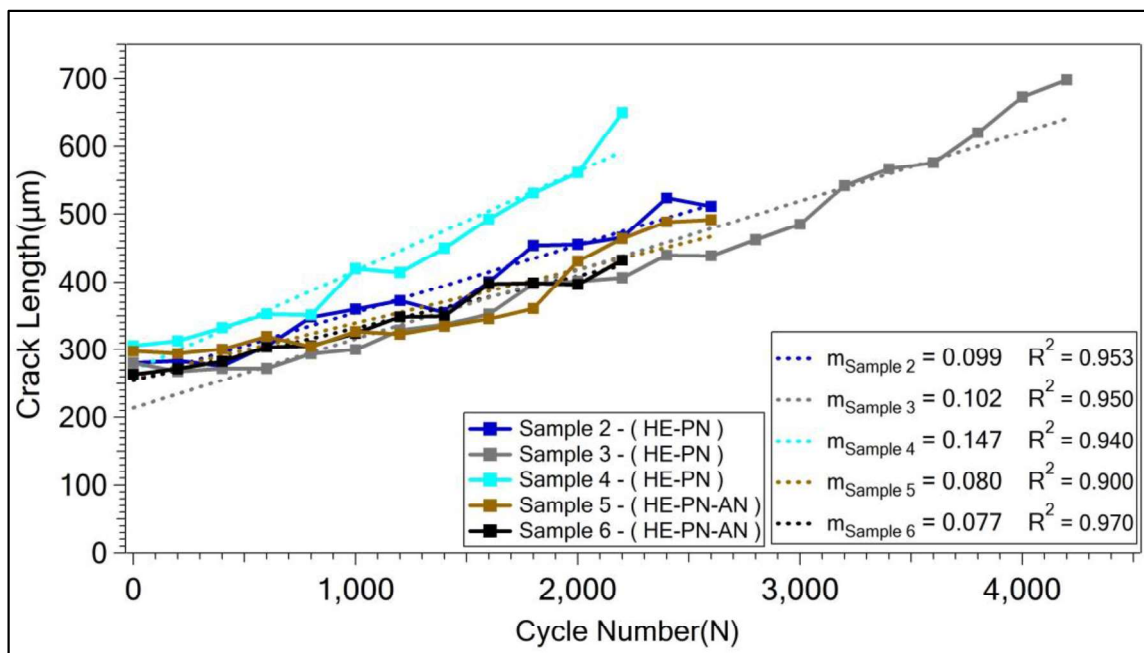


Figure 4.4-1. Evolution of crack lengths with the number of cycles in actuation fatigue cycling of HE-PN and HE-PN-AN samples [67]

Crack growth rate of these two types of samples, which were coded as HE-PN and HE-PN-AN were shown in the table below (Table 4.4-1). Crack growth rate of annealed samples HE-PN-AN resulted lower crack growth rates over the cycles compared to HE-PN samples.

Table 4.4-1. Crack growth rate values (“m”) of HE-PN and HE-PN-AN samples and crack length change trend [67]

“m” Values	Sample 2	Sample 3	Sample 4	Sample 5	Sample 6
Crack Growth Rate (μm/cycle)	0.099	0.102	0.147	0.080	0.077

Figure 4.4-2 contained optical micrographs showing the major crack propagation and minor side crack formations with the number of actuation cycles for both HE-PN and HE-PN-AN samples. Several minor side crack formations were seen on annealed samples over the number of cycles in contrast to HE-PN samples with distinctive major crack that led to fracture. In annealed samples, these minor side cracks propagated with the major crack and reached to almost similar crack lengths after a while. However, there were not many side cracks occurred around the pre-notch of HE-PN samples due to the fact that the growth rate of the major crack was always higher since the work done on HE-PN samples were used for the growth of the major crack instead of creating minor side cracks considering the higher induced stress and dislocation density due to hot extrusion. The higher strength of the HE-PN samples may resist to the formation of side cracks with actuation cycling.

The formation of several minor side cracks and propagation of these cracks in HE-PN-AN samples could be due to annealing process. Such that, annealing process could lead to a stress relief and dislocation rearrangement of hot extrusion process.


























Sample Number and Condition	Cycle Number				
	1,200 th	1,400 th	1,600 th	1,800 th	2,000 th
Sample 2 (HE-PN)					
Sample 3 (HE-PN)					
Sample 4 (HE-PN)					
Sample 5 (HE-PN-AN)					
Sample 6 (HE-PN-AN)					

Figure 4.4-2. Pre-notch, major crack and side crack optical micrographs of HE-PN and HE-PN-AN samples after 1,200th, 1,400th, 1,600th, 1,800th and 2,000th cycles of actuation cycling [67]

As it was mentioned before, work output could be calculated by multiplying the actuation strain with applied stress. Almost similar actuation strain magnitudes (ϵ_{act}) were obtained for all HE-PN and HE-PN-AN samples as shown in Figure 4.4-3 which also meant same work output was achieved from all samples. It is known from the fracture mechanics that energy transformed into work should be used to promote the formation and growth of cracks. This energy converted from work done must be spent on phase transformation, crack formation and crack propagation in samples with pre-notch. The energy spent on crack formations and crack growth would be the same for all samples since the actuation values hence the work output values were determined to be same for all samples. In contrast to the HE-PN samples, where this energy was used for the propagation of pre-notch, the HE-PN-AN samples used the same amount of energy to generate minor side cracks in addition to the propagation of the pre-notch. This might be as a result of relieving hot extrusion-generated stress which was relatively less in the annealed

materials, and made it relatively simple to form new surfaces with spending less energy in annealed samples.

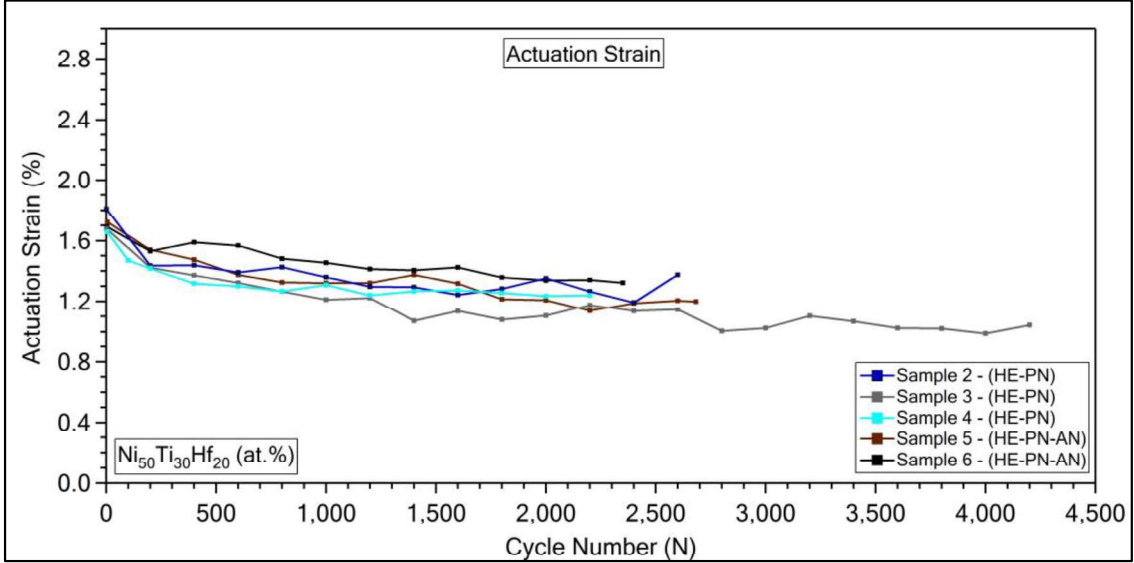


Figure 4.4-3. Actuation strain values determined from Actuation Fatigue experiment conducted on HE-PN and HE-PN-AN Ni₅₀Ti₃₀Hf₂₀ (at.%) samples [67]

Additionally, even if pre-notches were opened at the sample edges using WEDM and this method is thought to be the most suitable one with the pre-notch dimensions, residual stresses may still develop in the vicinity of the pre-notch. The growing rate of the pre-notch in HE-PN-AN samples was reported to be slower than that of HE-PN samples because annealing might reduce these residual stresses.

SIF values were calculated by using the equation of Tada et al. [75] and shown in Figure 4.4-4 for HE-PN and HE-PN-AN samples. SIF values for the first 1,800 cycles of HE-PN-AN samples were nearly the same. Due to the simultaneously joining minor cracks of Sample 5 after 1,800th cycle, an increase was observed. It can be stated that annealing helped to reduce the increase in SIF values following actuation cycles by rearranging dislocations and relieving stresses brought on by the hot extrusion process.

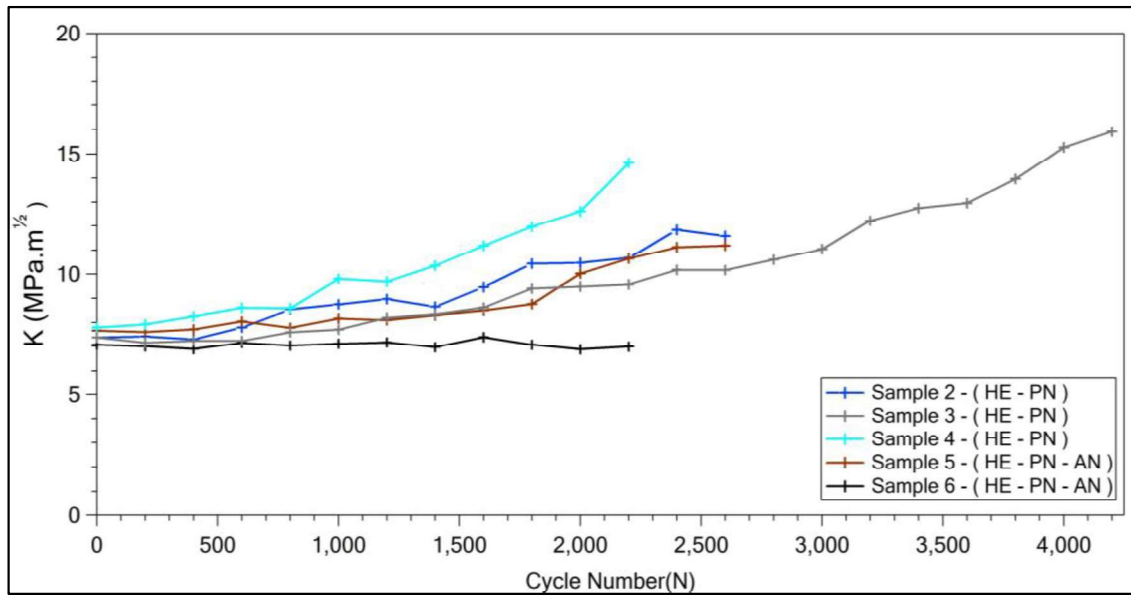


Figure 4.4-4. SIF values calculated for HE-PN and HE-PN-AN samples by the crack lengths at intermittent cycles [67]

4.5. Effect of UCT and Stress on Actuation Fatigue Tests of HE-PN-AN Samples

Actuation fatigue experiments were conducted under two different conditions to see the effect of stress and higher UCT on actuation fatigue and crack growth behavior. Firstly, a sample of HE-PN-AN $\text{Ni}_{50}\text{Ti}_{30}\text{Hf}_{20}$ (at. %) alloy was tested under constant load corresponding to 200 MPa stress with 15°C/s heating-cooling rate (this sample was enumerated with 7) at a different UCT temperature. Sample 7 was thermally cycled under constant load between 600°C and 150°C that were set as UCT and LCT, respectively.

Secondly, another sample was tested under a different stress level than the previous test samples which was 300 MPa with 15°C/s heating cooling rate between 440°C UCT and 150°C LCT temperatures (this sample is called as Sample 8). However, since it was known that TTs could be increased by the increased applied load from previous studies [77], it was necessary to make sure that the 440°C UCT was sufficient to observe full austenitic transformation with the application of 300 MPa. Therefore, HE-PN-AN sample was tested with actuation fatigue cycles under constant load referred to 300 MPa stress magnitude with different UCT values. Strain-Temperature curves were investigated, which were obtained from actuation fatigue experiments that were run for different UCT

values. The curves were shown in Figure 4.5-1. It was determined that 440°C UCT temperature was found to be sufficient for full transformation under stated constant load.

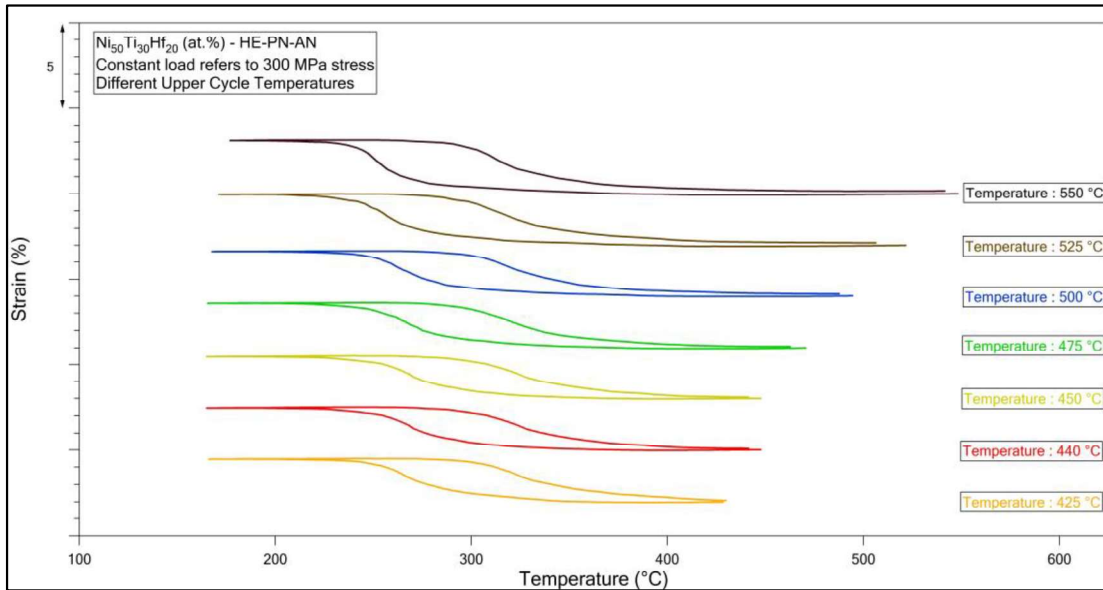


Figure 4.5-1. Strain vs Temperature Curves of HE-PN-AN samples tested under constant load refers to 300 MPa Stress at different UCTs

Sample 7, which was HE-PN-AN tested by setting the UCT to 600°C, was failed after 220 cycles. Strain-Temperature curves, which were gathered from different cycles of Sample 7, were shown in Figure 4.5-2 (a). Difference between strain at austenite phase and martensite phase increased with the number of cycles and curves were widened over the number of cycles.

Additionally, Sample 8 (HE-PN-AN) was tested under higher constant load which corresponded to 300 MPa stress magnitude was failed after 280 actuation cycles. Strain-Temperature curves of Sample 8 showed similar curves with the previous actuation fatigue tests with 440°C UCT under 200 MPa with the increasing number of cycles (Figure 4.5-2 (b)). By using these curves, values defining the actuation fatigue and shape memory properties were extracted then shown in subsequent figures in the following paragraphs.

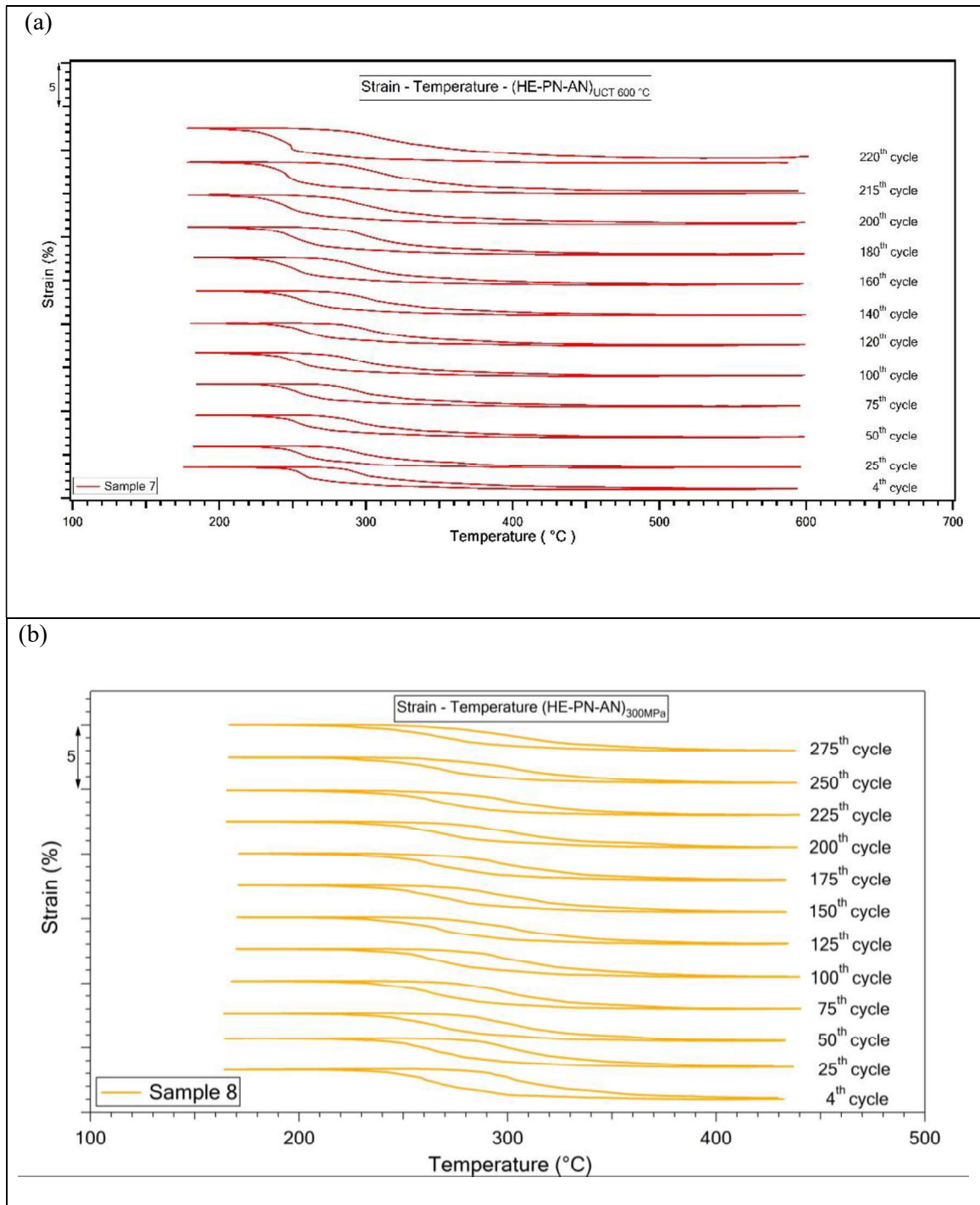


Figure 4.5-2. Strain-Temperature curves from the actuation fatigue experiment of $\text{Ni}_{50}\text{Ti}_{30}\text{Hf}_{20}$ (at. %) HE-PN-AN sample (a) under 200 MPa with 600°C UCT, (b) under 300 MPa with 440°C UCT.

Sample 7 and Sample 8 exhibited TTs almost in similar magnitudes until 140th cycle. While Sample 8 showed stable TTs, TTs of Sample 7 diverted from the TTs of Sample 8 starting from the 140th cycle as can be seen in Figure 4.5-3.

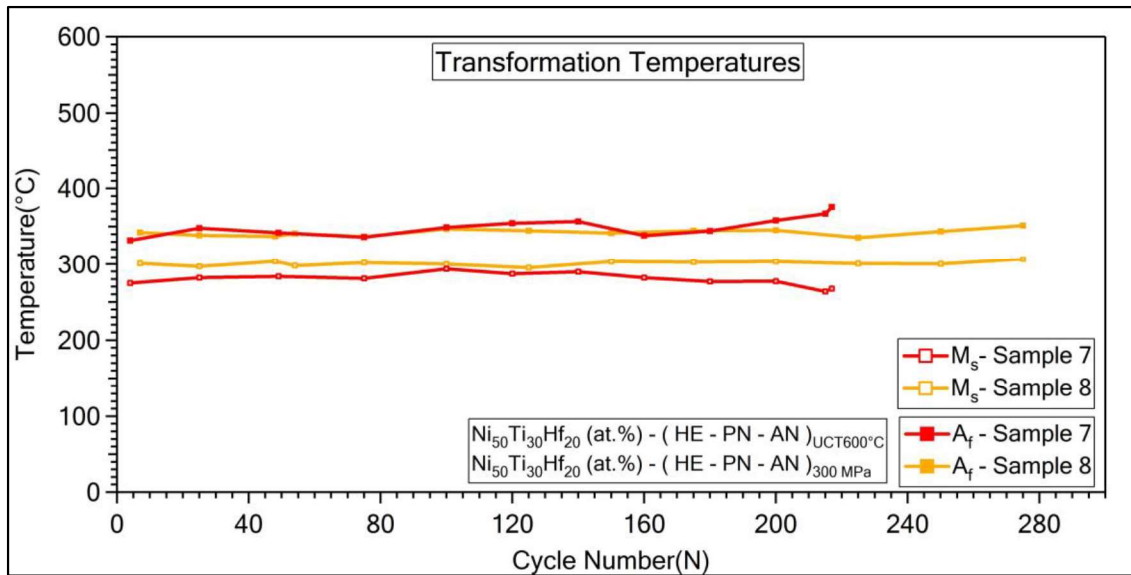


Figure 4.5-3. TT evolution determined from Actuation Fatigue experiment conducted on HE-PN-AN $\text{Ni}_{50}\text{Ti}_{30}\text{Hf}_{20}$ (at. %) sample under 200 MPa with 600°C UCT for Sample 7 and actuation fatigue test under 300 MPa with 440°C UCT for Sample 8.

Actuation strain values of Sample 8, which were thermally cycled under 300 MPa, were decreased with the number of cycles as it was shown in other studies on NiTiHf alloys due to the plastic strain accumulation and remnant martensites that were pinned by the phase transformation induced dislocations [29,76]. However, Sample 7, which was tested using higher UCT, showed an increase in actuation strain value. This increase was attributed to oxidation-based crack growth and the higher transforming volume of martensite to austenite with the increase in UCT. Also, creep induced plasticity could be effective at higher temperatures. It is worth to mention that the dislocations become mobile at relatively higher UCT and therefore they may lose their pinning effect and the martensite-austenite boundaries become mobile as well.

It's known from the previous study that higher UCT reduces the fatigue life of HTSMAs [18]. Increase in UCT also increase the actuation strain value since further heating could be required in some local areas for further transformation of martensite to austenite. The dislocation accumulation over the number of cycles could lead to dislocation barriers which could be overcome by overheating. Also, increase in actuation strain would lead to more crack opening and closing and that could promote crack growth.

Sample 8 showed better cyclic stability in terms of actuation strain under higher stress magnitude.

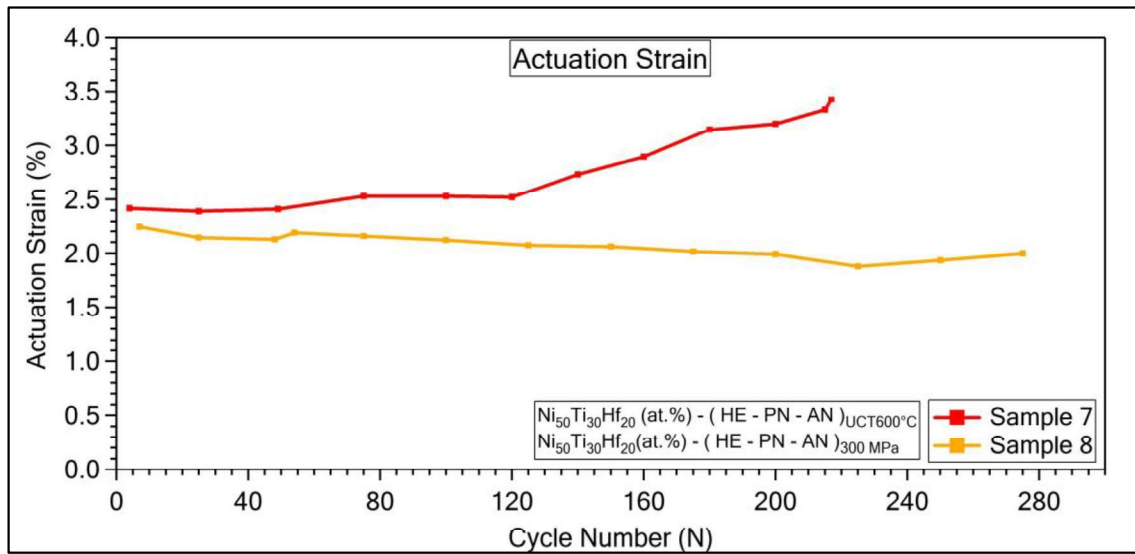


Figure 4.5-4. Actuation strain values determined from Actuation Fatigue experiment on HE-PN-AN $\text{Ni}_{50}\text{Ti}_{30}\text{Hf}_{20}$ (at. %) sample under 200 MPa with 600°C UCT for Sample 7 and actuation fatigue test under 300 MPa with 440°C UCT for Sample 8.

Accumulated irrecoverable strain values increased over the number of cycles in HE-PN-AN samples, and both samples resulted almost similar values in the beginning of the actuation fatigue cycles as presented in Figure 4.5-5. However, the accumulated irrecoverable strain values of Sample 7, which was tested using higher UCT, showed a deviation after 60th cycles. It showed a significant amount of irrecoverable strain through the actuation fatigue cycles which might be due to high temperature-based crack opening closing behavior during actuations leading to observe higher strain values.

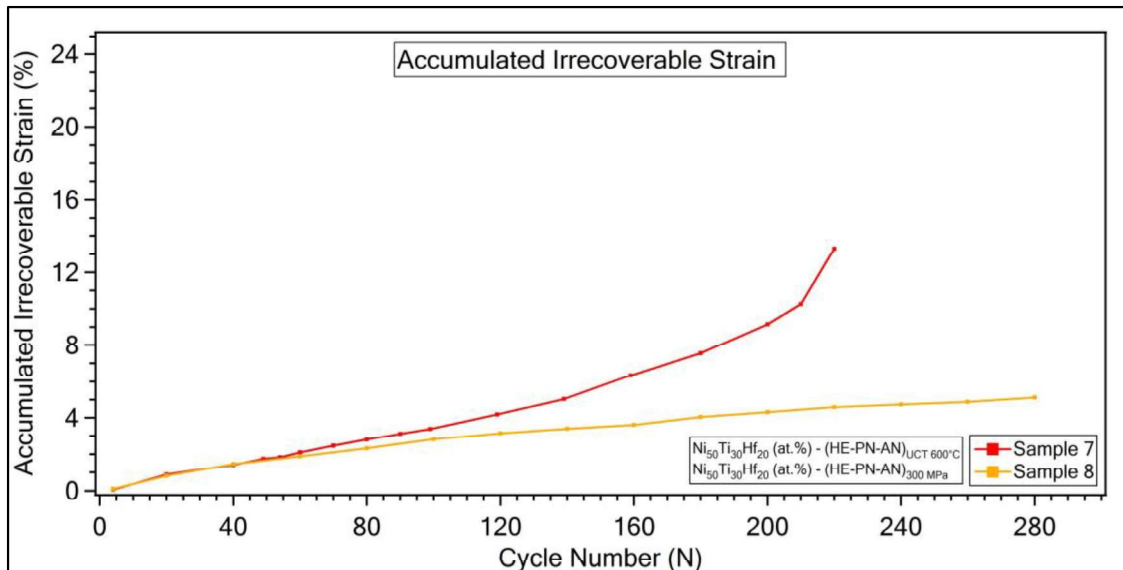


Figure 4.5-5. Accumulated irrecoverable strain values determined from Actuation Fatigue experiment conducted on HE-PN-AN Ni₅₀Ti₃₀Hf₂₀ (at.%) samples under 200 MPa with 600°C UCT for Sample 7 and actuation fatigue test under 300 MPa with 440°C UCT for Sample 8.

Thermal hysteresis values stayed almost constant in Sample 8, but Sample 7 tested at higher UCT resulted higher thermal hysteresis after 160 cycles as seen in Figure 4.5-6.

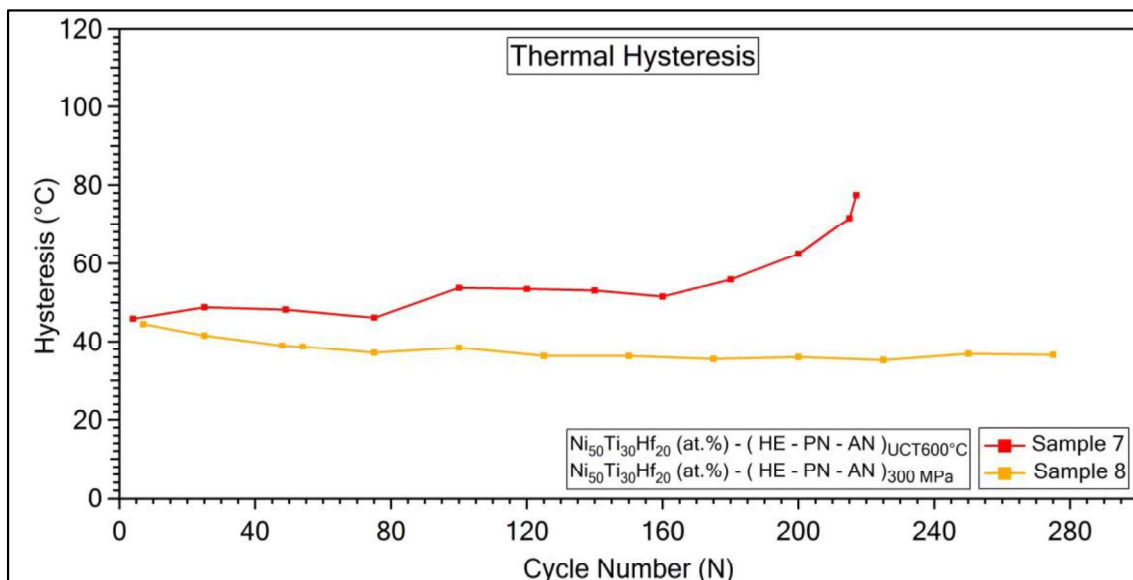


Figure 4.5-6. Thermal hysteresis values determined from actuation fatigue experiments of Ni₅₀Ti₃₀Hf₂₀ (at.%) HE-PN-AN samples under 200 MPa with 600°C UCT for Sample 7 and actuation fatigue test under 300 MPa with 440°C UCT for Sample 8.

Crack formations were investigated by using optical micrographs taken after intermittent actuation cycles for Sample 7 and Sample 8. Small crack initiations were observed with the 50th cycle, however propagations of these cracks were not clear. A major crack leading to fracture could not be observed in Sample 7 that was tested using higher UCT as can be seen in Figure 4.5-7. Many surface cracks were propagated together during the actuation cycles due to high UCT and high temperature-based surface oxidation that led to observe many surface cracks. Thus, crack growth curves could not be drawn due to indistinctive crack length.

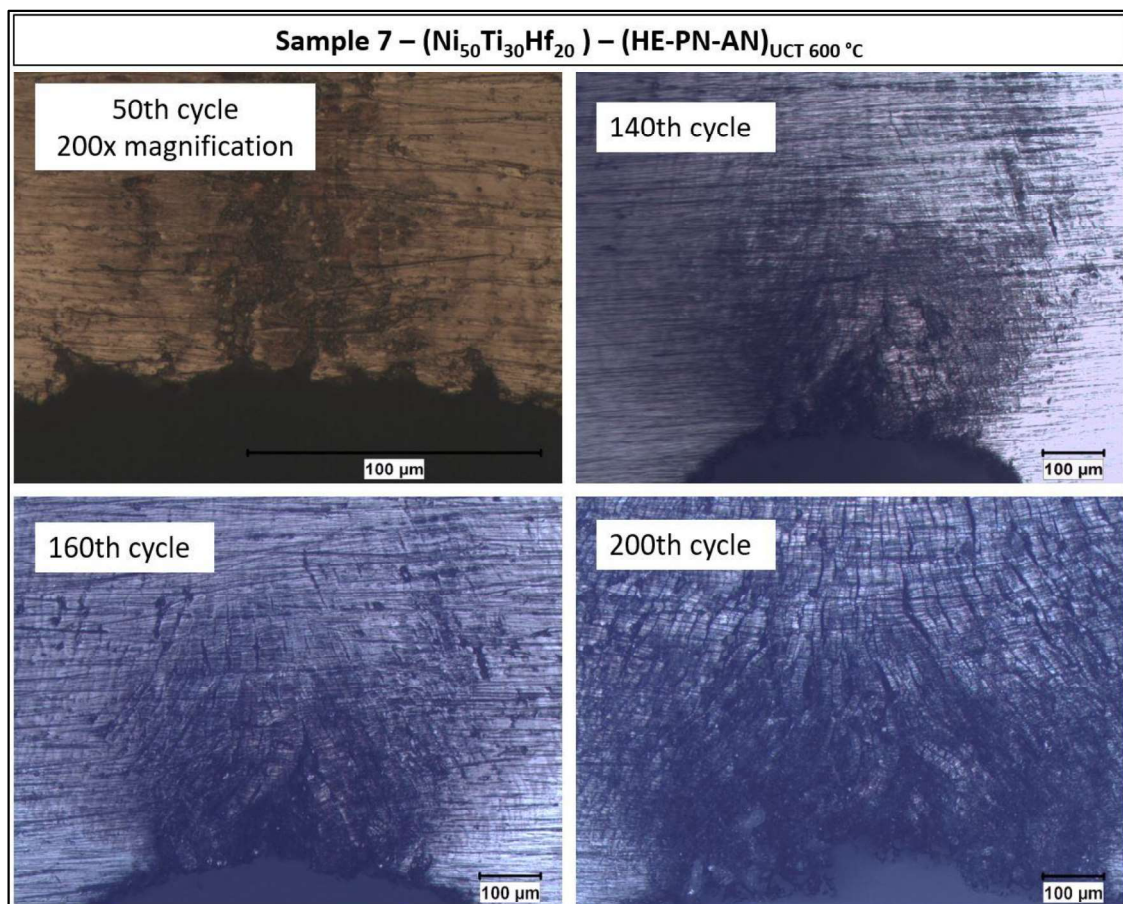


Figure 4.5-7. Optical micrographs taken after intermittent actuation cycles for Sample 7

Optical micrographs showing the pre-notch area of Sample 8 were presented for 75th and 200th cycles in Figure 4.5-8. Sample had small sized micro cracks at 75th cycle, however there was no noticeable difference in length of the initiated cracks in the next intermittent cycle, which was 200th cycle. Then, sample was failed after 280th cycle without showing a distinctive crack formation. Therefore, crack length with the number of cycles curves could not be drawn for Sample 8.

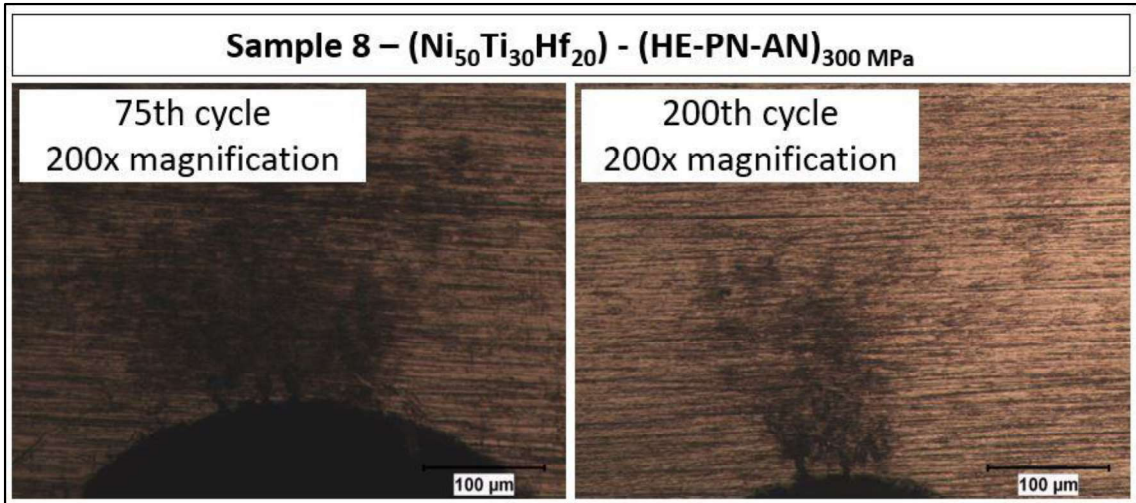


Figure 4.5-8. Optical micrographs taken after intermittent actuation cycles for Sample 8

Fracture surfaces of failed Sample 7 and Sample 8 were shown in Figure 4.5-9. Fracture morphology of the Sample 7 which was actuation fatigue cycled using higher UCT showed mostly intergranular fracture surfaces with many micro voids called as dimples. However, less dimples and intergranular fracture manner had been seen on the fracture surface of Sample 8. Higher UCT application led to mostly intergranular cracking as already stated in the work of Karakoc et al. at which the actuation fatigue cycles were run using higher UCT temperatures [18].

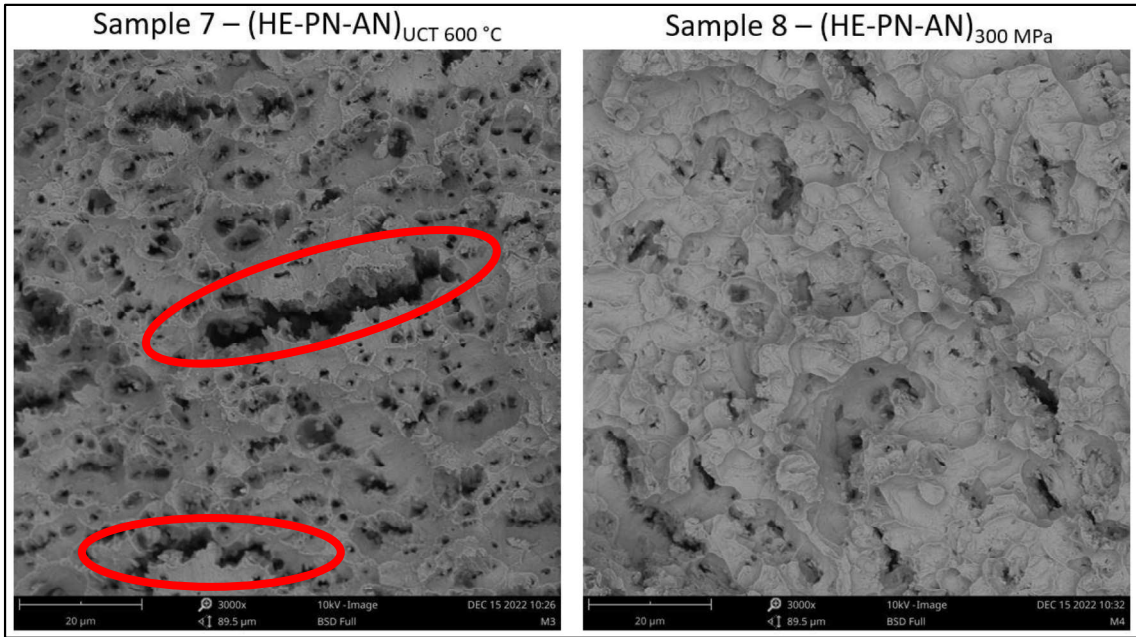


Figure 4.5-9. SEM Images from fracture surface of Sample 7 and Sample 8 after actuation fatigue experiments

From the SEM images showing the fracture surfaces of the failed samples in Figure 4.5-9, it can be seen that the higher UCT level (600°C) provoked the formation of many dimples and several elongated cracks which were probably due to the corporation of the dimples as shown with the red circles in Figure 4.5-9. Observing more dimples on the fracture surface might be attributed to the increased actuation strain due to the crack opening-closing during phase transformation that led to the formation of many small cracks inside [18].

4.6. Actuation Fatigue Testing of Ni₅₀Ti₂₅Hf₂₅ (at.%) HE-PN-AN alloy

A sample of Ni₅₀Ti₂₅Hf₂₅ (at.%) were tested to investigate the actuation fatigue performance and crack propagation behavior of a NiTiHf alloy having higher Hf content (25 at.% Hf). It is known that the TTs increase in NiTiHf alloys with the increasing content of Hafnium. Thus, Ni₅₀Ti₂₅Hf₂₅ (at.%) has higher TTs compared to Ni₅₀Ti₃₀Hf₂₀ (at. %) alloy. Stress-free TTs of annealed Ni₅₀Ti₂₅Hf₂₅ (at.%) were shown in Table 4.6-1 which was previously determined and reported by our lab group for the same batch of alloy.

Table 4.6-1. Stress-free TTs of annealed Ni₅₀Ti₂₅Hf₂₅ (at.%) alloys

	Stress-free TTs of annealed Ni ₅₀ Ti ₂₅ Hf ₂₅ (at.%)			
	A _f	A _s	M _s	M _f
Temperatures (°C)	434	398	368	324

Actuation fatigue experiments were conducted on HE-PN-AN Ni₅₀Ti₂₅Hf₂₅ (at.%) alloy under constant load corresponding to 200 MPa stress with 15°C/s heating-cooling rate (this sample is called as Sample 9). UCT temperature value was chosen as 600°C to observe full phase transformation along the cycles since Ni₅₀Ti₂₅Hf₂₅ (at.%) had higher TTs than that of Ni₅₀Ti₃₀Hf₂₀ (at.%) alloys. Sample 9 had performed 222 actuation fatigue cycles under load and strain-temperature curves that were obtained from different cycles were given in Figure 4.6-1.

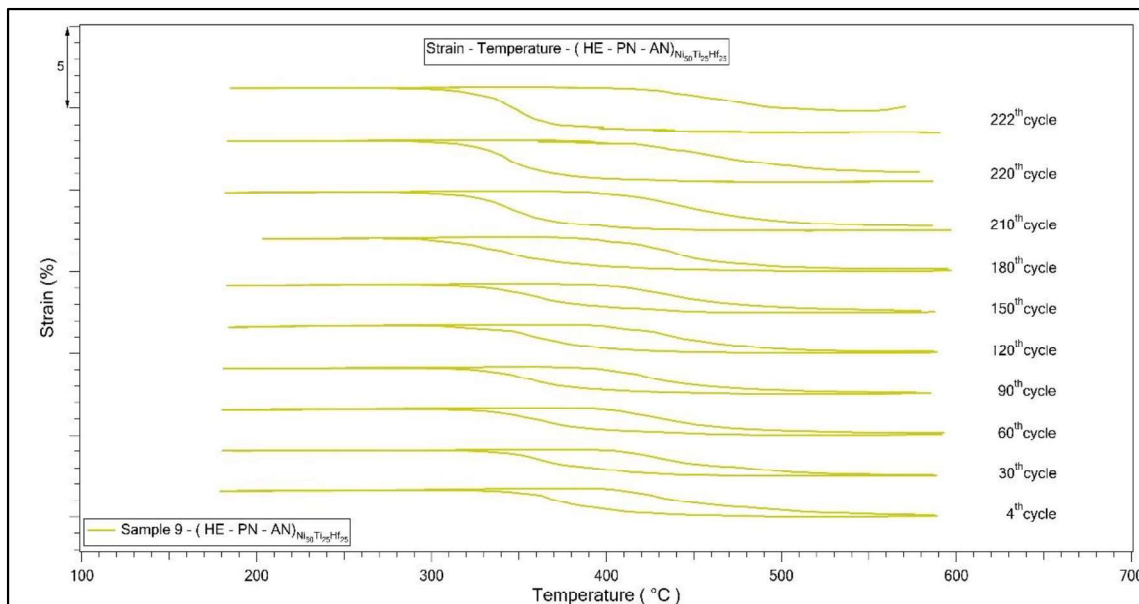


Figure 4.6-1. Strain-Temperature curves from the actuation fatigue experiment of $\text{Ni}_{50}\text{Ti}_{25}\text{Hf}_{25}$ (at.%) HE-PN-AN sample under 200 MPa with 600°C UCT

TTs that were extracted from strain-temperature curves of Sample 9 were shown in Figure 4.6-2. Stable transformation temperatures were observed throughout the lifetime of Sample 9.

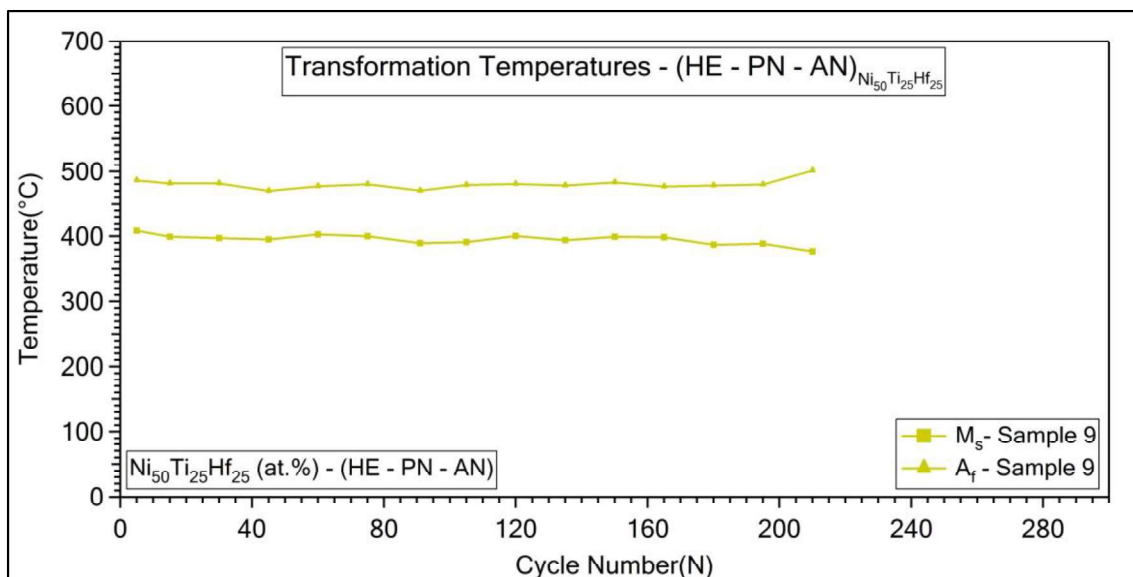


Figure 4.6-2. Evolution of TTs, which were determined from Actuation Fatigue experiment conducted on HE-PN-AN $\text{Ni}_{50}\text{Ti}_{25}\text{Hf}_{25}$ (at.%) sample under 200 MPa with 600°C UCT

Actuation strain values of the Sample 9 with respect to number of cycles were shown in Figure 4.6-3 where actuation strain values were determined to be stable until 150th cycle and then increased until fracture.

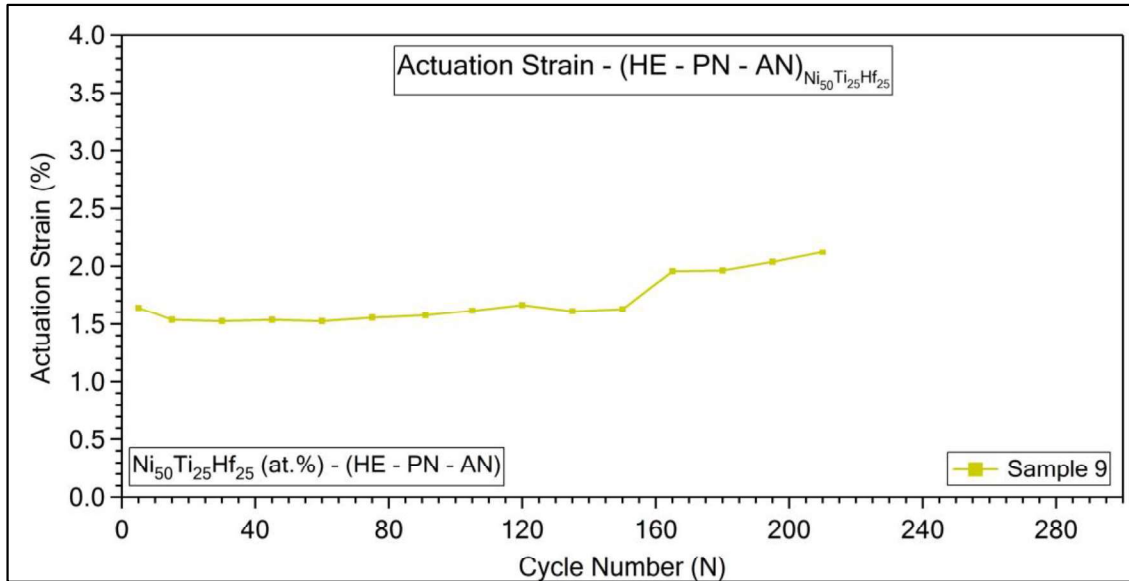


Figure 4.6-3. Actuation strain values determined from Actuation Fatigue experiment on HE-PN-AN Ni₅₀Ti₂₅Hf₂₅ (at.%) sample under 200 MPa with 600°C UCT

Sample 9 exhibited a significant amount of accumulated irrecoverable strain through the actuation fatigue cycles (Figure 4.6-4). Highly increased values over the number of cycles might be due to significant propagation of cracks due to severe oxidation of Sample 9 at high temperature. Also, similar increasing trend was obtained in testing of Sample 7 (Ni₅₀Ti₃₀Hf₂₀ (at.%) alloy) that was tested using higher UCT.

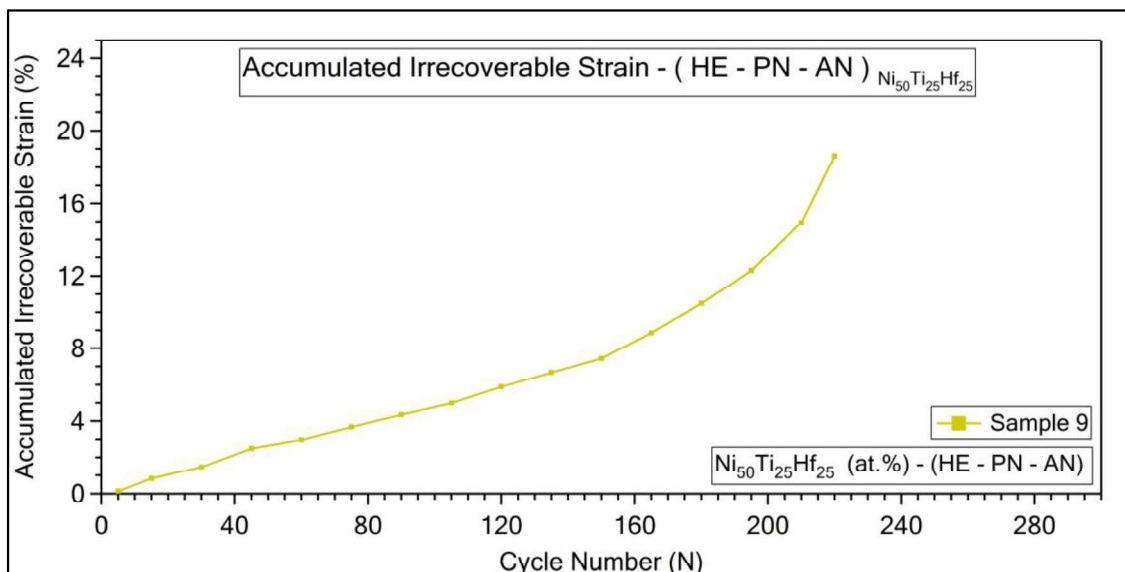


Figure 4.6-4. Accumulated irrecoverable strain values determined from Actuation Fatigue experiment conducted on HE-PN-AN $\text{Ni}_{50}\text{Ti}_{25}\text{Hf}_{25}$ (at.%) samples under 200 MPa with 600°C UCT for Sample 9

Thermal hysteresis values stayed almost the same during the first 90 cycles then started to increase in HE-PN-AN Sample 9 as shown in Figure 4.6-5. Thermal hysteresis values increased significantly as the accumulated strain increased due to propagation of the cracks due to oxidation. Then, transformation became harder by the increased plastic strain over the number of actuation cycles such that higher overheating and undercooling became necessary to observe full phase transformation.

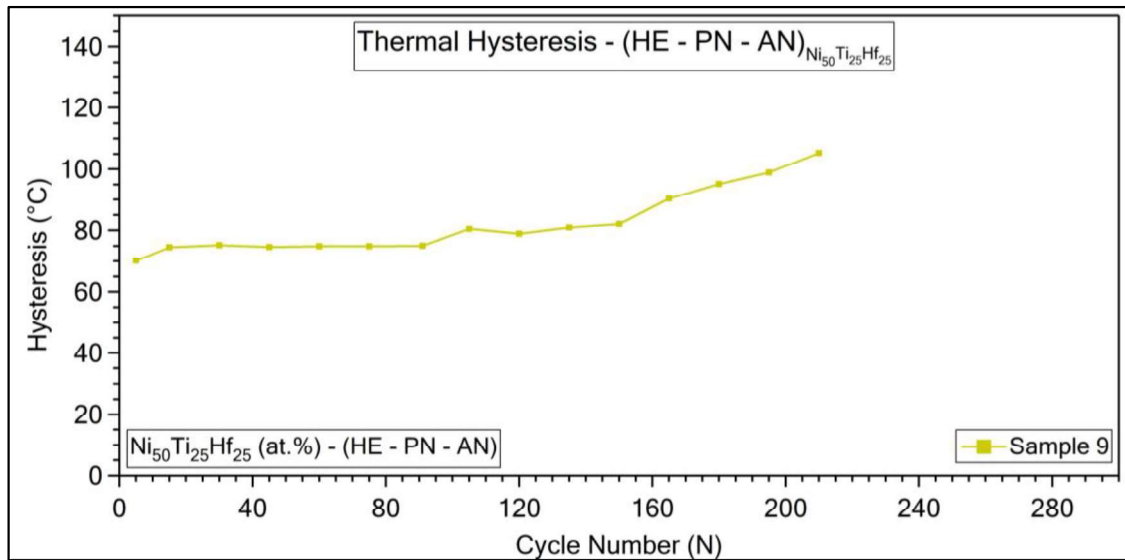


Figure 4.6-5. Thermal hysteresis values determined from actuation fatigue experiments of $\text{Ni}_{50}\text{Ti}_{25}\text{Hf}_{25}$ (at.%) HE-PN-AN samples under 200 MPa with 600°C UCT for Sample 9

Crack formations were investigated by using optical micrographs taken after intermittent actuation cycles for Sample 9 and shown in Figure 4.6-6. Crack initiations at the tip of the pre-notch and on the surface started at 50th cycle. There were distinctive cracks at intermittent cycles leading to fracture, however they propagated with the rate, which was determined by taking the micrographs the same cycle optical micrographs. Observation of several crack formations and propagations around the pre-notch and different form of surface cracks was attributed to of the higher Hf content in $\text{Ni}_{50}\text{Ti}_{25}\text{Hf}_{25}$ (at.%) alloy compared to $\text{Ni}_{50}\text{Ti}_{30}\text{Hf}_{20}$ (at.%) alloy. It has been already known that the affinity of Hf to Oxygen is very high. Therefore, relatively thicker Hf rich oxide layer may form in $\text{Ni}_{50}\text{Ti}_{25}\text{Hf}_{25}$ (at.%) due to higher Hf content. Since HfO is very hard and brittle more surface cracks might be formed [78].

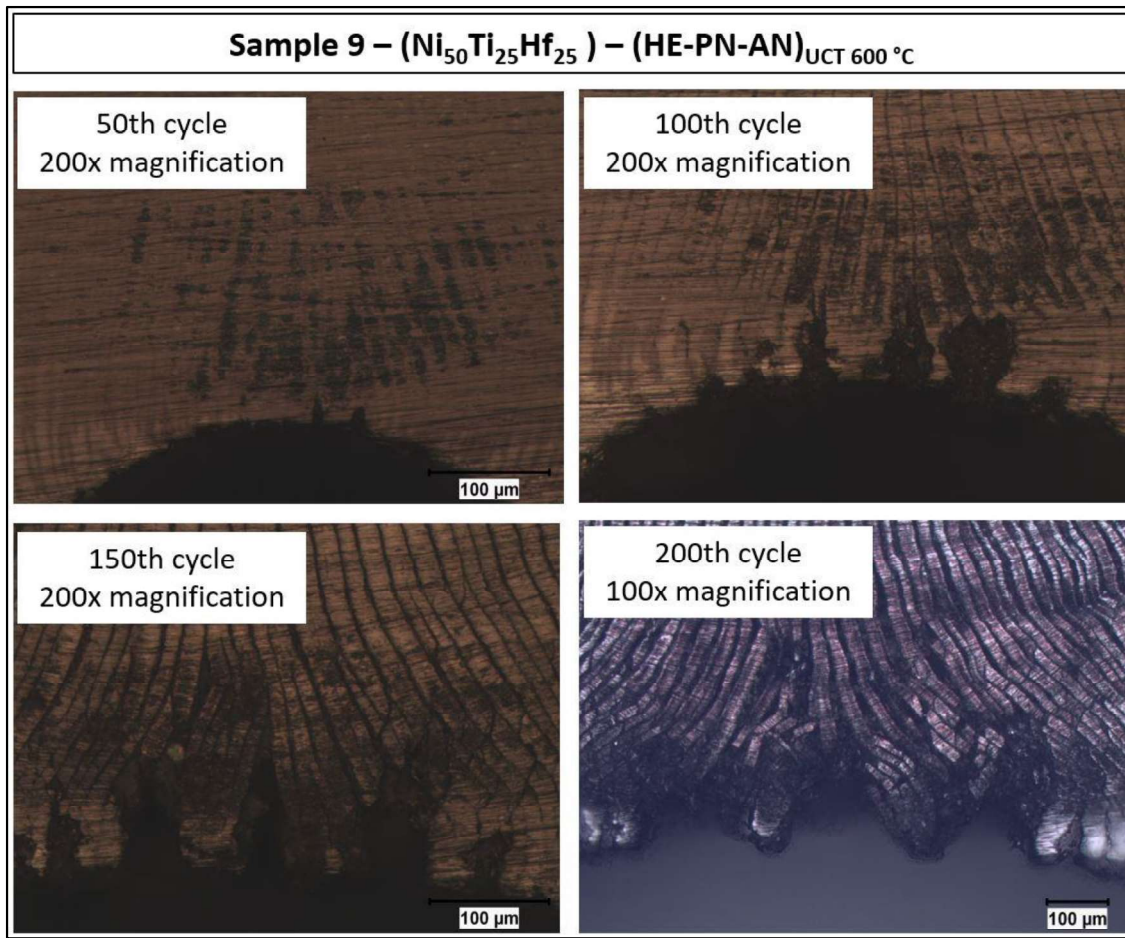


Figure 4.6-6. Optical micrographs taken after intermittent actuation cycles for Sample 9

3 distinctive cracks, which were propagated during the actuation cycles and led to fracture, were observed in the pre-notch area, however, their propagation rates were similar since they were in same sizes at the same cycles as can be seen in the micrographs. Thus, to draw crack length with the number of cycle curves and to calculate the crack growth rate, middle crack, which propagated a little faster than that of the other cracks, was followed in length measurements during the cycles (Figure 4.6-7). Best fit curve used to calculate the crack growth rate and its R-Squared value were also given in the figure. It was seen that the Sample 9 had 0.661 $\mu\text{m}/\text{cycle}$ crack growth rate value which was almost 9 times higher than the crack growth rates of annealed samples (Sample 5 and Sample 6). However, SIF values couldn't be calculated properly since the pre-notch section was highly deformed such that the shape of the pre-notch had undergone a huge change. So, the dimensions of the pre-notch could not be measured after intermittent cycles.

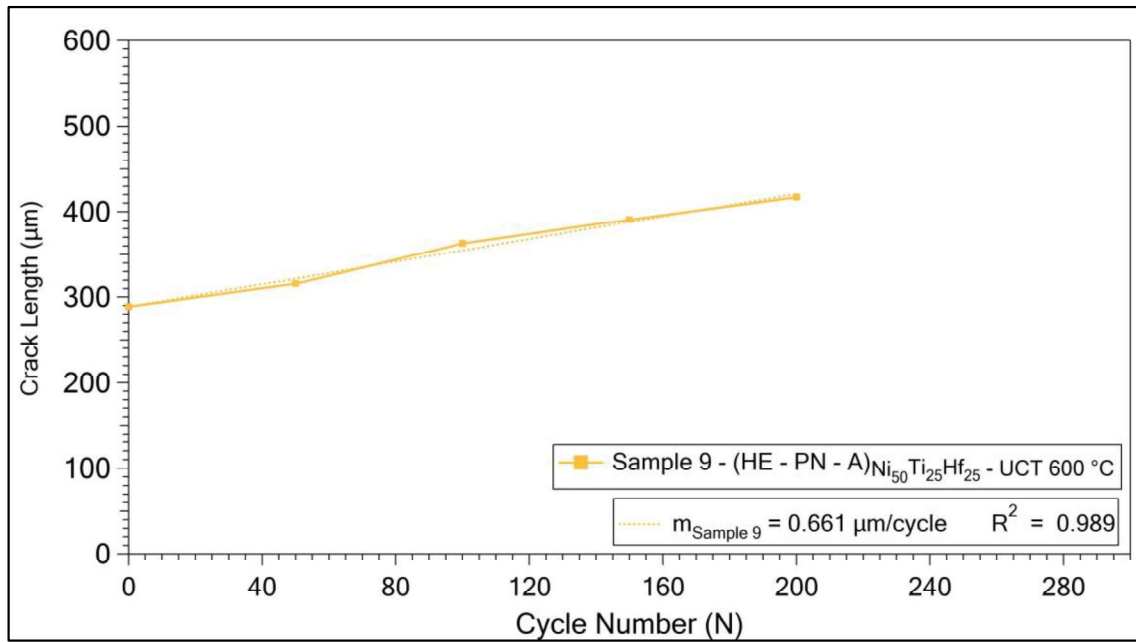


Figure 4.6-7. Evolution of crack lengths with the number of cycles in actuation fatigue cycling of Ni₅₀Ti₂₅Hf₂₅ (at.%) HE-PN-AN Sample 9

Fracture surface of failed Sample 9 was demonstrated in Figure 4.6-8. Fracture morphology of the Sample 9 which was actuation fatigue cycled using 600°C UCT showed mainly intergranular mode with many small micro voids that can be called as cup coned dimples.

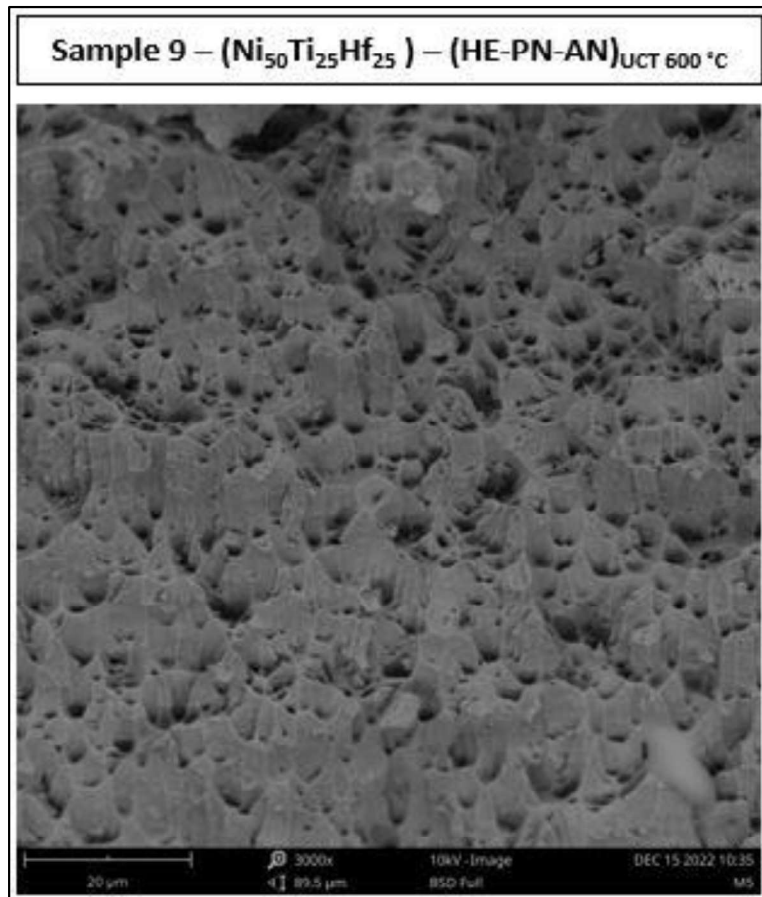


Figure 4.6-8. SEM Images from fracture surface of Sample 9 after actuation fatigue experiment

4.7. Effect of UCT, Stress and Hf content on Actuation Fatigue and comparison of actuation fatigue results

Results of actuation fatigue experiments under constant load for Sample 4, Sample 6, Sample 7, Sample 8 and Sample 9 were shown in this section to investigate the effects of UCT, applied stress and Hf content on actuation fatigue and crack growth behavior of the alloys that were used in this study.

Firstly, Sample 9, which was tested on $\text{Ni}_{50}\text{Ti}_{25}\text{Hf}_{25}$ (at.%) alloy, showed higher TTs compared to $\text{Ni}_{50}\text{Ti}_{30}\text{Hf}_{20}$ (at.%) alloys as expected during actuation fatigue experiments since Hf content increases the TTs. Additionally, it could be seen that higher UCT could result relatively unstable TTs over the actuation fatigue cycles as was seen in Sample 7 and Sample 9 that were tested using higher UCT and as was shown in Figure 4.7-1.

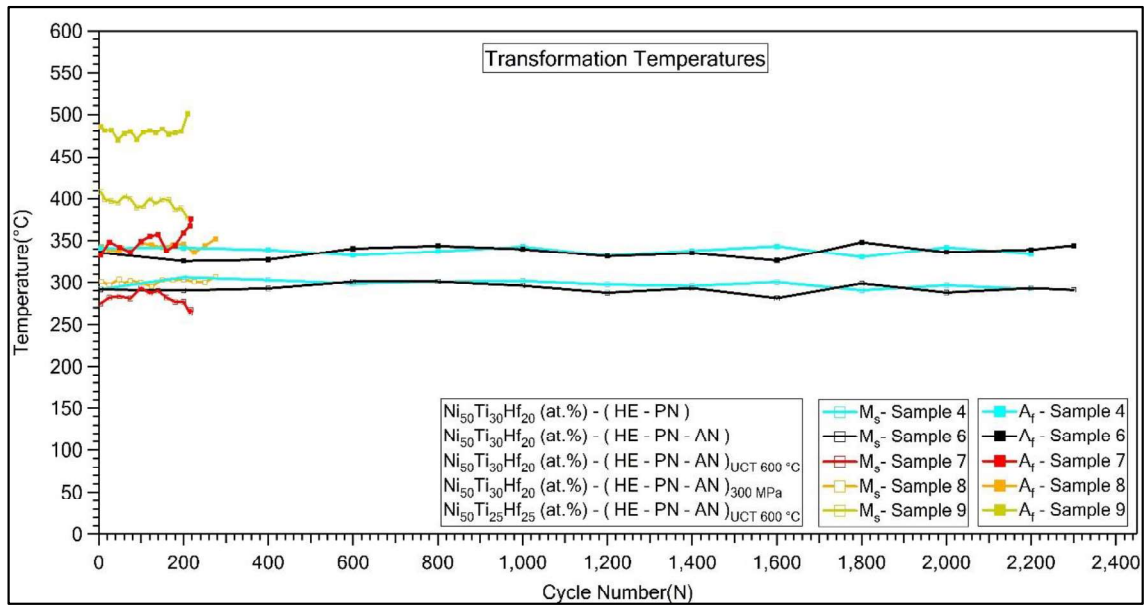


Figure 4.7-1. Evolution of TTs, which were determined from Actuation Fatigue experiment conducted on Sample 4, Sample 6, Sample 7, Sample 8 and Sample 9

Secondly, actuation strain values of the samples (Sample 4, Sample 6) that were thermally cycled using 440°C UCT under constant load corresponds to 200 MPa stress were decreased with the number of actuation cycles. Same decrease in actuation strain values was observed through the actuation cycles of Sample 8 that was tested using 440°C UCT under 300 MPa stress. This decrease was due to the plastic strain accumulation and formation of remnant martensite with the actuation cycles.

However, Sample 7 and Sample 9 that were thermally cycled using 600°C UCT showed increasing trend of actuation strain value. This might be due to further heating of the samples to higher UCT which could help on some local non-transformed areas to further transformation of martensite to austenite. Also, the increased mobility of the dislocations by overheating could lead to the increase in the transforming volume of martensite. But, sharp increase in the actuation strain values of both samples might be attributed to the crack growth due to severe oxidation at higher temperatures. Also, increase in actuation strain might lead to more crack opening and closing which actually promoted crack growth. Many dimples had been seen on the fracture surface of the samples that were tested using higher UCT levels due to this crack growth behavior.

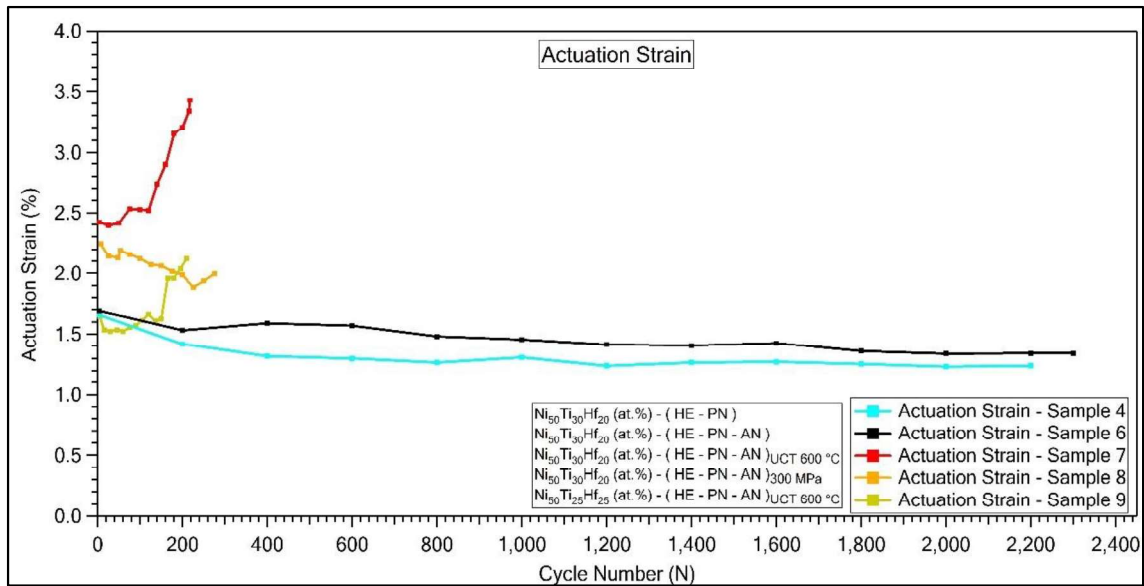


Figure 4.7-2. Actuation strain values determined from Actuation Fatigue experiment on Sample 4, Sample 6, Sample 7, Sample 8 and Sample 9

Thirdly, when the accumulated irrecoverable strain values over the number of cycles were investigated, all samples showed similar increasing trend of irrecoverable strain at the beginning. However, Sample 9 and Sample 7 tested with higher UCT values exhibited a significant amount of increase in accumulated irrecoverable strain values after running a few actuation fatigue cycles as can be seen in Figure 4.7-3. These two samples showed totally different accumulated irrecoverable strain trend compared to others.

Tremendous increase in accumulated irrecoverable strain values over the number of cycles might be due to significant propagation of crack which formed and propagate with the severe oxidation at high temperature and possible dislocation formations via phase transformation in Samples tested using 600°C UCT.

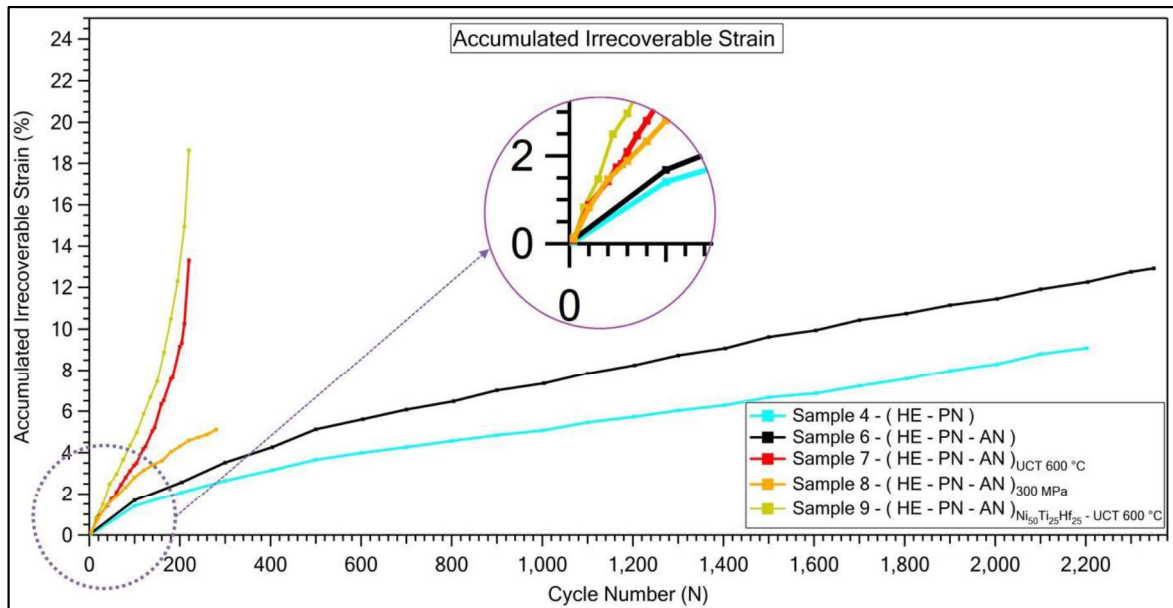


Figure 4.7-3. Accumulated irrecoverable strain values determined from Actuation Fatigue experiment conducted on Sample 4, Sample 6, Sample 7, Sample 8 and Sample 9

Furthermore, distinctive effect of using 600°C UCT on thermal hysteresis could be seen in Figure 4.7-4. There was a step increase in hysteresis values of Sample 7 and Sample 9 tested using higher UCT. Large thermal hysteresis and a step increase were observed in $\text{Ni}_{50}\text{Ti}_{25}\text{Hf}_{25}$ (at.%) alloys.

Thermal hysteresis values together with the accumulated irrecoverable strain increased due to the decrease in the strength of the alloy at high temperatures. The formation and accumulation of dislocations in alloys that have lower strength are easier. As the dislocation density increases, more overheating and undercooling should be applied to overcome the pinning effect of dislocations and to observe the full transformation, therefore the thermal hysteresis increases. Additionally, the crack formation and propagation became easier since the alloy having lower strength cannot resist to either crack initiation or propagation as well and this leads to observe premature failure.

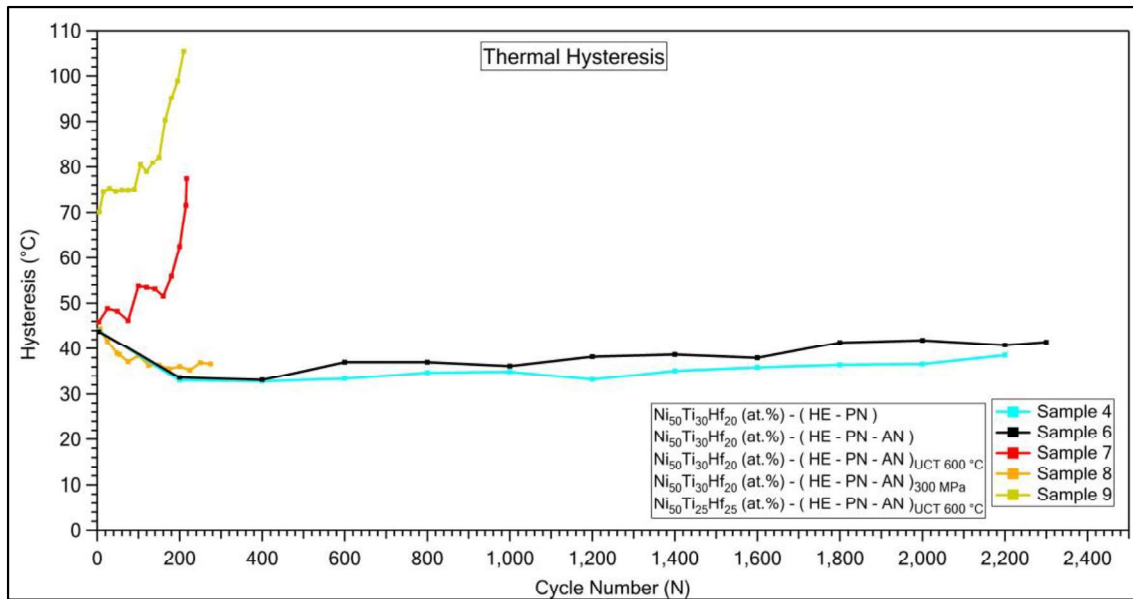


Figure 4.7-4. Thermal hysteresis values determined from actuation fatigue experiments of Sample 4, Sample 6, Sample 7, Sample 8, Sample 9

Effect of higher UCT temperature was also seen on surface crack formations from optical micrographs that were taken after intermittent actuation cycles for Sample 7 and Sample 9. Many surface cracks were propagated together during the actuation cycles because of the high UCT value that caused more oxidation.

Several crack formations and propagations around the pre-notch and especially different form of surface cracks were attributed to the increase of Hf content in $\text{Ni}_{50}\text{Ti}_{25}\text{Hf}_{25}$ (at.%) alloys compared to $\text{Ni}_{50}\text{Ti}_{30}\text{Hf}_{20}$ (at.%) alloys. Hf has high affinity to oxidation thus the oxidation became easier. HfO is very hard and brittle and forms relatively uniform on the surface which led to very high surface crack formations.

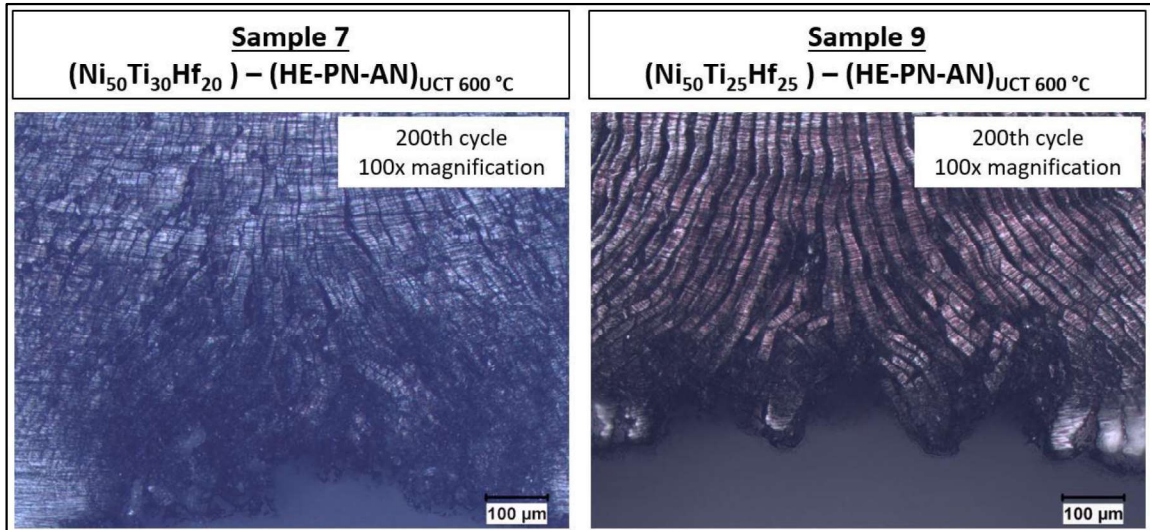


Figure 4.7-5. Optical micrographs taken after 200th intermittent actuation cycles for Sample 7 and Sample 9

Fracture surface SEM images of failed samples were shown in Figure 4.7-6. Fracture morphology of the Sample 7 and Sample 9 which were thermally cycled using 600°C UCT showed intergranular fracture surfaces mostly with many small dimples. This might be due to higher UCT application based higher actuation strain and relatively more crack opening-closing behavior during actuation cycling.

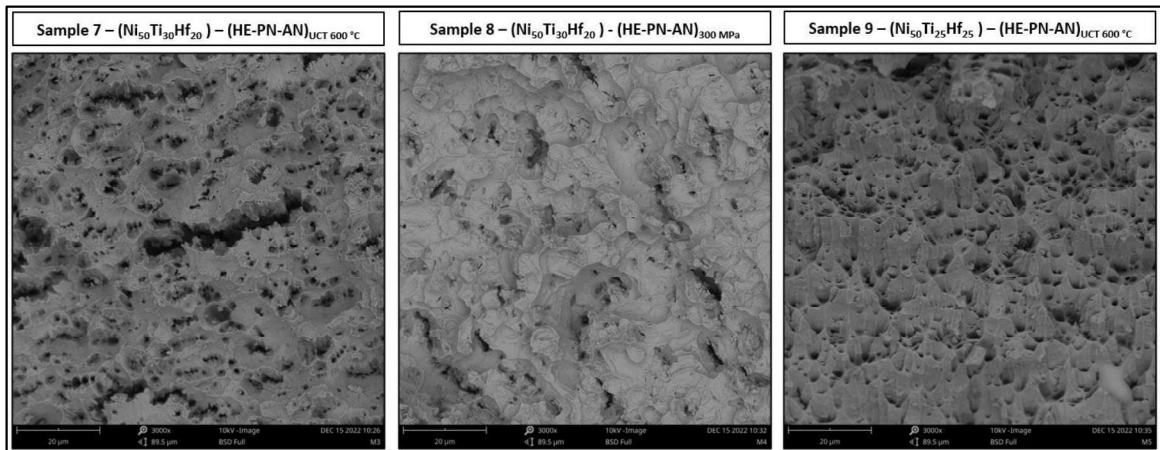


Figure 4.7-6. SEM Images from fracture surface of Sample 7, Sample 8 and Sample 9 after actuation fatigue experiment

4.8. Creep Experiment Results

Creep experiments were applied to HE-PN-AN $\text{Ni}_{50}\text{Ti}_{30}\text{Hf}_{20}$ alloys at 600°C under 3 different stress conditions which were 300 MPa, 400 MPa and 500 MPa and applied by dead weights. The magnitude of the dead weights was calculated according to the initial cross section of the samples for the selected stress magnitudes.

Sample 10, Sample 11 and Sample 12 were held under 300 MPa, 400 MPa and 500 MPa, respectively at 600°C . 600°C was chosen as the creep temperature since the highest accumulated irrecoverable strain values were obtained when the alloy was tested using 600°C UCT. This was considered as a sign that 600°C UCT might cause severe creep deformation. Each sample was detached multiple times from the test set-up at different time intervals to obtain the optical micrographs of the surface cracks. Therefore, strain rate curves were shown in different colors for different intervals of the creep tests which were conducted under 3 different stress levels as shown in Figure 4.8-1.

Strain rates were calculated as strain rate per seconds. Sample 10, Sample 11 and Sample 12 were failed after 286 minutes, 185 minutes and 16 minutes respectively.

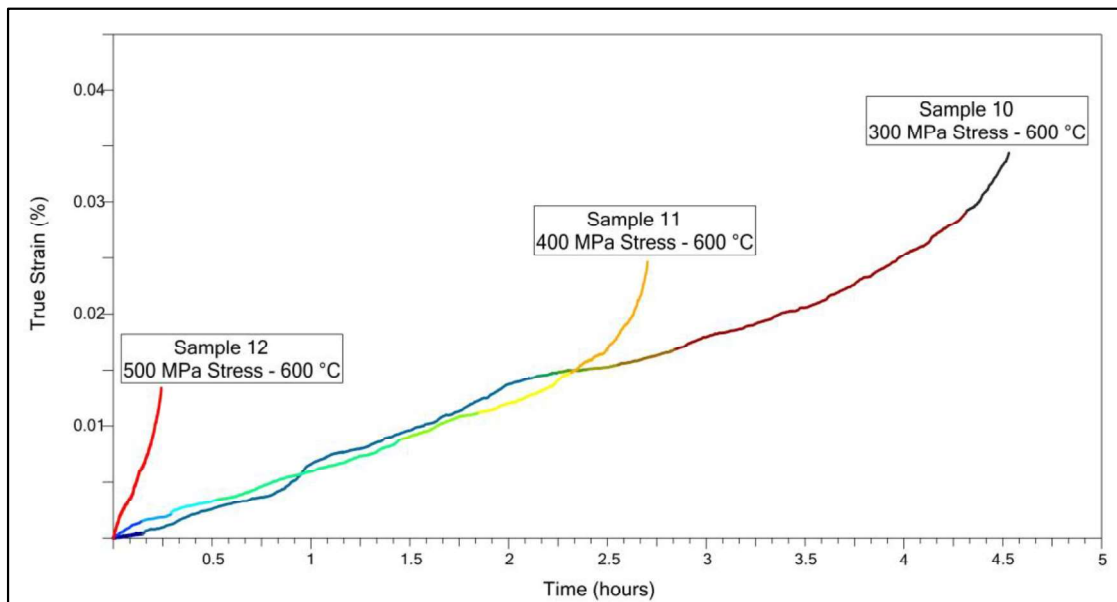


Figure 4.8-1. Creep Experiment results showing True Strain vs Time Curves, which were conducted at 600°C under 300, 400 and 500 MPa initial loading.

Almost no primary creep was observed in each tests as also found before by Tugrul et al. [35] in creep experiments of Ni₅₀Ti₂₅Hf₂₅ (at.%) alloys which might be due to the previous annealing heat treatment applied to samples. By the annealing heat treatment, dislocation formation and stress generation resulted from hot extrusion process could be annihilated/relieved and strain hardening did not take place during holding the sample at relatively high temperature. Secondary creep stage with linear increase in the creep strain during these tests was taken into account to calculate the strain rates. Since Sample 12 loaded under 500 MPa stress magnitude tertiary creep started just in a short time and it failed after 16 mins. However, secondary creep formation stage between 2 - 10 minutes was taken to calculate the strain rate, which was found to be 1.13E-05 s⁻¹. For Sample 10 and Sample 11, steady state strain rate values were determined from the secondary creep stage from different time intervals and steady state strain rate data of these intervals were calculated which were shown in Table 4.8-1.

Table 4.8-1. Creep Strain Rates for Ni₅₀Ti₃₀Hf₂₀ (at.%) HE-PN-AN samples at 600°C

Sample Number	Stress (MPa)	Steady State Strain Rate (s ⁻¹)
Sample 10	300	1.5103E-06
Sample 11	400	1.658E-06
Sample 12	500	1.13E-05

Optical micrographs during creep tests after several intervals were given in Figure 4.8-2 for Sample 10 which was tested with Ni₅₀Ti₃₀Hf₂₀ (at.%) at 600°C under 300 MPa stress magnitude and failed after 185 minutes. In creep tests different type of crack formations was observed which were mostly initiated from pre-notch. However, due to relatively high creep temperature the surface oxidation was severe and initiated cracks fully propagated along the surface till the end of the other edge of the sample. It is important to mention the crack lengths were not properly measured since the crack initiations and

propagations were found to very chaotic. The lengths of the first two major cracks that were shown at 130 minutes increased suddenly.

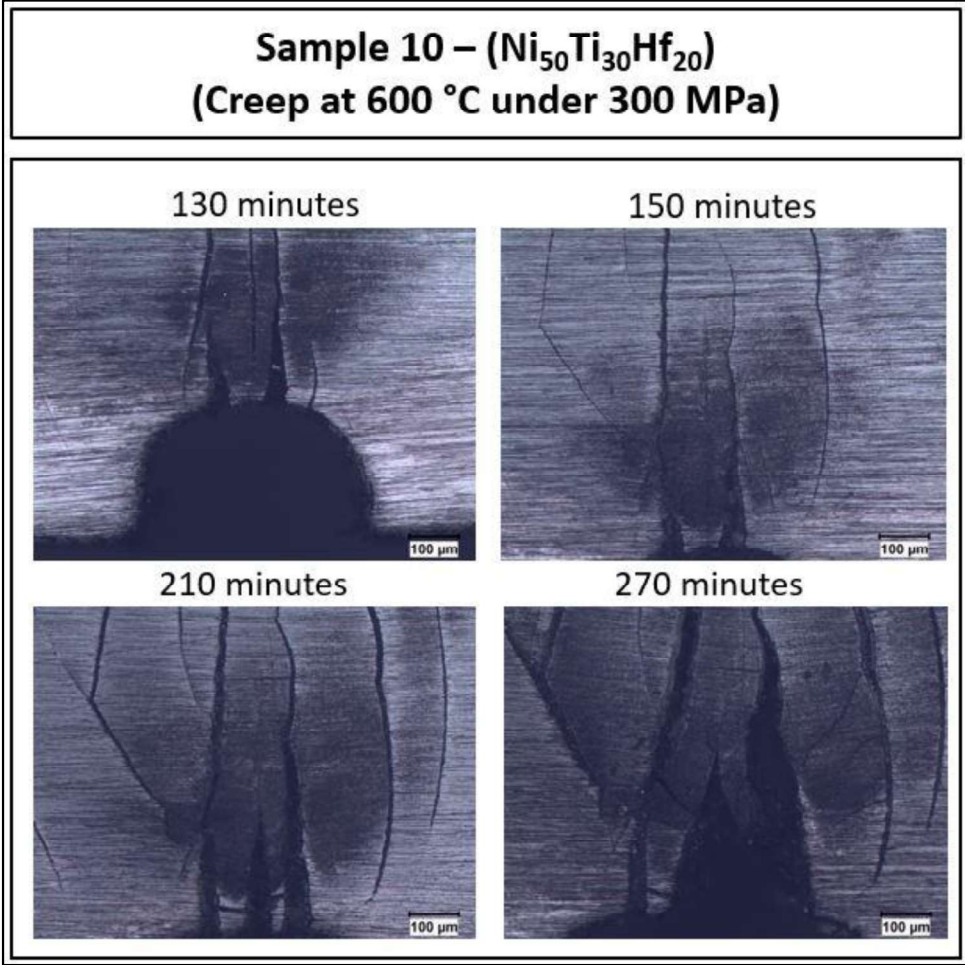


Figure 4.8-2. Optical micrographs taken after different intermittent creep experiment times for Sample 10 tested under 300 MPa

Surface optical micrographs of Sample 11, which was tested under 400 MPa stress magnitude were shown in Figure 4.8-3. Micrographs were taken at different intervals. Cracks were initiated around the pre-notch and also on the surface. Surface cracks propagated along the width of the sample gage from the first interval to the last interval, thus crack length measurements were not properly done.

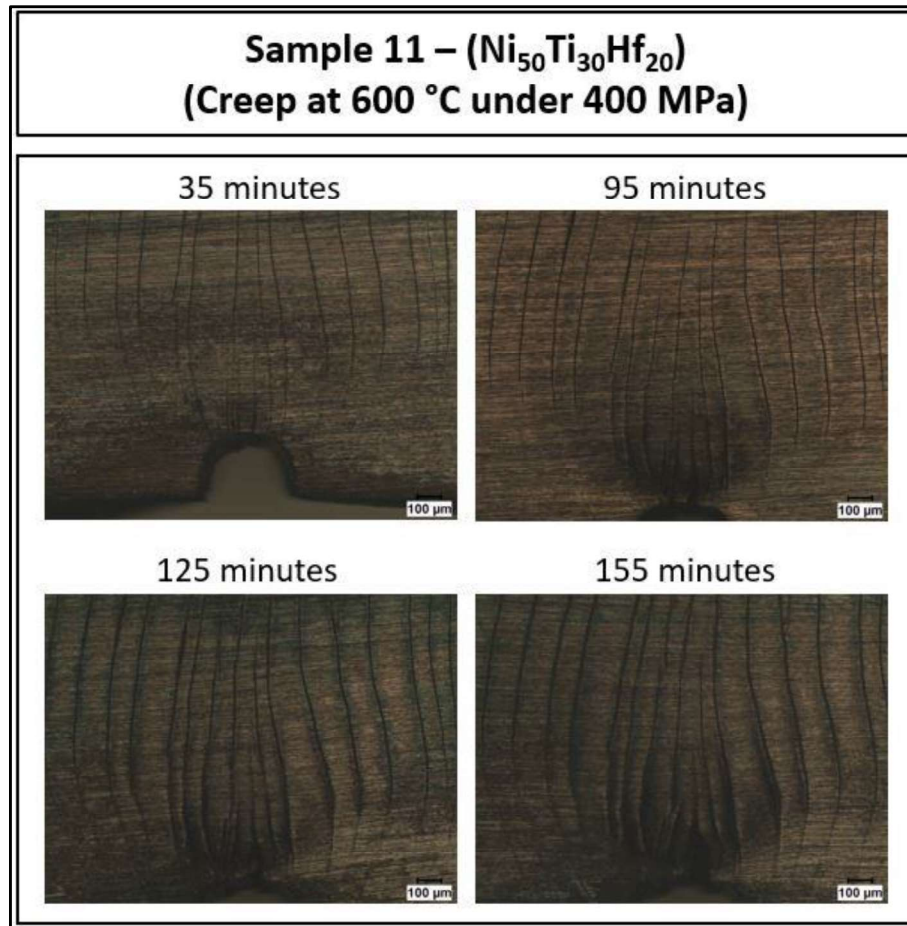


Figure 4.8-3. Optical micrographs taken after different intermittent creep experiment times for Sample 11 tested under 400 MPa

Optical micrographs of the surface of Sample 12, which was tested under 500 MPa stress were shown in Figure 4.8-4 after the failure of the sample since creep test was continued only for 16 minutes in which crack formations and crack propagations could not be followed. Wavy-like crack formations were observed after failure.

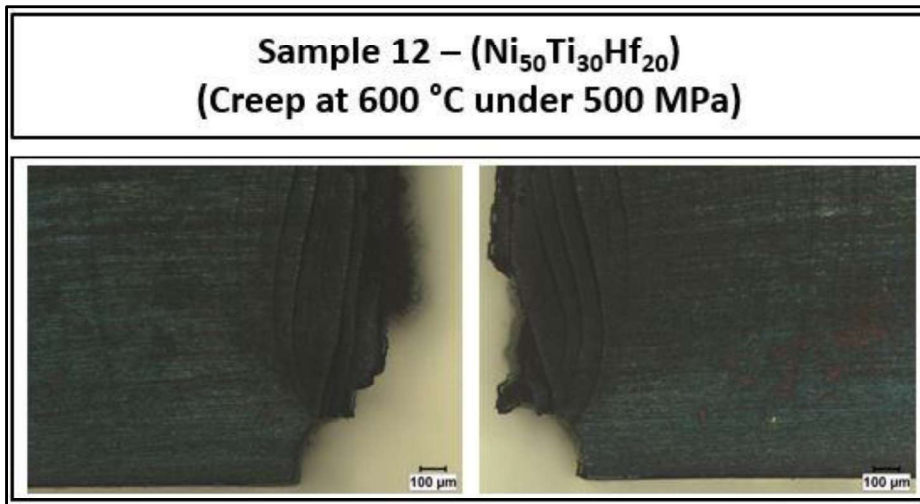


Figure 4.8-4. Optical micrographs taken after different intermittent creep experiment times for Sample 12 tested under 500 MPa

SEM images of fracture surfaces were given in Figure 4.8-5 and Figure 4.8-6 for samples tested under 300 MPa, 400 MPa and 500 MPa. Sample 10 showed mostly intergranular mode fracture surface including few numbers of small dimples.

The higher applied stress magnitude led to attain higher strain rate and also affected the mode of the fracture. Sample 12, which was tested under 500 MPa, showed transgranular manner fracture surface. The surface was observed to relatively flat and the surface showed a rock-candy appearance with few micro-voids. Micro-void formations may be due to presence of oxides from which the cracks initiated and then united.

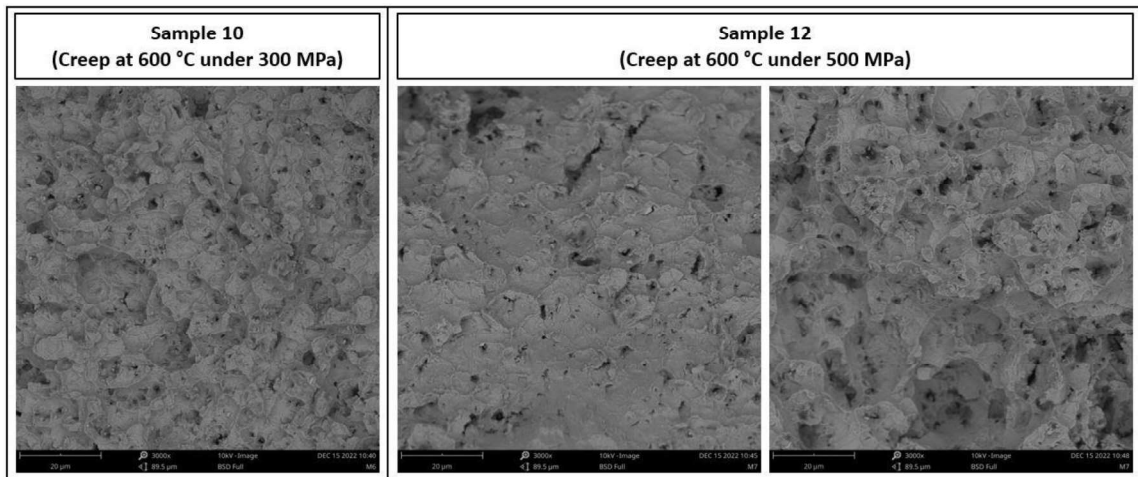


Figure 4.8-5. SEM Images from fracture surface of Sample 10 and Sample 12 which had creep experiment at 600°C under 300 MPa and 500 MPa

Sample 11 showed intergranular manner with some dimples as seen in Figure 4.8-6. Relatively larger sized dimples were observed in Sample 11 compared to Sample 10 due to the increased applied stress.

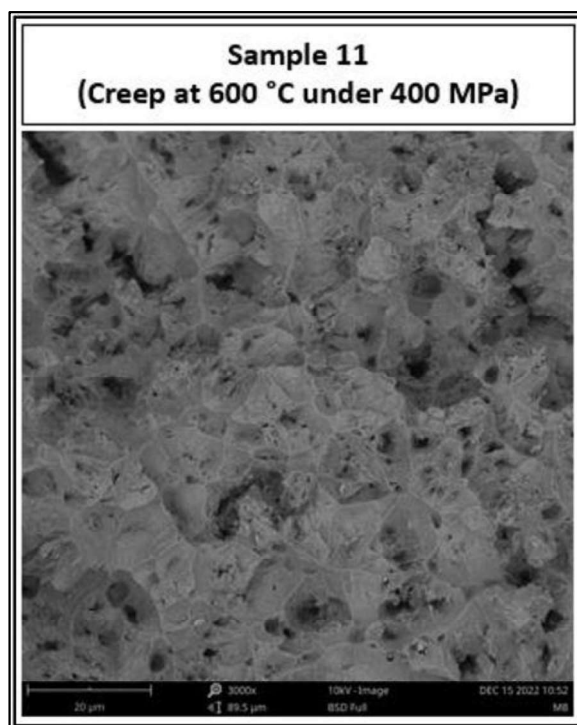


Figure 4.8-6. SEM Image from fracture surface of Sample 11 which had creep experiment at 600°C under 400 MPa

Strain rate increase due to the increase in the applied stress could have a significant effect on the fracture surface appearance and fracture mode of the alloy. Increase in the applied stress changed the appearance of fracture surface. 300 MPa and 400 MPa stress magnitudes led to the formation of intergranular manner with the dimples on the fracture surface and 500 MPa caused the formation of transgranular manner with flat fracture surface.

5. CONCLUSIONS

In this study, the main aim was to investigate effect of cyclic phase transformation on the crack growth behavior of NiTiHf HTSMAs having 20 at.% and 25 at.% Hf content. The studies were mainly focused on Ni₅₀Ti₃₀Hf₂₀ (at.%) alloy, however, the effect of increasing Hf content on the crack growth with cyclic phase transformation was also investigated using Ni₅₀Ti₂₅Hf₂₅ (at.%) alloy. In the light of the main objectives presented above, actuation fatigue experiments were designed and conducted on Ni₅₀Ti₃₀Hf₂₀ (at.%) and Ni₅₀Ti₂₅Hf₂₅ (at.%) alloys. Additionally, crack formation and propagation behavior of Ni₅₀Ti₃₀Hf₂₀ (at.%) alloy was also investigated via running creep experiments in the last part of the study.

First of all, actuation fatigue experiments were conducted on Hot-Extruded with no pre-notch (HE), Hot Extruded with pre-notch (HE-PN) and Hot Extruded with pre-notch and then annealed (HE-PN-AN) Ni₅₀Ti₃₀Hf₂₀ (at.%), samples and following conclusions were gathered during the tests. It is important to note that the codes of the samples were given in the parenthesis.

Unlike HE-PN samples, HE-PN-AN coded samples showed similar crack growth rates and trends since annealing heat treatment led to the elimination of deformation variations caused by hot extrusion. It was previously shown by our research group that the deformation variation was determined by observing flow lines along the cross section of the extruded billet and this variation caused to determine different actuation fatigue properties in the samples from the same batch [22]. Moreover, HE-PN-AN samples showed slower crack growth rates than that of the HE-PN samples. As crack growth rates of HE-PN-AN samples were found to be 0.077 and 0.08 $\mu\text{m}/\text{cycle}$, HE-PN samples exhibited crack growth rates as 0.099, 0.102, 0.147 $\mu\text{m}/\text{cycle}$. That was attributed to annealing heat treatment effect on relieving the internal stresses which were induced by hot extrusion process.

When optical micrographs of the cracks on annealed samples (HE-PN-AN) were investigated, it was seen that energy was spent not only on propagation of the major crack

from pre-notch but also crack formations of several minor side cracks. However, same magnitude of energy was spent only on propagation of the major crack, which started to form at the tip of the pre-notch in hot extruded samples (HE-PN). Due to annealing heat treatment, hot extrusion induced stresses were relieved and creation of new surfaces was relatively easier by spending less energy in annealed samples.

Actuation strain values throughout the thermal cycles were found to be almost same in HE-PN and HE-PN-AN samples. The values at the beginning were approximately 1.7% and dropped to approximately 1.3% with the number of cycles. The work output values should be the same for both of the alloys as well since work output can be found by multiplying the actuation strain values with the applied stress. The same magnitude of work output means that almost same amount of energy was spent on creating surfaces in both types of the samples (HE-PN and HE-PN-AN). However, annealed samples (HE-PN-AN) exhibited multiple minor cracks which were propagated with the same crack growth rate of the major crack during actuation cycles due to easier surface creation by using the same amount of energy as explained before. Also, it could be said that more stable crack growth rates and crack growth behavior were observed by annealing heat treatment during actuation fatigue cycling of $\text{Ni}_{50}\text{Ti}_{30}\text{Hf}_{20}$ (at.%) HTSMAs.

In the second section of the study, actuation fatigue experiments were conducted on 2 annealed virgin $\text{Ni}_{50}\text{Ti}_{30}\text{Hf}_{20}$ (at.%) HE-PN-AN samples with different test parameters. While UCT value was set to 600°C and the stress was kept at 200 MPa stress value during running the actuation fatigue experiment on one sample (Sample 7), stress value was increased to 300 MPa using 440°C UCT in testing of the other sample which was called as Sample 8.

It was seen that higher UCT resulted higher actuation strains and increase in actuation strain would lead on more crack opening and closing behavior which might be the reason of promoting the crack growth. This behavior led to observe many dimples and several united dimples on the fracture surface of the failed samples tested using higher UCT. However, main reasons of seeing totally different actuation strain, accumulated irrecoverable strain and thermal hysteresis values and trends with higher UCT application

were due to high amount of oxidation based surface cracks development and their cooperated propagation and also the accumulation of dislocations in the samples, which have lower strength at high temperatures. Therefore, transformation became more difficult by the increased plastic strain with the number of actuation cycles with many crack propagations. The sharp increase in thermal hysteresis was also due to the fact that, more energy was required to overcome phase transformation that might be inhibited by the phase transformation induced dislocations.

It could be seen that higher actuation strain values could be achieved by higher UCT application. Having higher actuation strain might be important since these materials are used as actuators and actuation strain value is an important performance parameter in actuation. On the other hand, it did not provide longer fatigue lifetimes, reliable and stable shape memory properties which are also more important in using actuators.

Additionally, higher UCT resulting severe oxidation led to develop an area around the pre-notch with many surface cracks propagating together such that it was not possible to follow the progress of the main crack. Furthermore, in actuation fatigue testing under 300 MPa stress, similar trends in actuation fatigue properties were determined that were also found in the experiments conducted under 200 MPa stress and using 440°C UCT.

In addition to higher UCT effect, higher stress caused sudden failure without crack propagation. Crack growth behavior could not be properly traced during actuation fatigue cycling of Sample 8, since the sample showed no crack propagation during first 200 cycles but a sudden fracture was realized after next 80 cycles.

Moreover, actuation fatigue experiment was run on annealed Ni₅₀Ti₂₅Hf₂₅ (at.%) (HE-PN-AN) sample. Sample was tested using 600°C UCT, since Ni₅₀Ti₂₅Hf₂₅ (at.%) alloys have higher TTs, thus higher UCT should be used to see full transformation during actuation fatigue cycles. First of all, it is important to mention that very severe surface oxidation was observed possibly due to high Hf content of this alloy since Hf has a very high affinity to oxygen and UCT was kept at 600°C throughout the cycles. More surface

cracks were observed and this might be attributed to the hard and brittle nature HfO [78]. On the other hand, dimple formations were observed on the fracture surface since higher UCT led to achieve higher actuation strain and relatively more crack opening-closing behavior during actuation cycling. Also, higher crack growth rate was obtained as “0.661 $\mu\text{m}/\text{cycle}$ ” in this alloy because of the manner of the crack opening and closing. Having relatively higher and stable actuation strain values in $\text{Ni}_{50}\text{Ti}_{30}\text{Hf}_{20}$ (at.%) in addition to their lower thermal hysteresis values than that of $\text{Ni}_{50}\text{Ti}_{25}\text{Hf}_{25}$ (at.%) alloys could make them a better alternative for actuation application. However, both alloys showed unstable shape memory properties in addition to shorter lifetimes when UCT was kept at high temperatures.

Finally, creep experiments were conducted on $\text{Ni}_{50}\text{Ti}_{30}\text{Hf}_{20}$ (at.%) under 300 MPa, 400 MPa and 500 MPa at 600°C. It was primarily found that no primary creep stage was observed in all creep curves of the 3 experiments. This might be attributed to the high creep temperature and annealing of the samples before the creep experiments. Therefore, it was not possible to achieve strain hardening in annealed samples at 600°C. In addition, the creep strain rates were calculated from the secondary stages of the creep curves and it was determined that 500 MPa caused a sudden fracture with a higher strain rate and by quickly entering to the tertiary creep stage. It should be kept in mind that the creep experiments can be further conducted at relatively lower creep temperatures to reveal the crack initiation and propagation behavior of these alloys. Detailed information about crack propagation could not be obtained because the time duration of the creep experiments was very short.

Different types of crack formations were detected on the surface of the creep tested samples compared to thermally cycled samples. In creep tests, crack formations started due to the surface oxidation on the surface and high creep temperature caused chaotic crack formations. Cracks propagated suddenly along the full width of the samples starting from the tip of the pre-notch. Therefore, measuring the crack lengths throughout the creep deformation was not possible. The fracture surfaces of the samples that were creep tested were also investigated and it was found that higher applied stress led to achieve higher creep strain rates and appearance of the fracture surface was observed to be different.

It is already known from the literature that strain rate in addition to creep temperature affects the fracture mode. Moderately higher strain rate could change the size and depth of the dimples and the fracture surface became relatively flat with fewer dimple formations when the applied stress was kept very high [79].

6. REFERENCES

- [1] O. K., C.M. Wayman, General applications of SMA's and smart materials, Cambridge University Press, **1998**.
- [2] D.C. Lagoudas, ed., Shape Memory Alloys, **2008**. <https://doi.org/10.1002/0471732877.emd002>.
- [3] C. Calhoun, R. Wheeler, T. Baxevanis, D.C. Lagoudas, Actuation fatigue life prediction of shape memory alloys under the constant-stress loading condition, *Scr. Mater.* **95** (2015) 58–61. <https://doi.org/10.1016/j.scriptamat.2014.10.005>.
- [4] J. Ma, I. Karaman, R.D. Noebe, J. Ma, I. Karaman, R.D. Noebe, High temperature shape memory alloys, *Int. Mater. Rev.* **55** (2010) 257–315. <https://doi.org/10.1179/095066010X12646898728363>.
- [5] K. Otsuka, X. Ren, Recent developments in the research of shape memory alloys, *Intermetallics.* **7** (1999) 511–528. [https://doi.org/10.1016/S0966-9795\(98\)00070-3](https://doi.org/10.1016/S0966-9795(98)00070-3).
- [6] F. El Feninat, G. Laroche, M. Fiset, D. Mantovani, Shape Memory Materials for Biomedical Applications, *Adv. Eng. Mater.* **4** (2002) 91–104. [https://doi.org/10.1002/1527-2648\(200203\)4:3<91::AID-ADEM91>3.0.CO;2-B](https://doi.org/10.1002/1527-2648(200203)4:3<91::AID-ADEM91>3.0.CO;2-B).
- [7] M.A. Farmani, M. Ghassemieh, Shape memory alloy-based moment connections with superior self-centering properties, *Smart Mater. Struct.* **25** (2016). <https://doi.org/10.1088/0964-1726/25/7/075028>.
- [8] C. Fang, D. Liang, Y. Zheng, M.C.H. Yam, R. Sun, Rocking bridge piers equipped with shape memory alloy (SMA) washer springs, *Eng. Struct.* **214** (2020). <https://doi.org/10.1016/j.engstruct.2020.110651>.
- [9] J. Mohd Jani, M. Leary, A. Subic, M.A. Gibson, A review of shape memory alloy research, applications and opportunities, *Mater. Des.* **56** (2014) 1078–1113. <https://doi.org/10.1016/j.matdes.2013.11.084>.
- [10] D.J. Hartl, D.C. Lagoudas, Aerospace applications of shape memory alloys, *Proc. Inst. Mech. Eng. Part G J. Aerosp. Eng.* **221** (2007) 535–552. <https://doi.org/10.1243/09544100JAERO211>.
- [11] K. Otsuka, T. Kakeshita, Science and technology of shape-memory alloys: New developments, *MRS Bull.* **27** (2002) 91–98. <https://doi.org/10.1557/mrs2002.43>.
- [12] S. Saadat, J. Salichs, M. Noori, Z. Hou, H. Davoodi, I. Bar-on, Y. Suzuki, A. Masuda, An overview of vibration and seismic applications of NiTi shape memory alloy, *Smart Mater. Struct.* **11** (2002) 218–229. <https://doi.org/10.1088/0964-1726/11/2/305>.

- [13] K. Otsuka, X. Ren, Physical metallurgy of Ti-Ni-based shape memory alloys, *Prog. Mater. Sci.* 50 (2005) 511–678. <https://doi.org/10.1016/j.pmatsci.2004.10.001>.
- [14] J. Ma, I. Karaman, R.D. Noebe, High temperature shape memory alloys, *Int. Mater. Rev.* 55 (2010) 257–315. <https://doi.org/10.1179/095066010X12646898728363>.
- [15] H.E. Karaca, E. Acar, H. Tobe, S.M. Saghaian, NiTiHf-based shape memory alloys, *Mater. Sci. Technol.* 30 (2014) 1530–1544. <https://doi.org/10.1179/1743284714Y.0000000598>.
- [16] H.E. Karaca, S.M. Saghaian, G. Ded, H. Tobe, B. Basaran, H.J. Maier, R.D. Noebe, Y.I. Chumlyakov, Effects of nanoprecipitation on the shape memory and material properties of an Ni-rich NiTiHf high temperature shape memory alloy, *Acta Mater.* 61 (2013) 7422–7431. <https://doi.org/10.1016/j.actamat.2013.08.048>.
- [17] R. Santamarta, R. Arróyave, J. Pons, A. Evirgen, I. Karaman, H.E. Karaca, R.D. Noebe, TEM study of structural and microstructural characteristics of a precipitate phase in Ni-rich Ni-Ti-Hf and Ni-Ti-Zr shape memory alloys, *Acta Mater.* 61 (2013) 6191–6206. <https://doi.org/10.1016/j.actamat.2013.06.057>.
- [18] O. Karakoc, C. Hayrettin, M. Bass, S.J. Wang, D. Canadinc, J.H. Mabe, D.C. Lagoudas, I. Karaman, Effects of upper cycle temperature on the actuation fatigue response of NiTiHf high temperature shape memory alloys, *Acta Mater.* 138 (2017) 185–197. <https://doi.org/10.1016/j.actamat.2017.07.035>.
- [19] H.H. Saygili, H.O. Tugrul, B. Kockar, Effect of Aging Heat Treatment on the High Cycle Fatigue Life of Ni_{50.3}Ti_{29.7}Hf₂₀ High-Temperature Shape Memory Alloy, *Shape Mem. Superelasticity.* 5 (2019) 32–41. <https://doi.org/10.1007/s40830-018-00202-5>.
- [20] N. Babacan, M. Bilal, C. Hayrettin, J. Liu, O. Benafan, I. Karaman, Effects of cold and warm rolling on the shape memory response of Ni₅₀Ti₃₀Hf₂₀ high-temperature shape memory alloy, *Acta Mater.* 157 (2018) 228–244. <https://doi.org/10.1016/j.actamat.2018.07.009>.
- [21] O. Akgul, H.O. Tugrul, B. Kockar, Effect of the cooling rate on the thermal and thermomechanical behavior of NiTiHf high-temperature shape memory alloy, *J. Mater. Res.* 35 (2020) 1572–1581. <https://doi.org/10.1557/jmr.2020.139>.
- [22] E. Akin, O. Akgul, H.O. Tugrul, G. Dugan, B. Kockar, Investigating the effect of hot extrusion and annealing to the functional fatigue behavior of Ni₅₀Ti₃₀Hf₂₀ high temperature shape memory alloy, *Smart Mater. Struct.* 30 (2021). <https://doi.org/10.1088/1361-665X/ac1bee>.
- [23] F.R. Phillips, R.W. Wheeler, A.B. Geltmacher, D.C. Lagoudas, Evolution of internal damage during actuation fatigue in shape memory alloys, *Int. J. Fatigue.* 124 (2019) 315–327. <https://doi.org/10.1016/j.ijfatigue.2018.12.019>.
- [24] E. Sgambitterra, P. Magarò, F. Niccoli, D. Renzo, C. Maletta, Low-to-high cycle

- fatigue properties of a NiTi shape memory alloy, *Procedia Struct. Integr.* 18 (2019) 908–913. <https://doi.org/https://doi.org/10.1016/j.prostr.2019.08.242>.
- [25] F. Furgiuele, P. Magarò, C. Maletta, E. Sgambitterra, Functional and Structural Fatigue of Pseudoelastic NiTi: Global Vs Local Thermo-Mechanical Response, *Shape Mem. Superelasticity.* 6 (2020) 242–255. <https://doi.org/10.1007/s40830-020-00289-9>.
- [26] A.L. McKelvey, R.O. Ritchie, Fatigue-crack growth behavior in the superelastic and shape-memory alloy nitinol, *Metall. Mater. Trans. A.* 32 (2001) 731–743. <https://doi.org/10.1007/s11661-001-0089-7>.
- [27] K. Gall, H. Maier, Cyclic deformation mechanisms in precipitated NiTi shape memory alloys, *Acta Mater.* 50 (2002) 4643–4657. [https://doi.org/10.1016/S1359-6454\(02\)00315-4](https://doi.org/10.1016/S1359-6454(02)00315-4).
- [28] G. Eggeler, E. Hornbogen, A. Yawny, A. Heckmann, M. Wagner, Structural and functional fatigue of NiTi shape memory alloys, *Mater. Sci. Eng. A.* 378 (2004) 24–33. <https://doi.org/10.1016/j.msea.2003.10.327>.
- [29] O. Karakoc, C. Hayrettin, D. Canadinc, I. Karaman, Role of applied stress level on the actuation fatigue behavior of NiTiHf high temperature shape memory alloys, *Acta Mater.* 153 (2018) 156–168. <https://doi.org/10.1016/j.actamat.2018.04.021>.
- [30] O.W. Bertacchini, D.C. Lagoudas, E. Patoor, Thermomechanical transformation fatigue of TiNiCu SMA actuators under a corrosive environment - Part I: Experimental results, *Int. J. Fatigue.* 31 (2009) 1571–1578. <https://doi.org/10.1016/j.ijfatigue.2009.04.012>.
- [31] Y. Wu, A. Ojha, L. Patriarca, H. Sehitoglu, Fatigue Crack Growth Fundamentals in Shape Memory Alloys, *Shape Mem. Superelasticity.* 1 (2015) 18–40. <https://doi.org/10.1007/s40830-015-0005-4>.
- [32] S.W. Robertson, A.R. Pelton, R.O. Ritchie, Mechanical fatigue and fracture of Nitinol, *Int. Mater. Rev.* 57 (2012) 1–37. <https://doi.org/10.1179/1743280411Y.0000000009>.
- [33] B. Haghgouyan, B. Young, S. Picak, T. Baxevanis, I. Karaman, D.C. Lagoudas, A Unified Description of Mechanical and Actuation Fatigue Crack Growth in Shape Memory Alloys, n.d.
- [34] C. LExcellent, P. Robinet, J. Bernardini, D.L. Beke, P. Olier, High temperature creep measurements in equiatomic Ni-Ti shape memory alloy, *Materwiss. Werksttech.* 36 (2005) 509–512. <https://doi.org/10.1002/mawe.200500922>.
- [35] H.O. Tugrul, O. Akgul, B. Kockar, Creep behavior of 50at%Ni 25at%Ti 25at%Hf high temperature shape memory alloy under constant load, *Mater. Today Commun.* 33 (2022) 104827. <https://doi.org/10.1016/j.mtcomm.2022.104827>.
- [36] K. V. Ramaiah, C.N. Saikrishna, V.R. Ranganath, V. Buravalla, S.K. Bhaumik,

- Fracture of thermally activated NiTi shape memory alloy wires, *Mater. Sci. Eng. A.* 528 (2011) 5502–5510. <https://doi.org/10.1016/j.msea.2011.03.070>.
- [37] A.P. Iliopoulos, J.C. Steuben, T. Kirk, T. Baxevanis, J.G. Michopoulos, D.C. Lagoudas, Thermomechanical failure response of notched NiTi coupons, *Int. J. Solids Struct.* 125 (2017) 265–275. <https://doi.org/10.1016/j.ijsolstr.2017.06.017>.
- [38] S. Jape, B. Young, B. Haghgouyan, C. Hayrettin, T. Baxevanis, D.C. Lagoudas, I. Karaman, Actuation-Induced stable crack growth in near-equiatom nickel-titanium shape memory alloys: Experimental and numerical analysis, *Int. J. Solids Struct.* 221 (2021) 165–179. <https://doi.org/10.1016/j.ijsolstr.2020.09.032>.
- [39] O. K., C.M. Wayman, *Shape memory materials*, Cambridge University Press, 1998.
- [40] A. Nagasawa, K. Enami, Y. Ishino, Y. Abe, S. Nenno, Reversible shape memory effect, *Scr. Metall.* 8 (1974) 1055–1060. [https://doi.org/10.1016/S0036-9748\(74\)80003-7](https://doi.org/10.1016/S0036-9748(74)80003-7).
- [41] T. Saburi, S. Nenno, Reversible Shape Memory in Cu-Zn-Ga, *Scr. Metall.* 8 (1974) 1363–1367.
- [42] B. Kockar, SHAPE MEMORY BEHAVIOR OF ULTRAFINE GRAINED NiTi AND TiNiPd SHAPE MEMORY ALLOYS, 2007.
- [43] T.A. Schroeder, C.M. Wayman, The two-way shape memory effect and other “training” phenomena in CuZn single crystals, *Scr. Metall.* 11 (1977) 225–230. [https://doi.org/10.1016/0036-9748\(77\)90058-8](https://doi.org/10.1016/0036-9748(77)90058-8).
- [44] X. Ren, K. Otsuka, Universal symmetry property of point defects in crystals, *Phys. Rev. Lett.* 85 (2000) 1016–1019. <https://doi.org/10.1103/PhysRevLett.85.1016>.
- [45] O.J. Godard, M.Z. Lagoudas, D.C. Lagoudas, Design of space systems using shape memory alloys, *Smart Struct. Mater.* 2003 *Smart Struct. Integr. Syst.* 5056 (2003) 545. <https://doi.org/10.1117/12.483469>.
- [46] A. Ölander, Cadmium-Gold Alloys Solid, *J. Am. Chem. Soc.* 54 (1932) 3819–3833.
- [47] W.J. Buehler, J. V. Gilfrich, R.C. Wiley, Effect of Low-Temperature Phase Changes on the Mechanical Properties of Alloys near Composition TiNi, *J. Appl. Phys.* 34 (1963) 1475–1477. <https://doi.org/10.1063/1.1729603>.
- [48] T.B. Massalski, *Massalski T.B.-Binary alloy phase diagrams. V2*, (1986) 1129.
- [49] S. Miyazaki, Y. Ohmi, K. Otsuka, Y. Suzuki, CHARACTERISTICS OF DEFORMATION AND TRANSFORMATION PSEUDOELASTICITY IN Ti-Ni ALLOYS., *J. Phys. (Paris), Colloq.* 43 (1982). <https://doi.org/10.1051/jphyscol:1982434>.
- [50] S. Miyazaki, K. Otsuka, DEFORMATION AND TRANSITION BEHAVIOR

- ASSOCIATED WITH THE R-PHASE IN Ti-Ni ALLOYS., *Metall. Trans. A, Phys. Metall. Mater. Sci.* 17 A (1986) 53–63. <https://doi.org/10.1007/BF02644442>.
- [51] B. Kockar, I. Karaman, J.I. Kim, Y. Chumlyakov, A method to enhance cyclic reversibility of NiTiHf high temperature shape memory alloys, *Scr. Mater.* 54 (2006) 2203–2208. <https://doi.org/10.1016/j.scriptamat.2006.02.029>.
- [52] B. Kockar, I. Karaman, A. Kulkarni, Y. Chumlyakov, I. V. Kireeva, Effect of severe ausforming via equal channel angular extrusion on the shape memory response of a NiTi alloy, *J. Nucl. Mater.* 361 (2007) 298–305. <https://doi.org/10.1016/j.jnucmat.2006.12.007>.
- [53] D.A. Miller, D.C. Lagoudas, Influence of cold work and heat treatment on the shape memory effect and plastic development of NiTi, *Mater. Sci. Eng. A.* 308 (2001) 161–175. [https://doi.org/10.1016/S0921-5093\(00\)01982-1](https://doi.org/10.1016/S0921-5093(00)01982-1).
- [54] R.R. Adharapurapu, F. Jiang, K.S. Vecchio, Aging effects on hardness and dynamic compressive behavior of Ti-55Ni (at.%) alloy, *Mater. Sci. Eng. A.* 527 (2010) 1665–1676. <https://doi.org/10.1016/j.msea.2009.10.069>.
- [55] T. Saburi, M. Yoshida, S. Nenno, Deformation behavior of shape memory Ti-Ni alloy crystals, *Scr. Metall.* 18 (1984) 363–366.
- [56] J.T. Lim, D.L. McDowell, Degradation of an Ni-Ti alloy during cyclic loading, in: *Proc.SPIE*, 1994: pp. 326–341. <https://doi.org/10.1117/12.174083>.
- [57] D.A. Miller, D.C. Lagoudas, Thermomechanical characterization of NiTiCu and NiTi SMA actuators: Influence of plastic strains, *Smart Mater. Struct.* 9 (2000) 640–652. <https://doi.org/10.1088/0964-1726/9/5/308>.
- [58] D.H. C., V.V. J.H.N., Martensitic Transformations in Gold-Titanium, Palladium-Titanium and Platinum-Titanium Alloys Near The Equiatomic Composition, *J. Less-Common Met.* 20 (1970) 83–91.
- [59] M.A. Schmerling, B.K. Das, D.S. Lieberman, Phase transformations in near equiatomic Ta-Ru alloys, *Metall. Trans.* 1 (1970) 3273–3278. <https://doi.org/10.1007/BF03037853>.
- [60] B.K. Das, E.A. Stern, D.S. Lieberman, Displacive transformations in near-equiatomc Nb-Ru alloys-II. Energetics and mechanism, *Acta Metall.* 24 (1976) 37–44. [https://doi.org/10.1016/0001-6160\(76\)90144-9](https://doi.org/10.1016/0001-6160(76)90144-9).
- [61] S.K. Wu, C.M. Wayman, Martensitic Transformations and the Shape Memory Effect in TisoNiloAu4o and TisoAuso Alloys, 376 (1987) 359–376.
- [62] R. Orlando, R.D. Noebe, B. Tiffany, G. Anita, P. Anna, S. Daniel, S.J. Hans, K. Michael, Characterization of Ternary NiTiPt High-Temperature Shape Memory Alloys, in: *Smart Struct. Mater. 2005 Behav. Mech.*, 2005. <https://doi.org/10.1117/12.599608>.

- [63] P.G. Lindquist, C.M. Wayman, Shape Memory and Transformation Behavior of Martensitic Ti-Pd-Ni and Ti-Pt-Ni Alloys, Butterworth-Heinemann Ltd, n.d. <https://doi.org/10.1016/B978-0-7506-1009-4.50009-3>.
- [64] S.M. Saghaian, H.E. Karaca, H. Tobe, A.S. Turabi, S. Saedi, S.E. Saghaian, Y.I. Chumlyakov, R.D. Noebe, High strength NiTiHf shape memory alloys with tailorable properties, *Acta Mater.* 134 (2017) 211–220. <https://doi.org/10.1016/j.actamat.2017.05.065>.
- [65] T. Umale, D. Salas, B. Tomes, R. Arroyave, I. Karaman, The effects of wide range of compositional changes on the martensitic transformation characteristics of NiTiHf shape memory alloys, *Scr. Mater.* 161 (2019) 78–83. <https://doi.org/10.1016/j.scriptamat.2018.10.008>.
- [66] J. Schijve, *Fatigue of structures and materials*, 2nd ed., Springer Netherlands, Dordrecht, 2009. <https://doi.org/10.1007/978-1-4020-6808-9>.
- [67] M. Ekiciler, B. Kockar, Crack growth behavior during actuation cycling of hot extruded and annealed Ni₅₀Ti₃₀Hf₂₀ high temperature shape memory alloys, *Smart Mater. Struct.* 31 (2022). <https://doi.org/10.1088/1361-665X/ac798f>.
- [68] M.E. Kassner, M.-T. Pérez-Prado, Introduction, in: *Fundam. Creep Met. Alloy.*, Elsevier, 2004: pp. 3–9. <https://doi.org/10.1016/B978-008043637-1/50002-8>.
- [69] A.K. Mukherjee, High-temperature-creep mechanism of TiNi, *J. Appl. Phys.* 39 (1968) 2201–2204. <https://doi.org/10.1063/1.1656527>.
- [70] J. Bernardini, C. Lexcellent, L. Daróczy, D.L. Beke, Ni diffusion in near-equiatomic Ni-Ti and Ni-Ti(-Cu) alloys, *Philos. Mag.* 83 (2003) 329–338. <https://doi.org/10.1080/0141861021021000036656>.
- [71] S.M. Oppenheimer, A.R. Yung, D.C. Dunand, Power-law creep in near-equiatomic nickel-titanium alloys, *Scr. Mater.* 57 (2007) 377–380. <https://doi.org/10.1016/j.scriptamat.2007.05.004>.
- [72] P.K. Kumar, U. Desai, J.A. Monroe, D.C. Lagoudas, I. Karaman, G. Bigelow, R.D. Noebe, Experimental investigation of simultaneous creep, plasticity and transformation of Ti_{50.5}Pd₃₀Ni_{19.5} high temperature shape memory alloy during cyclic actuation, *Mater. Sci. Eng. A.* 530 (2011) 117–127. <https://doi.org/10.1016/j.msea.2011.09.051>.
- [73] P.S. Chaugule, O. Benafan, J.B. le Graverend, Phase transformation and viscoplasticity coupling in polycrystalline nickel-titanium-hafnium high-temperature shape memory alloys, *Acta Mater.* 221 (2021) 117381. <https://doi.org/10.1016/j.actamat.2021.117381>.
- [74] Saygili H H, The development of a fatigue test machine to investigate the functional fatigue life of high temperature shape memory alloys and the determination of the functional fatigue life of these alloys, Hacettepe University,

2018.

- [75] H. Tada, P.C. Paris, G.R. Irwin, Stress Analysis Results for Common Test Specimen Configurations, in: H. Tada, P.C. Paris, G.R. Irwin (Eds.), Stress Anal. Cracks Handbook, Third Ed., ASME Press, **2000**: p. 0. <https://doi.org/10.1115/1.801535.ch2>.
- [76] O. Karakoc, C. Hayrettin, A. Evirgen, R. Santamarta, D. Canadinc, R.W. Wheeler, S.J. Wang, D.C. Lagoudas, I. Karaman, Role of microstructure on the actuation fatigue performance of Ni-Rich NiTiHf high temperature shape memory alloys, *Acta Mater.* 175 (**2019**) 107–120. <https://doi.org/10.1016/j.actamat.2019.05.051>.
- [77] B. Kockar, I. Karaman, J.I. Kim, Y.I. Chumlyakov, J. Sharp, C.J. (Mike. Yu, Thermomechanical cyclic response of an ultrafine-grained NiTi shape memory alloy, *Acta Mater.* 56 (**2008**) 3630–3646. <https://doi.org/10.1016/j.actamat.2008.04.001>.
- [78] K.M. Kim, J.T. Yeom, H.S. Lee, S.Y. Yoon, J.H. Kim, High temperature oxidation behavior of Ti-Ni-Hf shape memory alloy, *Thermochim. Acta.* 583 (**2014**) 1–7. <https://doi.org/10.1016/j.tca.2014.02.016>.
- [79] A.S.M.H. Committee, *Fractography*, (**1987**). <https://doi.org/10.31399/asm.hb.v12.9781627081818>.

APPENDIX

APPENDIX 1 - Publications

M. Ekiciler, B. Kockar, Crack growth behavior during actuation cycling of hot extruded and annealed Ni₅₀Ti₃₀Hf₂₀high temperature shape memory alloys, Smart Mater. Struct. 31 (2022). <https://doi.org/10.1088/1361-665X/ac798f>.

APPENDIX 2 – Conference Presentations

M. Ekiciler, B. Kockar, Influence of Annealing Heat Treatment on Crack Growth Behavior and Crack Size Evolution During Actuation Cycling of Ni₅₀Ti₃₀Hf₂₀ Alloys, 12th European Symposium on Martensitic Transformations (ESOMAT 2022), September 5-9 Ankara, TURKEY.